ISSN number 0971 - 9709

IGU
Promoting Earth System Sciences

The Journal of Indian Geophysical Union

AN OPEN ACCESS BIMONTHLY JOURNAL OF IGU

VOLUME 29, ISSUE 1, JANUARY 2025

EDITORIAL OFFICE

Indian Geophysical Union, NGRI Campus, Uppal Road, Hyderabad- 500 007

Telephone: 91-4027012739, 27012332; Telefax:+91-04-27171564

Email: jigu1963@gmail.com, website: http://iguonline.in/journal/

The Journal with six issues in a year publishes articles covering

Solid Earth Geosciences; Marine Geosciences; and Atmospheric, Space and Planetary Sciences.

The Journal is Financially supported by MoES, Govt. of India.

Annual Subscription

Individual Rs -1000/- per issue and Institutional Rs- 5000/- for six issues

Payments should be sent by DD drawn in favour of "The Treasurer, Indian Geophysical Union", payable at Hyderabad,

Money Transfer/NEFT/RTGS (Inter-Bank Transfer), Treasurer, Indian Geophysical Union, State Bank of India, Habsiguda Branch,

Habsiguda, Uppal Road, Hyderabad- 500 007

A/C: 52191021424, IFSC Code: SBIN0020087, MICR Code: 500002318, SWIFT Code: SBININBBHO9.

For correspondence, please contact, Hon. Secretary, Indian Geophysical Union, NGRI Campus, Uppal Road,

Hyderabad - 500 007, India; Email: igu123@gmail.com; Ph: 040 27012332

ISSN: 0257-7968 (Clarivate Analytics)
ISSN: 0971-9709 (NISCAIR)
Approved as bimonthly ESCI journal by Clarivate Analytics
Cited in Indian Citation Index (ICI), New Delhi
Evaluated by NISCAIR, New Delhi
SCI & UGC Approved Journal

CONTENTS

Research Articles

Development of Spectral gamma-ray logging probe using $LaBr_3$(Ce) detector and testing of its application in geophysical prospecting for uranium
Habeeb Ali Khan[1], Srinivasulu[1], A. Markandeyulu[1], G. Udaya Laxmi[2], M.N. Chary (Retd.)[1] and Prakhar Kumar[1] **1**

Petrographic study of Umlatdoh limestone in parts of Meghalaya, north-east India with an emphasis on diagenetic and depositional attributes
Anni Rani Das, Meghali Baruah[*], Mrinal Kanti Pathak, Devesh Walia and Shikhar Kumar **12**

Reservoir characterization using a hybrid of particle swarm optimization: A case study from the Blackfoot field, Canada
Ravi Kant[1*], S.P. Maurya[1], Nitin Verma[1], Raghav Singh[1], K.H. Singh[2], Ajay P. Singh[1], Prabodh K. Kushwaha[1], M.K. Srivastava[1], G. Hema[1], Harsha Raghuvanshi[1] and Richa[1] **26**

Impact of solar activity on ~200-year cyclic variations in groundwater recharge rates in the Badain 500 Jaran Desert, Inner Mongolia, Northwest China
Rajesh Rekapalli[1,2], R.K.Tiwari[1] and Animesh Mandal[3] **38**

Finite Element solutions of Maxwell fluid flow towards a stretching surface with addition of 507 thermal radiation, porous medium and magnetic field
Nagaraju Bathula[*] and Kishan Naikoti **45**

Kinematics of the Capricorn microplate and its surrounding regions as inferred from the analyses of GPS data
A.Akilan*[1], K. K. Abdul Azeez[1], Sravan K. Kotluri[2], H.V.S. Satyanarayana[1], S. Padhy[3] and O.P. Pandey **56**

Conference Report

Report on 61st Annual Convention of the Indian Geophysical Union (IGU), held at Banaras Hindu University (BHU), Varanasi (India) during December 3–5, 2024
Abhey Ram Bansal[1]*, A.S.S.S.R.S. Prasad [1] and R K Mall[2] **64**

J. Ind. Geophys. Union, 29(1) (2025), 1-11
https://doi.org/10.71122/JIGU.29(1)2025.001

Development of Spectral gamma-ray logging probe using $LaBr_3$(Ce) detector and testing of its application in geophysical prospecting for uranium

Habeeb Ali Khan[1], Srinivasulu[1], A. Markandeyulu[1], G. Udaya Laxmi[2], M.N. Chary (Retd.)[1] and Prakhar Kumar[1]
[1]Atomic Minerals Directorate for Exploration and Research, Begumpet, Hyderabad-500016, India
[2] Centre of Exploration Geophysics, Osmania University, Hyderabad-500007, India
Corresponding author: habeeb82@hotmail.com

ABSTRACT

Spectral gamma ray logging is a useful technique for uranium exploration during the large-scale borehole drilling stage. It can detect sub-surface uranium-bearing formations, quantify uranium concentration, and map geological structures. Traditionally, NaI(Tl) crystal is used as a detector in spectral logging probes. The coring boreholes drilled for uranium exploration have a limited diameter, necessitating smaller detectors in Spectral gamma ray logging probes. This limitation resulted in reduced sensitivity, increased high-energy thorium contributions in uranium and potassium channels, and thus pose challenges in accurately quantifying uranium content with the NaI(Tl) detector. Advances in detector technology, such as $LaBr_3$(Ce), $CeBr_3$ and CsI(Tl) scintillation detectors, offer improved energy resolution and sensitivity in smaller form factors. The $LaBr_3$(Ce) detector has various advantages over standard NaI(Tl) detectors of the same size, such as high density, superior light output, good linearity, faster response time, and improved energy resolution. In this regard, an attempt was made to use a $LaBr_3$(Ce) detector in the spectral gamma-ray logging probe. A spectral gamma-ray logging probe using a small 1-inch diameter x 1-inch height $LaBr_3$(Ce) detector was developed to perform gamma-ray spectroscopy in slim borehole environments. The probe was attached to a vehicle-mounted multi-para borehole logging system. The probe was calibrated using gamma-ray sources of known energies and standard boreholes with known uranium, thorium, and potassium concentrations. The spectral gamma-ray logging was performed in a borehole with a radioactive zone around the Sarangapalli area, Guntur district of Andhra Pradesh (India). The logging results were compared with laboratory core sample analysis results to confirm the credibility of the probe's ability to measure K, U, and Th concentrations in a drilled borehole.

Keywords: $LaBr_3$(Ce) detector, Spectral logging, Probe calibration, Uranium exploration, Radioactive zone

INTRODUCTION

In mineral exploration, drilled boreholes are crucial to assess the presence of minerals in the subsurface. Various logging probes are employed to log the drilled boreholes and evaluate the subsurface information. These probes provide important information regarding the geological formations, mineral composition, fluid content and other properties crucial to assessing potential mineral deposits. A spectral gamma-ray logging probe is one such critical probe, used in uranium exploration. This probe measures the natural gamma radiation, emitted by radioisotopes of elements, mainly potassium (K), uranium (U), and thorium (Th) in the subsurface. It helps to identify and quantify radioactive minerals, especially uranium-bearing minerals, which indicate potential ore bodies. In order to perform the logging activity in the drilled borehole, the probe's diameter must be smaller than the borehole diameter so that it may be lowered into the borehole freely and perform measurements effectively. The diameter of coring boreholes varies significantly depending on the geological formation, drill depth, and exploration objective. Therefore, small-size NaI(Tl) detectors were used in traditional spectral gamma-ray logging probes resulting in reduced sensitivity and increased contributions from high-energy thorium in uranium and potassium channels (Jegannathan et al., 2018). The $LaBr_3$(Ce) detector has several advantages over NaI(Tl) detectors of the same size. The improved energy resolution of the $LaBr_3$(Ce) detector, results in sharp energy peaks compared to the NaI(Tl) spectra (ORTEC, 2023). This reduces the high-energy thorium contributions in uranium and potassium channels. The $LaBr_3$(Ce) scintillator exhibits a high density (5.2 g/cm^3), high light yield (~ 68000 photons/ MeV), energy resolution (3-4% at 662 keV), decay time (16 ns), excellent thermal stability and higher detection efficiency than the NaI(Tl) scintillator (epic-crystal.com). Many researchers have studied the application of $LaBr_3$(Ce) scintillation detector for gamma-ray spectrometry (Dias et al., 2009; Saizu and CATA-DANIL, 2011; Loher et al., 2012) and found it suitable**.** As a result, the $LaBr_3$(Ce) detector was selected to develop a suitable spectral gamma-ray probe for spectral logging of drilled cored boreholes for uranium exploration. Indigenously developed spectral logging systems are economical and have full control over the system for repair, maintenance, and calibration.

High-purity Germanium (HPGe) detectors offer superior energy resolution, compared to $LaBr_3$ and NaI detectors. HPGe detectors require cryogenic cooling and operate at temperatures between 90-120 K. This cooling is achieved using a combination of a cryostat, dewar, and liquid nitrogen. Therefore, the HPGe detector is not preferable for borehole logging applications. The comparison of LaBr3(Ce), NaI(Tl), and HPGe spectra is illustrated below (Figure 1).

DEVELOPMENT OF SPECTRAL GAMMA-RAY LOGGING PROBE USING $LaBr_3$(Ce) DETECTOR

In order to achieve a smaller probe diameter, including the detector protective enclosure and metal probe case diameters, a hermetically sealed $LaBr_3$(Ce) crystal of diameter 1-inch x 1-inch length (EPIC make), coupled with a suitable photo

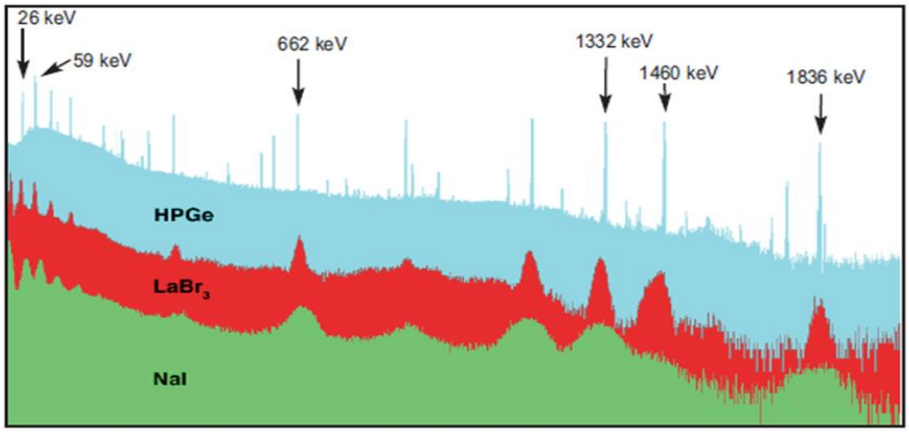

Figure 1. Comparison for 3 inch x 3 inch LaBr3(Ce), 3inch x 3 inch NaI(Tl), and HPGe spectra (ORTEC, 2023).

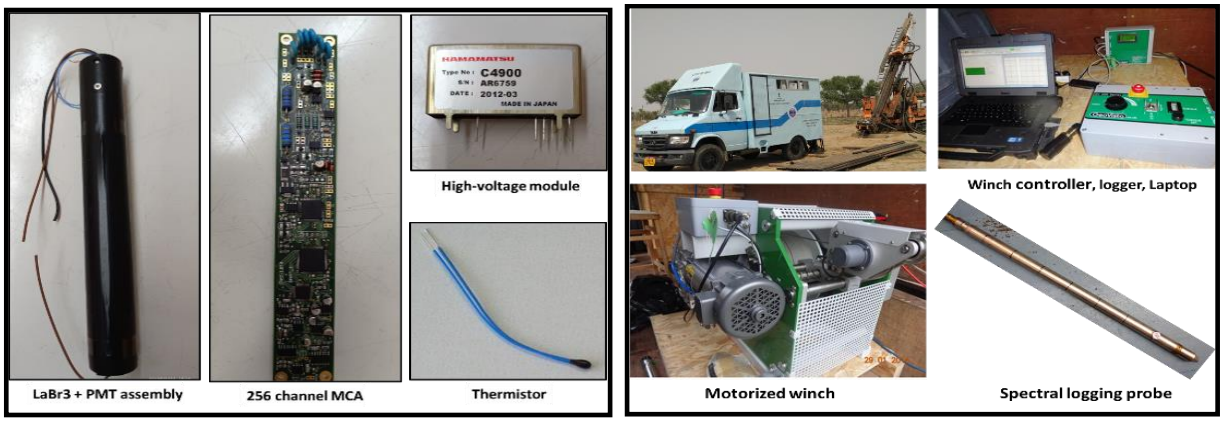

Figure 2. Internal components of spectral logging probe and multi-para logging system.

multiplier tube (Hamamatsu make), was used in the probe along with a 256-channel multi-channel analyser (MCA). A thermistor was attached to the detector for temperature compensation. Data was collected and recorded using a vehicle-mounted motorised winch and Geovista, UK logger unit coupled to a laptop (Figure 2). The detector and photo-multiplier unit transform the incident gamma ray into an electric pulse. The amplitude of the pulse is proportional to the incident gamma ray energy. The 256-channel multi-channel analyzer (MCA) segregates the gamma-ray events depending on pulse height and assigns a specific channel to each pulse height range. The surface electronics receive and store the data in the respective channels.

CALIBRATION

Energy scale calibration

In gamma-ray spectroscopy, calibrating the energy scale involves establishing a relationship between the energy of gamma rays emitted by specific isotopes and the corresponding channel numbers on the detector's spectrum. The energy calibration was performed by exposing the detector to known energy gamma-ray sources. The radioactive isotopes viz., cesium-137 (662 keV), cobalt-60 (1173 keV and 1332 keV) and thorium (Tl-204; 2620 keV) were used for the energy scale calibration.

The spectral probe was exposed to these radioactive isotopes and counts were recorded for 200 seconds. The gamma-ray spectrums with the x-axis representing channel numbers and the y-axis representing counts or intensity of the gamma-ray were plotted. The ^{137}Cs spectrum peak of 662 keV was observed at channel #51 (Figure 3). The ^{60}Co spectrum peaks of 1173 keV and 1332 keV energies were observed at channel #89 and channel #103 respectively (Figure 4). The thorium (^{232}Th) and its decay chain include several daughter products that emit gamma rays. One prominent gamma ray emitted by thallium-208 (^{208}Tl) in the thorium decay chain, has an energy

of 2620 keV. The gamma-ray with an energy of 2620 keV was detected and registered at channel #200 in the thorium gamma-ray spectrum recorded by the spectral gamma-ray probe (Figure 5).

The above channel numbers of known peaks of ^{137}Cs, ^{60}Co, and ^{208}Tl (thorium daughter product) are used to calibrate the energy scale of the spectrum. The calibration factor 'channel per keV' value was computed based on the above peak position information (Figure 6). The calculated value, 0.07616 channel per keV, indicates the conversion factor between the energy of a gamma ray in keV and the corresponding channel number in the gamma-ray spectrum.

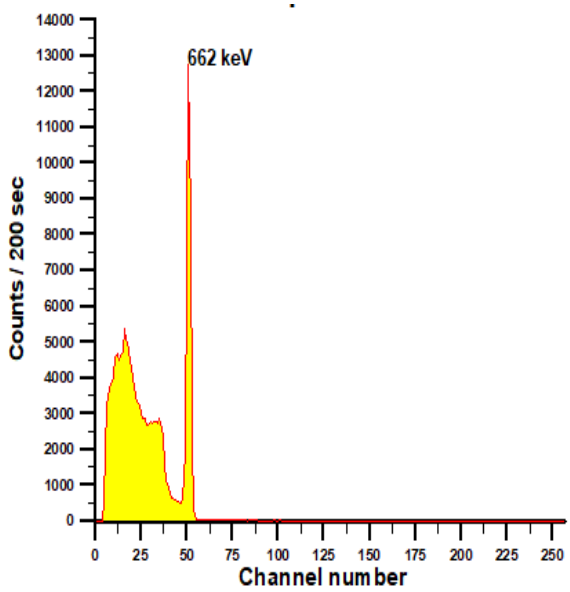

Figure 3. ^{137}Cs Spectrum recorded by $LaBr_3(Ce)$ spectral probe; 662 keV peak at Ch. # 51.

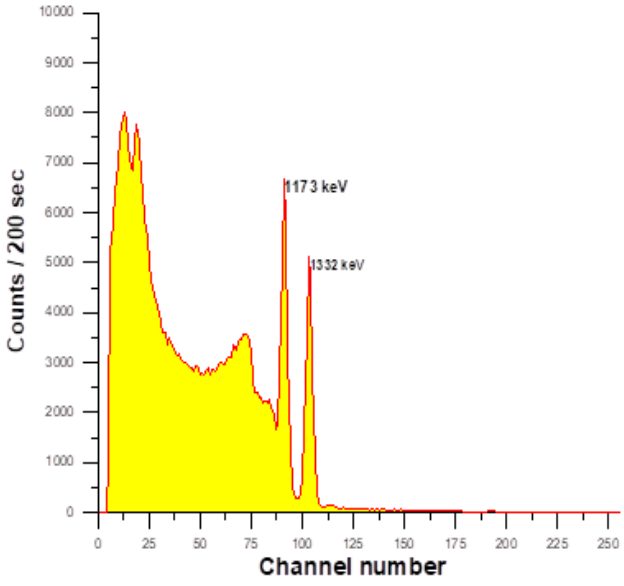

Figure 4. ^{60}Co spectrum recorded by $LaBr_3(Ce)$ spectral probe; 1173 keV peak at ch. # 89 and 1332 keV peak at ch.# 103.

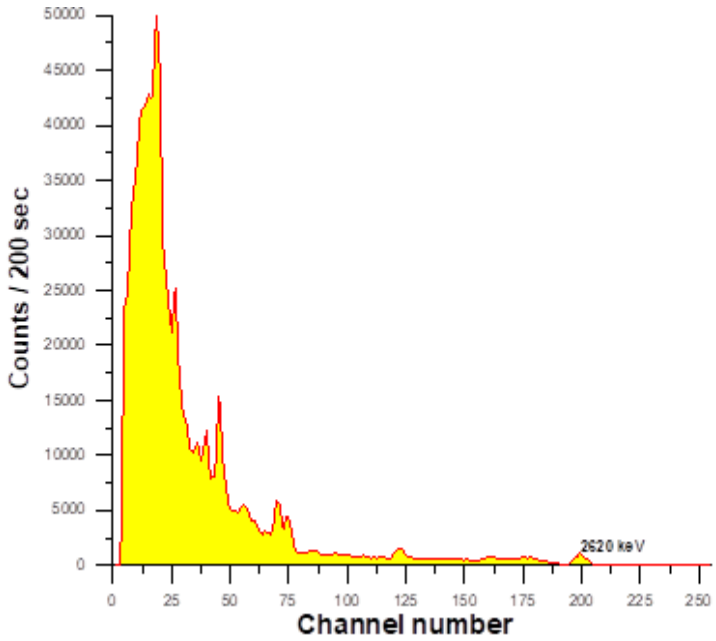

Figure 5. Thorium spectrum recorded by $LaBr_3(Ce)$ spectral probe; 2620 keV peak at ch. # 200.

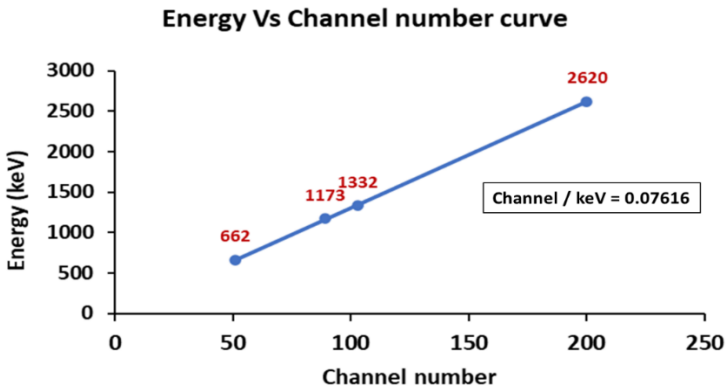

Figure 6. Energy calibration curve of $LaBr_3$(Ce) spectral probe.

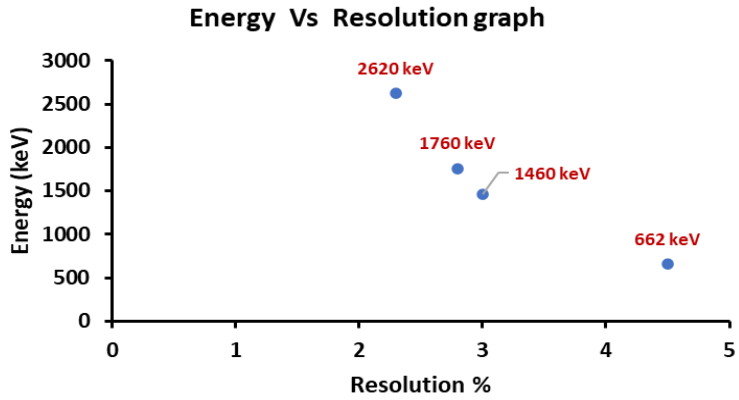

Figure 7. Resolution versus energy graph of $LaBr_3$(Ce) spectral probe.

This helps in identifying unknown peaks and quantifying the energy of the detected gamma rays. To convert from channel number to energy (keV), the channel number should be multiplied by the calibration factor

To find out the presence of potassium (K), uranium (U), and thorium (Th) content in the drilled borehole using the spectral gamma-ray probe, the intensity of gamma rays emitted at specific energies associated with these elements should be measured. Potassium-40 (^{40}K) emits gamma rays with 1460 keV energy. The ^{214}Bi is part of the uranium (^{238}U) decay chain and emits gamma rays with 1760 keV energy. Thorium (^{232}Th) decay chain member, thallium (^{208}Tl) emits gamma rays with 2620 keV energy. The calibration factor of 0.07616 channels per keV was used to find out the channel positions for the gamma rays with energies of 1460 keV, 1760 keV, and 2620 keV.

RESOLUTION OF THE DETECTOR

The resolution of a detector is an important parameter that describes its ability to distinguish between gamma rays of different energies. The calculation of the resolution of a detector for gamma-ray energies of interest is part of the calibration process. The calculation of the resolution of the detector at 662 keV is as follows. The peak for the 662 keV gamma-rays was observed at channel# 51 and denoted as Ch#peak. The measurement of Full Width at Half Maximum (FWHM) of the 662 keV peak in terms of channels was determined and denoted as Ch (FWHM). The resolution of the detector at 662 keV energy was calculated using the following formula

$$Resolution(R) = \frac{Ch(FWHM)}{Ch\#peak}\ X\ 100\%$$

The resolution of the detector for 662 keV energy was 4.5%.

The relative resolutions of a detector for gamma energies 1460 keV (^{40}K), 1760 keV (^{214}Bi), and 2620 keV (^{208}Tl) were calculated using the following formula:

$$\left(\frac{Resolution1}{Resolution2}\right) = \left(\frac{Energy2}{Energy1}\right)^{1/2}$$

The calculated relative resolutions are plotted against the energy (Figure 7). As the gamma ray energy increases, the resolution improves.

WINDOW WIDTH

In gamma-ray spectrometry, determining the window width for peak analysis is crucial to accurately identify and quantify different gamma-ray energies. The process involves calculating the standard deviation (σ) of the peak in the spectrum. The standard deviations (σ) of 1460 keV, 1760 keV and 2620 keV gamma energy peaks were calculated using the following formula.

$$Resolution = \frac{FWHM}{peak\ energy} = \frac{2.35\ б}{peak\ energy}$$

Gamma-ray peaks typically have a Gaussian shape due to the statistical nature of the detection process. The Gaussian distribution is characterized by its mean (centre of the peak) and standard deviation (σ). The standard deviation is the measure of the width of the peak. The window width is set to the multiplier of the standard deviation. In order to cover about 99.7% of the peak area under the Gaussian curve, a six-sigma (6 x σ) window width was selected to capture most of the peak's data.

STRIPPING RATIOS AND SENSITIVITIES

The stripping ratios and sensitivities are crucial parameters to quantify the gamma radiation emitted from radioactive materials in the subsurface. To determine these parameters, the three (K, U, Th) model boreholes known as primary standards available at the Atomic Minerals Directorate for Exploration and Research, Hyderabad were utilized. The primary standard simulates a borehole filled with a well-sampled and precisely analysed layer of known grade and about twice the infinite thickness in both radial direction and in height with a hole at the centre. The primary standard can be considered as a sphere with the detector placed at its centre. The probe is positioned at the centre of the borehole, and gamma-ray counts were recorded in the three windows. The spectral gamma probe stripping ratios and sensitivities obtained using the above primary standards are tabulated in Table 1.

The stripping ratios and sensitivities of the 1-inch x 1-inch $LaBr_3$(Ce) logging probe were compared with the 1-inch x 4-inch NaI(Tl) logging probe (Table 2) (Jegannathan et al., 2018). Currently, only 1-inch height and 1-inch diameter LaBr3(Ce) detectors are available in the market, so the same was used in the spectral logging probe. The NaI(Tl) detector length (height) is 4-inch whereas the $LaBr_3$(Ce) detector length is 1-inch.

The comparison of sensitivities (S_k, S_u, S_{th}) between both detectors is not precise due to the difference in sample volume exposure to each detector. Good sensitivities are important for detecting low levels of radioactivity, and spectral gamma-ray logging is used only in highly radioactive zones.

The diameter (thickness) of both detectors is the same. The 2.62 MeV gamma-ray emitted from the thorium series passes through the detector's thickness. For the gamma-ray to be fully registered and observed by the detector, it must be completely absorbed to record a count in the thorium channel. If the detector thickness is insufficient, only a portion of the gamma-ray energy will be detected, resulting in a false count in the lower energy window (uranium or potassium). The stripping ratios (α, β, γ) indicate incomplete absorption of the high-energy gamma ray and these ratios should be as low as possible. The density of the NaI(Tl) detector is 3.67 g/cm³, while the density of the LaBr3(Ce) detector is 5.2 g/cm³. Due to its higher density, the stripping ratios are improved for the LaBr3(Ce) spectral logging probe, compared to the NaI(Tl) spectral logging probe.

Casing and water corrections

Gamma rays emitted by the borehole formation get attenuated while passing through the iron casing and water column. The correction factors are used to account for the influence of iron casing and water in the borehole measurements. They are calculated as the ratios of gamma-ray counts recorded by the probe in the middle of the mineralized zone with and without casing/water in the standard borehole. The corrections were derived for different combinations of the casings and water column for gross gamma counting (Table 3).

Table 1. 1-inch x 1-inch $LaBr_3$(Ce) probe Stripping Ratios and Sensitivities.

α	β	γ	a	S_k	S_u	S_{th}
				(Cps/%)	(cps/ppm)	(cps/ppm)
1.14	1.19	1.34	0.033	0.26	0.015	0.0044

Table 2. 1-inch x 4-inch NaI(Tl) probe stripping ratios and sensitivities (Jegannathan et al., 2018).

α	β	γ	a	S_k	S_u	S_{th}
				(Cps/%)	(cps/ppm)	(cps/ppm)
1.221	1.64	1.75	0.039	0.561	0.0507	0.0178

Table 3. Casing and water corrections.

Casing type	Counts/sec	Correction factor	Thickness (mm)
Without casing	3078	1	0
AX	2438	1.26	3.15
BX	2380	1.29	4
NX	2145	1.44	4
HX	2271	1.36	4.8
AX+BX	2014	1.53	7.15
AX+HX	1923	1.60	7.95
BX+NX	1789	1.72	8
BX+HX	1889	1.63	8.8
NX+HX	1729	1.78	8.8
AX+NX	1844	1.67	7.15
AX+BX+NX	1569	1.96	11.15
AX+BX+HX	1645	1.87	11.95
BX+NX+HX	1478	2.083	12.8
AX+BX+NX+HX	1278	2.41	15.95
without casing with water	2710	1.136	39.61 (Hx)

CALCULATION OF NET WINDOW COUNTS FROM GROSS WINDOW COUNTS

The following formulas are used to calculate the net counts for the K, U and Th window gross counts.

$Th_{net} = (Th_{gross} - a.U_{gross}) / (1-a.\alpha)$

$U_{net} = (U_{gross} - \alpha. Th_{gross}) / (1-a.\alpha)$

$K_{net} = [K_{gross} - (1-a.\alpha) + Th_{gross} (\alpha.\gamma - \beta) + U_{gross} (a.\beta - \gamma)] / (1-a.\alpha)$

Where Th_{net}, U_{net} and K_{net} are the net counts Th_{gross}, U_{gross} and K_{gross}s are the gross counts in the respective windows and α, β, γ and 'a' are stripping ratios. The fine-tuning of window widths for K, U and Th windows was done using the peak positions observed in the primary standards.

STUDY OF SPECTRAL GAMMA PROBE RESPONSE IN THE CORING BOREHOLE ENVIRONMENT

A borehole drilled by the Atomic Minerals Directorate for Exploration and Research (AMD) near Sarangapalli village, Palnadu district, Andhra Pradesh state, India was selected to perform the spectral gamma-ray logging using the newly developed logging probe.

Geology of the study area

Palnad Sub-basin is located in the north-eastern part of the Cuddapah Basin. The Sarangapalle area is located in the northern part of the Palnad Sub-basin (Figure 8). It comprises of a thick sequence of arenaceous, argillaceous and carbonate sediments belonging to the Kurnool Group which is divided into six Formations viz., Banganapalle, Narji, Auk, Paniam, Koilkuntla and Nandyal Formation. The sediments of the Banganapalli and Narji formations were non-unconformably deposited predominantly over highly fractured basement granitoids in the area. The Banganapalli formation comprising conglomerate, quartzite and shale forms dissected plateaus and structural hills. Whereas, Narji formations comprising limestone, shale and siltstone form pedi-plains. The limestone beds belonging to Narji formations are sub-horizontal dipping towards SE with the dip amount ranging from 5˚ to 15˚ (Singh et al., 2017).

GROSS GAMMA RAY LOGGING OF THE DRILLED BOREHOLE

Point-to-point logging mode is appropriate for recording significant counts in the windows during spectral gamma-ray logging. Recording the data for 100 seconds at each point along the borehole is typical and necessary to ensure accurate and reliable measurements during spectral gamma-ray logging. The point-to-point logging process can significantly extend the overall duration of the logging operation, especially for deep or complex boreholes. It requires specialised logging equipment and skilled personnel to conduct point-to-point logging effectively. The combination of time and resources needed for point-to-point logging contributes to its expense. Adopting a selective logging method for spectral gamma logging can help to overcome some of the challenges associated with point-to-point logging. A gross gamma logging probe is initially used to identify a selective (radioactive) zone.

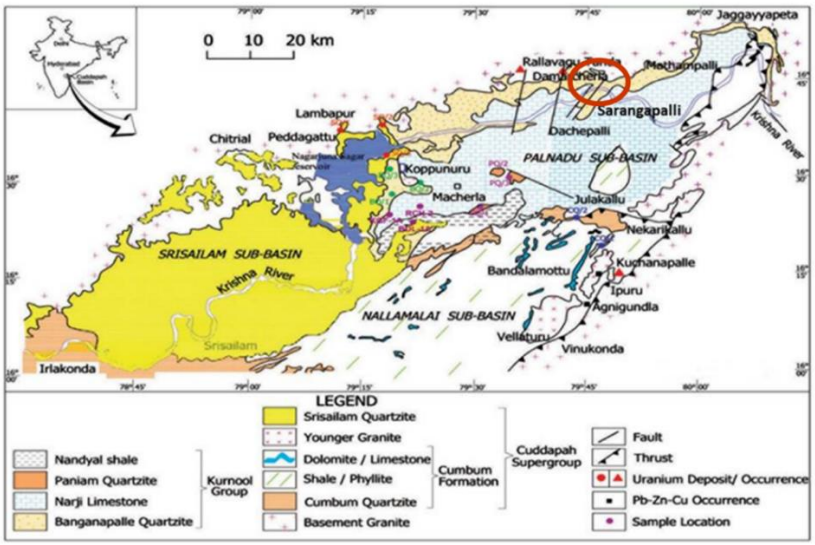

Figure 8. Geological map covering borehole location and its surrounding areas (Singh et al., 2017).

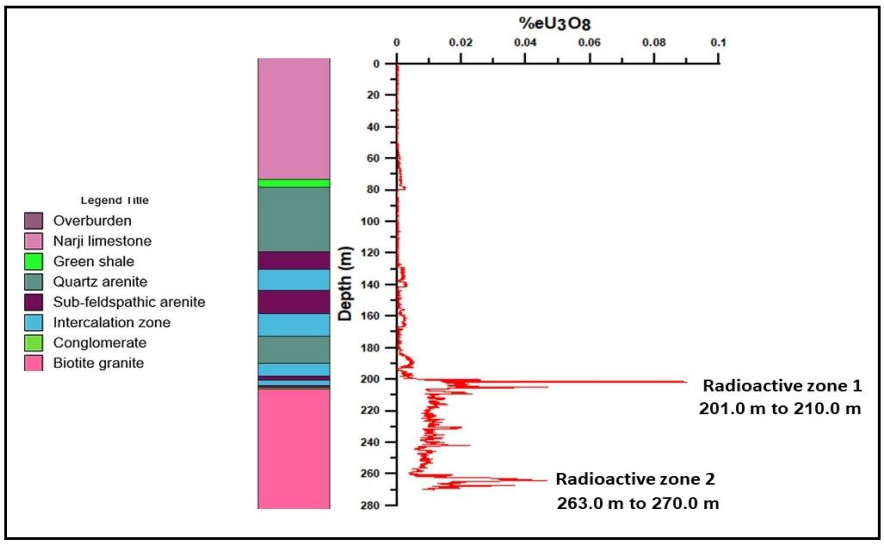

Figure 9. Total gamma-ray logging graph and lithological correlation.

This initial logging measures the total gamma radiation emitted from the formation. It indicates where potential radioactive materials are present within the borehole. The total (gross) radioactivity was measured along the borehole depth using the existing gross gamma ray logging probe in continuous logging mode up to the depth of 270.0 m. The depth versus total radioactivity log revealed two radioactive zones i.e., from 201.0 m to 210 m and 263 m to 270 m depth with a 100-ppm cut-off grade (Figure 9). These two radioactive zones were selected for spectral gamma ray logging. Top most radioactive band (201-210 m), is associated with the intercalation zone above the unconformity, while the other zone (263-270 m) is hosted by basement granite.

SPECTRAL GAMMA-RAY LOGGING OF A DRILLED BOREHOLE BY SELECTIVE LOGGING METHOD

The Slim spectral gamma ray logging probe with a Lanthanum Bromide detector was used to collect the 256-channel spectral data from the two radioactive zones in the borehole. The practice of verifying the ^{137}Cs peak centroid was followed to start the logging. The data was collected at every 10 cm interval for 100 seconds in point-to-point logging mode. An Excel sheet was created to gather the grass gamma counts in the Total, K, U and Thorium windows from 256 channels of data at each point. The stripping constants were incorporated into the Excel sheet to calculate the net

counts. The net counts were converted into concentrations using sensitivity constants.

URANIUM (RADIUM EQUIVALENT) AND THO_2 PROFILES IN THE RADIOACTIVE ZONE-1

The uranium [Radium equivalent (Ra. eq) – the daughter group of uranium series] and thorium concentrations obtained from the spectral gamma ray logging were plotted against depth (Figure 10). The plot revealed that the borehole subsurface from 202.5 m to 203.5 m depth, is rich in uranium (Ra. eq) concentration. The maximum concentration of around 0.060% of Ra. eq was recorded at 202.8 m depth. The thorium concentrations in this depth range are negligible. The Ra. eq was also recorded in the borehole from 205.9 m to 206.9 m depth range and the concentrations varied from 0.010% to 0.024%. Thorium is also present at this depth range with a concentration of 0.010%. Thus, the spectral gamma ray logging revealed two zones of interest in the borehole i.e., one pure uranium (Ra. eq) zone and the second one is a mixed zone of uranium (Ra. eq) and thorium (Figure 10).

COMPARATIVE STUDY

Uranium (Ra. eq) comparison

The spectral logging data was compared with the data analyzed from laboratory on core samples by gamma ray spectrometry method. A 30 cm depth shift was observed between the above two data sets. The depth shift was corrected and both the data sets were plotted as a function of depth. The uranium (Ra. eq) profile obtained from the laboratory core sample analysis is similar to the spectral gamma logging profile and it provides a strong confirmation of the reliability of the logging results (Figure 11).

ThO_2 COMPARISON

The concentrations of ThO_2 recorded by the spectral gamma ray logging in the pure uranium zone (zone 1a) are less than 0.010%. These values are consistent with laboratory measurements, suggesting that the field data reflect the thorium levels in that zone. The spectral gamma-ray logging recorded the thorium concentrations in the mixed zone (zone 1b) varying from 0.010% to 0.016%. The laboratory core samples analysis confirms the thorium concentrations in the mixed zone ranging from 0.010% to 0.030% (Figure 12). Thus, the presence of the thorium mineralisation identified by spectral gamma-ray logging besides laboratory analysis, confirms consistency in the data sets. The small size detector in the spectral logging probe might not capture all the high energy (2062 keV) gamma radiation, leading to under-estimation of the thorium concentrations. The higher thorium concentrations in the laboratory analysis data than that of logging values are attributed to the small size detector used in the spectral logging probe.

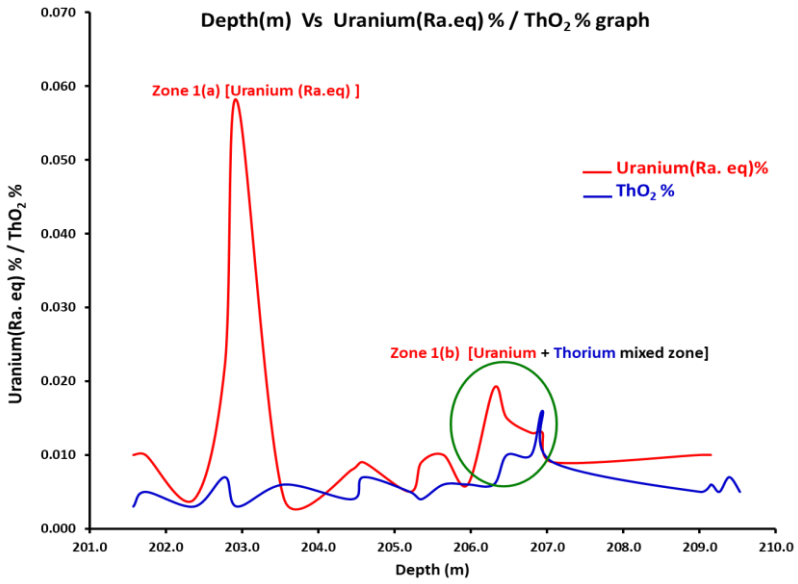

Figure 10. Uranium (Ra. eq) and thorium profiles in the radioactive zone -1.

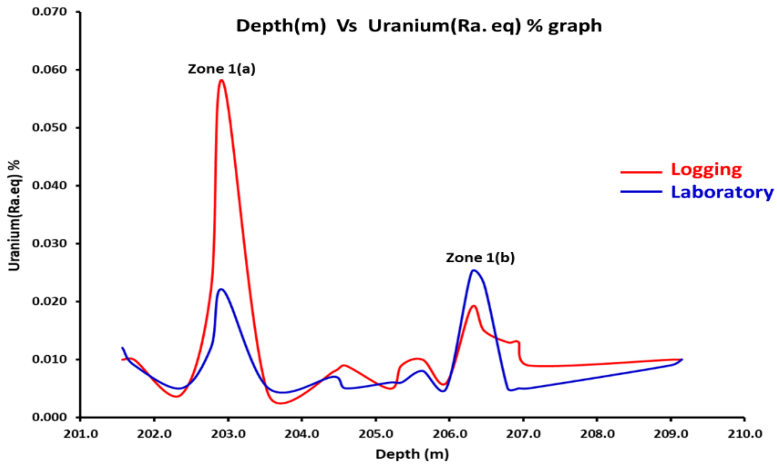

Figure 11. Uranium (Ra. eq) profiles of logging and laboratory data.

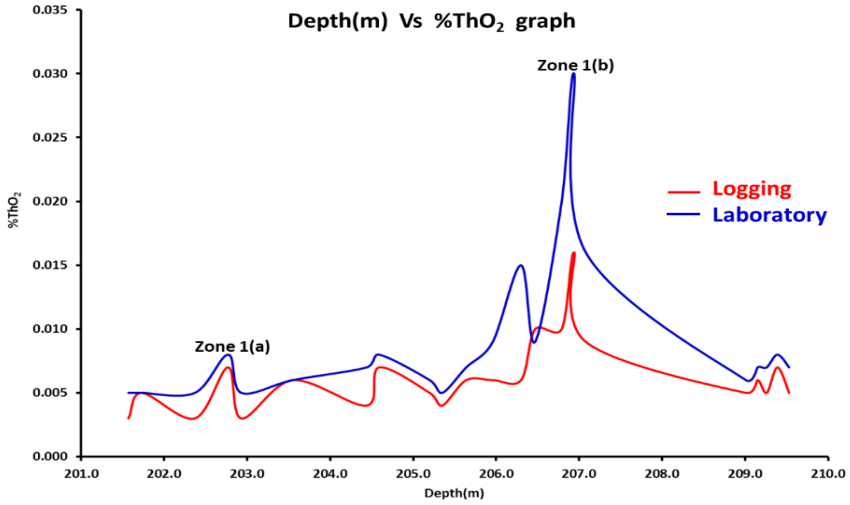

Figure 12. Tho_2 profiles of logging and laboratory data.

The subsurface formation contains radioactive materials (like uranium and thorium) that are unevenly distributed, making direct point-to-point comparisons inappropriate. Estimating uranium levels in zones where thorium is also present can be complicated due to the interference of thorium's radioactivity. However, the uranium estimations made under such conditions (despite thorium's presence), are reasonably comparable to laboratory measurements in the radioactive zone (Table 4).

POTASSIUM PROFILE IN THE RADIOACTIVE ZONE -1

The 1436-keV gamma-ray emitted by a naturally occurring ^{138}La radioisotope contributes to the internal radioactivity of the $LaBr_3(Ce)$ detector**.** This gamma ray is indistinguishable from the 1461-keV gamma ray emitted by the ^{40}K isotope because of the detector energy resolution constraints. In order to isolate the ^{40}K gamma rays, background data was recorded for 500 seconds at a standard borehole barren area and subtracted from the potassium window counts.

The potassium concentrations recorded by the spectral gamma-ray logging ranged from 0.1% to 4.8% in the radioactive zone- 1 of the borehole (Figure 13). The rock type in the radioactive zone is biotite granite. The granite core samples collected from the barren zone of the borehole were analysed in the laboratory for potassium concentrations. The potassium concentration ranges reported by the laboratory in the granite rock of the Sarangapalli area, vary between 3.3% and 6.9%. The maximum K concentration recorded by spectral gamma-ray logging (4.8%) did not exceed the maximum K value of sample analysis data even in the presence of uranium and thorium.

K ESTIMATION BY SPECTRAL LOGGING IN THE PRESENCE OF URANIUM AND THORIUM

The spectral logging recorded 0.060% of uranium (Ra. eq), 0.4% of K and 0.002% of thorium at 202.8 m depth and 0.011% of uranium (Ra. eq), 1.7% of K and 0.016% of thorium at 206.7 m depth in the borehole. The low to moderate potassium concentrations (0.4% & 1.7%), indicate that the estimation of potassium by spectral logging was not significantly influenced by the presence of uranium (Ra. eq) and thorium.

Table 4. Comparison of spectral logging data and borehole core samples analysis data (Laboratory Gamma-ray spectrometry method).

	Spectral logging data	Borehole core samples analysis data (Laboratory Gamma-ray spectrometry method)	Spectral logging data	Borehole core samples analysis data (Laboratory Gamma-ray spectrometry method)
Depth (m)	Uranium (Ra. eq)%	Uranium (Ra. eq)%	ThO_2%	ThO_2%
201.6	0.010	0.012	0.003	0.005
201.7	0.010	0.009	0.005	0.005
202.4	0.004	0.005	0.003	0.005
202.8	0.022	0.012	0.007	0.008
202.9	0.058	0.022	0.003	0.005
203.6	0.004	0.005	0.006	0.006
204.4	0.008	0.007	0.004	0.007
204.6	0.009	0.005	0.007	0.008
205.2	0.005	0.006	0.005	0.006
205.4	0.009	0.006	0.004	0.005
205.6	0.010	0.008	0.006	0.007
206.0	0.006	0.005	0.010	0.010
206.3	0.019	0.025	0.010	0.015
206.5	0.015	0.023	0.010	0.010
206.8	0.008	0.005	0.010	0.020
206.9	0.007	0.005	0.016	0.030
207.1	0.006	0.005	0.010	0.016
209.0	0.010	0.009	0.005	0.006
209.2	0.010	0.010	0.006	0.007

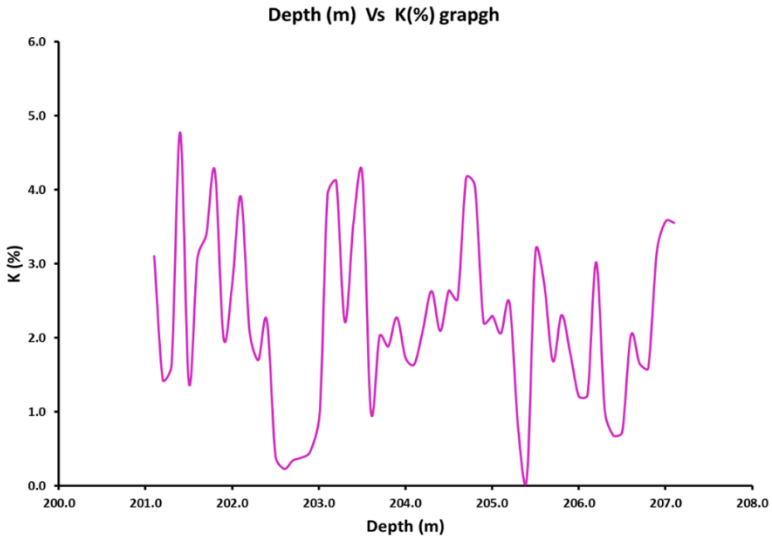

Figure 13. Potassium profile graph in radioactive zone -1.

RESULTS AND DISCUSSIONS

The borehole was logged in the Sarangaplli area using a spectral logging probe ($LaBr_3$) in situ measurements. The spectral logging recorded the pure uranium (Ra. eq) and mixed (U + Th) anomalous zones. The results indicated that the spectral logging probe distinguished the U and Th in the mixed anomalous zone. The potassium estimation by spectral logging was not significantly influenced by the presence of uranium (Ra. eq) and thorium. The spectral gamma-ray logging results were reasonably comparable with the laboratory analysis reports. The study confirms the credibility of the probe's capability to measure K, U, and Th concentrations in geological materials contributing to more reliable geological interpretations and resource evaluations. The spectral gamma-ray logging provides results right after the completion of logging of a borehole. This imminence allows for quick decision-making regarding the next steps in planning the boreholes. This efficiency is crucial in exploration activities where timely decisions can i0000mpact the overall progress and success of the project. The data obtained from spectral gamma-ray logging can be used to correlate boreholes drilled across the exploration block. Spectral logging results help to understand the spatial distribution of K, U, and Th concentrations, aiding in planning further exploration.

CONCLUSIONS

The lanthanum bromide ($LaBr_3$) detector with a 1-inch diameter and 1-inch length for spectral gamma-ray logging probe is suitable for qualitative measurements, especially for narrow boreholes. The spectral probe performance can be improved further by using a 1-inch diameter and 3-inch or 4-inch length lanthanum bromide detector. The concentrations recorded by the spectral logging are not point-to-point comparable with the laboratory concentrations (qualitative analysis). The sample volume and the detector sizes are different in both methods; therefore, correlation studies are not feasible. The $LaBr_3$ detector balances practicality with ensuring accurate and reliable measurements of gamma-ray emissions for geological exploration and analysis. The qualitative distinction of uranium and mixed (uranium + thorium) anomalous zones through spectral logging in the Sarangapalli area is useful in advancing the exploration program.

ACKNOWLEDGEMENT

The authors are very grateful to Sri Dheeraj Pande, Director, AMD and Dr Prakhar Kumar Additional Director (OP-II), Atomic Minerals Directorate for Exploration and Research, Hyderabad for permitting this paper's publication. The authors are also grateful to Shri A. Markandeyulu, Head, Exploration Geophysics Group and Smt. A. Meenakshi Sundari, Head, Instrumentation, AMD for consistent encouragement. Sincere thanks to the officers of the exploration team of the Sarangapalli area and all my colleagues for their valuable suggestions.

Author Contributions

Habeeb Ali Khan: Spectral probe development, calibration, manuscript writing; Srinivaslu: Data acquisition, processing, manuscript writing; A. Markandeyulu: conceptualization, manuscript writing; G. Udaya Laxmi: manuscript writing; M.N. Chary: manuscript writing; Prakhar Kumar: Geology and lithological inputs

Data Availability

Data can be made available on reasonable request from the corresponding author.

Compliance with Ethical Standards

The authors declare that they have no conflict of interest and adhere to copyright norms.

References

Jegannathan, G., Velusamy, V., Reddy, B.R. and Sharma, P.K., 2018. Spectral gamma ray logging: A cost-effective method for uranium exploration. Radiat. Prot. Environ., 41, 42-6

ORTEC, 2023 . Lanthanum Bromide Scintillation Detectors. product catalogue

Dias, F.C., Grund, M.S., Renha Jr. G., Galdoz, E. G., Christallini, O. and Facchinetti, M., 2009. The use of Lanthanum Bromide Detectors for Nuclear Safeguards Applications. Int. Nuclear Atomic Conf. –INAC 2009. https://api.semanticscholar.org/CorpusID:202115762

Saizu, M.A. and CATA-DANIL, G., 2011. Lanthanum Bromide scintillation detector for Gamma spectrometry applied in internal radioactive contamination measurements. U.P.B. Sci. Bull., Series A, 73(4), 119-126.

Loher, B., Savran, D., Fiori, E., Miklavec, M., Pietralla, N. and Vencelj, M., 2012. High count rate γ-ray spectroscopy with $LaBr_3$:Ce scintillation detectors. Elsevier, 1-8. https://doi.org/10.48550/arXiv.1202.6495

Singh, R.V., Sarbaina, C., Basu, H., Venkateshwarlu, M., Banerjee, R., Singh, Y. and Verma, M., 2017. Geochemical characterization of quartzites of the Srisailam, Banganapalle and Paniam formations from the northern part of the Cuddapah Basin, Telangana and Andhra Pradesh. J. Appl. Geochem., 19(1), 34-43.

Received on: 20-08-2024 ; Revised on: 04-11-2024 ; Accepted on: 06-11-2024

J. Ind. Geophys. Union, 29(1) (2025), 12-25
https://doi.org/10.71122/JIGU.29(1)2025.002

Petrographic study of Umlatdoh limestone in parts of Meghalaya, north-east India with an emphasis on diagenetic and depositional attributes

Anni Rani Das, Meghali Baruah*, Mrinal Kanti Pathak, Devesh Walia and Shikhar Kumar
Department of Geology, North-Eastern Hill University, Shillong – 793022 (India)
*Corresponding author: meghaligeo33@gmail.com

ABSTRACT

Early Eocene Umlatdoh Limestone of Sylhet Limestone Group have been studied to understand their framework constituents and diagenetic processes. Additionally, an approach was made to infer the depositional environment of this limestone based on the abundance of biogenic assemblages. Two vertical profile sections were measured and representative rock samples were collected for petrographic study. The limestones of the study area are classified as wackestone, packstone and grainstone, dominated by calcareous green algae (Dasycladalean algae) and large benthic foraminifers. An open lagoonal to proximal middle shelf environment has been envisaged during the deposition of the studied limestone. The diagenetic overprints of these limestones are characterized by several key diagenetic features, including micritization, cementation, compaction, dissolution and neomorphism. These diagenetic processes occurred in marine phreatic, meteoric phreatic, mixed meteoric phreatic, and burial diagenetic environments. Micritization of allochems, cementation by isopachous and granular calcite, neomorphism, and bioclast recrystallization occurred during meteoric-phreatic diagenesis. Meteoric-vadose diagenesis led to extensive dissolution and the infilling of fractures with sparry calcite. During burial diagenesis, blocky calcite cementation appears to have become prominent.

Keywords: Umlatdoh Limestone, Meghalaya, Petrography, Diagenesis, Depositional environment

INTRODUCTION

The Sylhet Limestone Group is well known for its captivating lithology as developed in the Cherrapunjee area of Meghalaya, Northeast India. Thick alternating carbonate and siliciclastic sequences, ranging in age from Late Palaeocene to Middle Eocene (Tewari et al., 2010a,b; Ghosh and Sarkar, 2013; Sarkar, 2015a,b, 2016) characterize the group. Larger benthic foraminiferal (LBF) assemblages and calcareous algae, dominate the carbonate sequences. Although the larger benthic foraminiferal (LBF) assemblages from Palaeogene succession of Meghalaya have been correlated with both the Tethyan and Indo-Pacific provinces (Jauhri, 1994; Jauhri et al., 2016), very little is known about their palaeo-environmental implications, including enormous development of carbonate build-ups, and large accretion of marine biota (Saraswati et al., 2018; Srivastava and Singh, 2019). Further, abundance of biogenic assemblages in shallow water carbonate depositional systems is substantially influenced by environmental factors like tides, waves, and occasional storms (Boothroyd, 1985; Hallock and Glenn, 1986; Jones and Hunter, 1992; Scoffin, 1993; Li et al., 1997, 1998; Shaghude et al., 2002; Gischler et al., 2003; Beavington-Penney and Racey, 2004; Wilson et al., 2010). The present study aims to identify different biogenic assemblages as well as various diagenetic attributes preserved in the Early Eocene Umlatdoh Limestone (Sylhet Limestone Group), employing microscopic analysis (Adams and MacKanzie, 1998) and their interpretation in terms of diagenetic vis-à-vis depositional environments.

GEOLOGICAL SETTING OF THE STUDY AREA

The study area forms a part of the southern Shillong Plateau and includes localities surrounding Wahrew Bridge of Meghalaya (25°10´50.68´´- 25°10´50.70´´ N; 91°45´52.67´´-91°45´51.57´´ E; Figure 1). The Shillong Plateau is a northeastern extension of the Peninsular India which is bounded by E-W trending Brahmaputra Fault system to the North and the Dauki Fault to the south. The N-S trending Jamuna Fault defines the western limit while eastern margin of the plateau is marked by NW-SE Kopili Fracture zone (Evans, 1964; Desikachar, 1974; Acharyya et al., 1986; Nandy, 1986; Gupta and Sen, 1988; Ray et al., 2011; Nandy, 2017). The Southern Shillong Plateau is covered by Cretaceous and Cenozoic sedimentary deposits forming a raised topography in the foreland of the Himalayas (Nagappa, 1959; Garg and Jain, 1995; Biswas et al., 2007; Kalita and Gogoi, 2015; Najman et al., 2016). Overlying conformably the Cretaceous cover, Southern Shillong Plateau spectacularly exposes the complete Paleocene -Eocene succession (Table 1) (Sarkar, 2020).

The Therria sandstone comprising intercalated sandstone – shale with minor coal units, marks the beginning of Tertiary succession. The Sylhet Limestone Group divisible into lower Lakadong, middle Umlatdoh, and upper Prang Formations conformably overlies the Therria sandstone. The lower and middle divisions of the Sylhet Limestone are comprised of calcareous (lower) and arenaceous (upper) members, while youngest Prang Formation is predominantly calcareous. Further, the three formations of Sylhet Limestone Group are considered to have resulted in response to three successive marine transgressions during the late Paleocene, early Eocene, and the middle Eocene periods respectively. The late Eocene Kopili Formation on the top, marks the closer of Tertiary succession in the region (Jauhri, 1994, 1998; Sarkar, 2020).

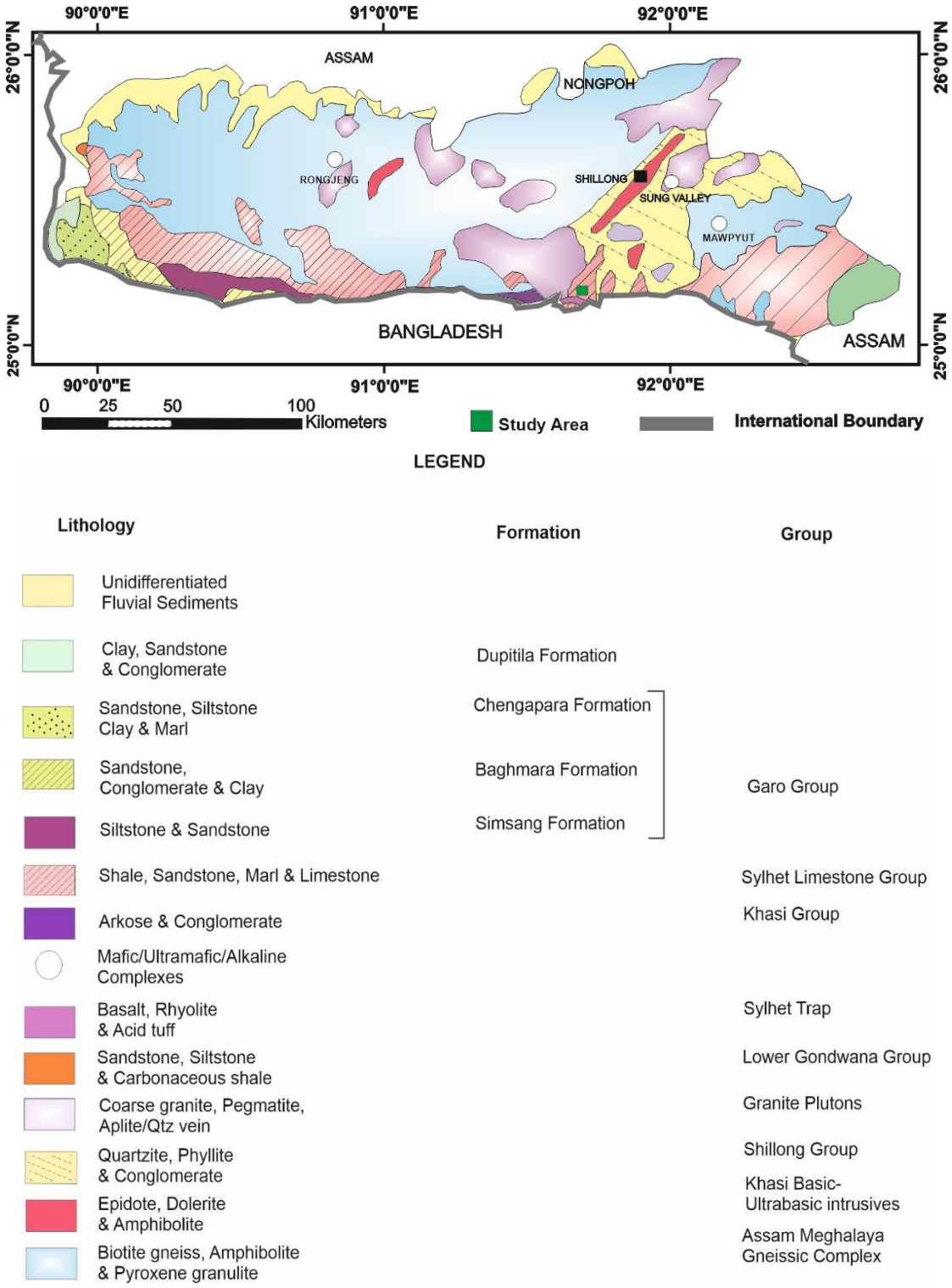

Figure 1. Generalized geological map of the Shillong Plateau, Northeast India, showing location of the study area (modified after Sahoo et al., 2024).

The study area comprises of Umlatdoh Formation, divisible into lower Umlatdoh Limestone and upper Narpuh Sandstone (Nagappa, 1959; Mehrotra and Banerji, 1973; Jauhri and Agarwal, 2001; Sarkar, 2016, 2020) members. The Umlatdoh Limestone (Figure 2 a–d) around which the present study is centred, displays 2-6 meters thick algal – foraminiferal carbonate with occasional dolomite.

Table 1. Lithostratigraphic succession of the study area (after Sarkar, 2020)

Age	Lithostratigraphic unit		Lithology
Late Eocene	*Kopili Formation*		Alternations of shale and sandstone
Middle Eocene	Sylhet Limestone Group	*Prang Formation*	Highly fossiliferous limestone with abundant large nummulitids, alveolinids, and orthophragminids
Early Eocene		*Umlatdoh Formation* Narpuh Sandstone Umlatdoh Limestone	Arkosic, ferruginous sandstone (with no foraminifera) Hard, massive limestone rich in benthic foraminifera
Late Palaeocene -earliest Eocene		*Lakadong Formation* Lakadong Sandstone Lakadong Limestone	Soft, friable, buff colored sandstone with coaly horizons Hard, compact limestone with abundant larger foraminifera
Late Palaeocene	*Therria Sandstone*		Medium to - coarse grained sandstone, shale with minor coal units
Early Palaeocene	*Langpar Formation*		Calcareous shale with limestone bands

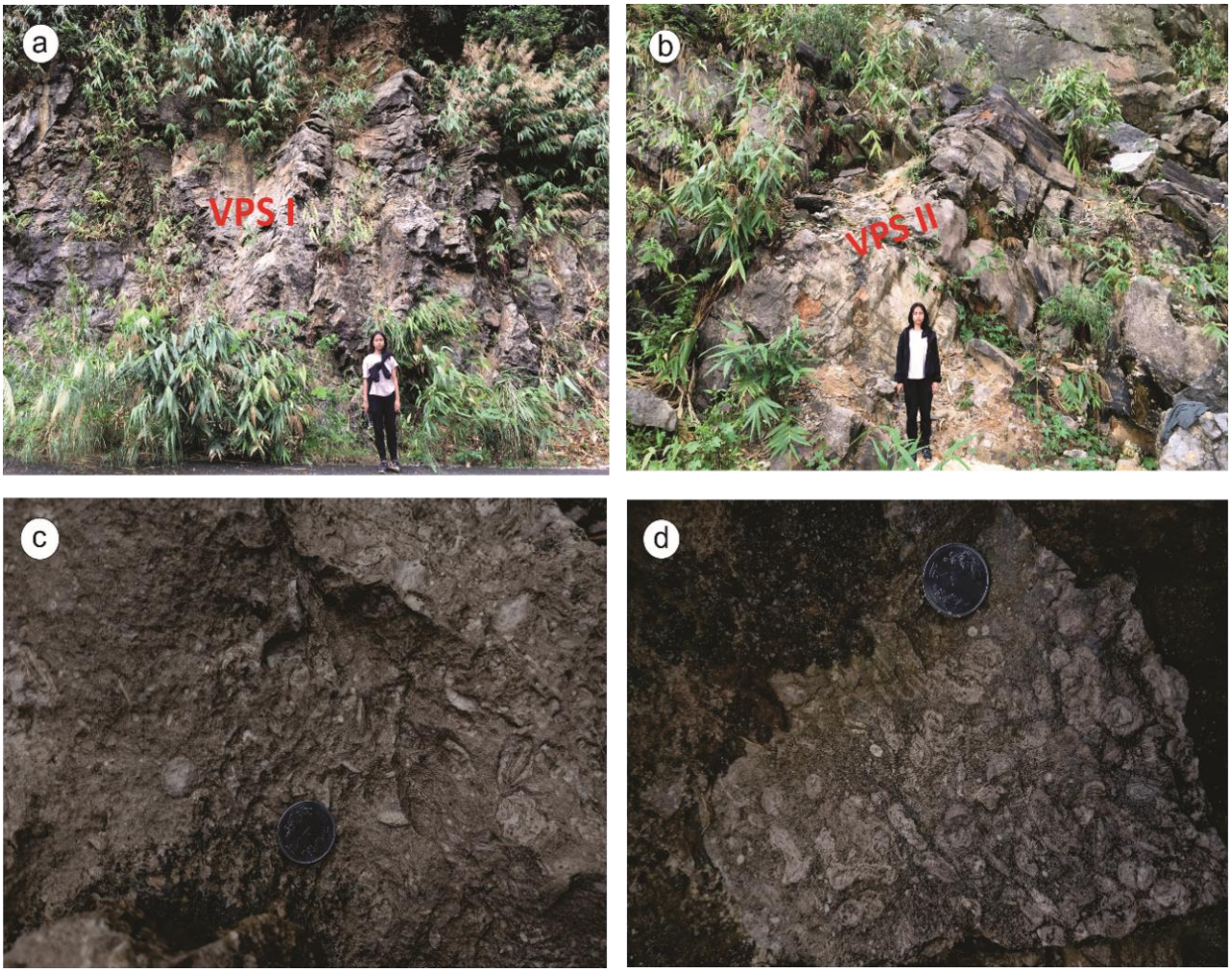

Figure 2. (a) and **(b)** Field photographs showing outcrops of Umlatdoh Limestone used in the measurement of vertical profile sections (VPS – I & II). (**c**) and **(d)** depicts parallel layering of fossil Nummulites in hand specimens.

METHODOLOGY

Two outcrop locations along the road cuttings near Wahrew Bridge, Sohbar (Figure 2a,b) were identified for detailed measurements and recording of vertical profile sections. Based on textural and lithological variations, colour, nature of bedding etc. two vertical profile sections were documented (Figure 3a,b) besides collection of samples in time and space. Thin sections were prepared for the purpose of detailed microscopic analysis using Euromax research microscope at the Department of Geology, North Eastern Hill University, Shillong. The Umlatdoh Limestones were then classified using the classification scheme after Dunham (1962).

RESULTS

Petrography

Based on the classification scheme after Dunham (1962), Umlatdoh Limestone were classified as wackestone, packstone and grainstone (Figure 4 a-d), the major components of these limestones being skeletal grains, non-skeletal grains, and cement including micrite and sparry calcite.

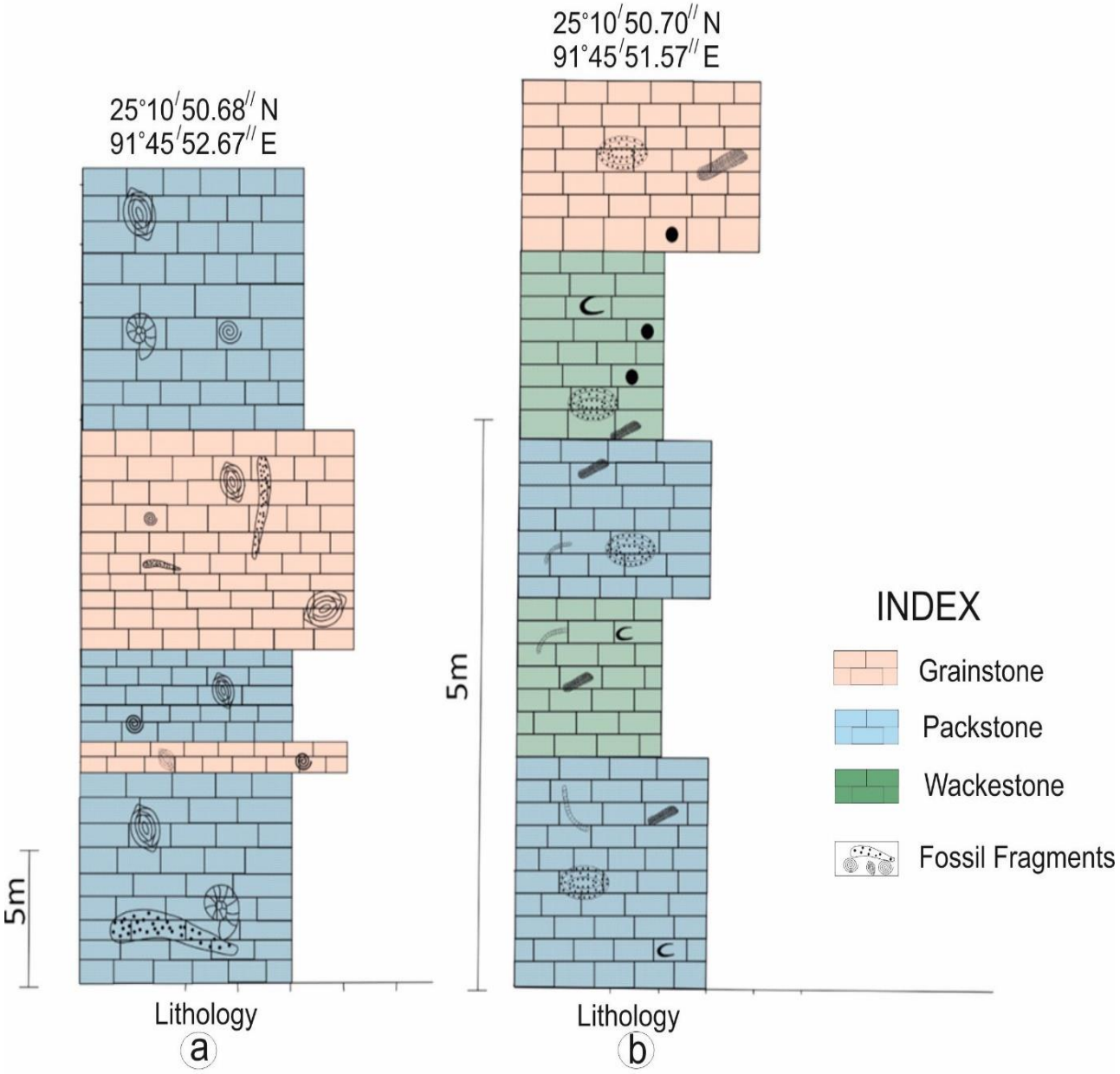

Figure 3. (a) and **(b).** Vertical profile sections of Umlatdoh Limestone recorded near Wahrew Bridge, Sohbar, Meghalaya.

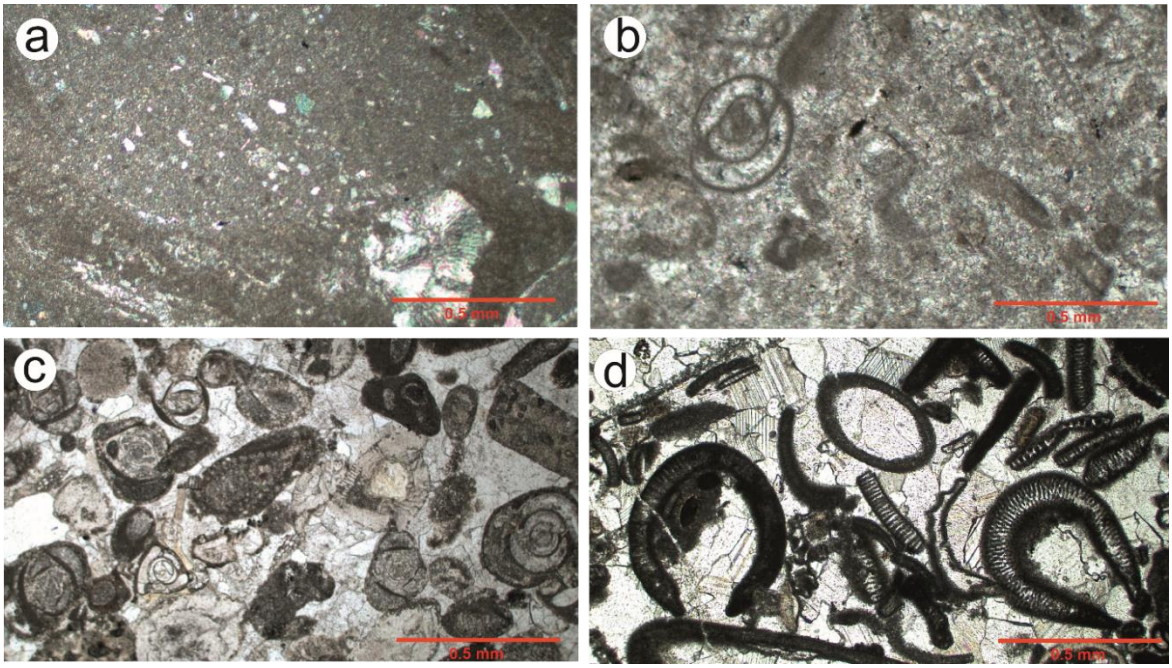

Figure 4. Photomicrographs of Umlatdoh Limestone showing **(a)** Wackestone and neomorphism of bioclasts (XPL), **(b)** Packstone and neomorphism of bioclasts (PPL), **(c)** Miliolid Grainstone (PPL) and **(d)** Algal Grainstone (PPL).

Skeletal grains

Skeletal grains are mostly comprised of large benthic foraminiferal remains including Nummulites sp. (Figure 5a), Assilina sp. (Figure 5e), Alveolina sp. (Figure 5b), Discocyclina sp. (Figure 5c), Biloculina sp. (Figure 5d), Quniqueloculina sp. (Figures 5f & 6i), Periloculina sp. (Figure 6h) and Lockhartia sp. (Figure 6g). Dasycladalean algae appears abundantly in almost all the thin sections (Figure 6 a–f). Shell structures are generally well preserved, yet a few skeletal grains are filled with sparry calcite.

Non-skeletal grains

Non-skeletal grains mainly consist of intraclasts, ooids, and peloids. Aggregates bounded by organic matter or several carbonate particles, cemented together by microcrystalline cement, can also be observed. Intraclasts, thus present, are fragments of lithified or partly lithified carbonate sediments (Figure 5g). Lithified or partly lithified irregularly shaped discrete carbonate fragments of varied sizes have been termed as intraclast (Azizi et al., 2014). These also occur as composite grains bounded together by organic matter as well as microcrystalline carbonate cement (Figure 5g).

Ooids, in the studied thin sections, occur as more or less spherical bodies having 2 mm diameter with concentric rims around a nucleus (Figure 5g, h). Cylindrical to elliptical grains of micritic composition ranging between 0.1-0.2 mm in diameter have been identified as of peloids (Figure 5g).

Diagenesis

Diagenesis refers to all those processes leading to destruction, dissolution and formation of new minerals in sediments simultaneous to or slightly after burial till the sediment eventually consolidates and lithifies into sedimentary rock (Tucker, 1993; Melim et al., 2002; Boggs, 2009; Azizi et al., 2014; Nader, 2017; Ishaq et al., 2019). Petrographic studies reveal the presence of diagenetic processes like micritization, compaction, cementation, dissolution, neomorphism and internal filling responsible for the lithification and subsequent consolidation of the Umlatdoh Limestone.

Micritization

Micritization involves conversion of certain allochemical grains into dense micrite by the activity of endolithic algae (Longman, 1980; Adabi, 2009; Jafarian et al., 2017, 2018). It takes place in disturbed or shallow water environment at or just below the sediment – water interface where margins of carbonate grains are replaced by micrite (Wei, 1995; Adams and MacKenzie, 1998; Kabanov, 2000). In the present context, development of micritic envelope around skeletal fragments such as Nummulites sp. (Figure 5a), Assilina sp. (Figure 5e), Alveolina sp. (Figure 5b), Discocyclina sp. (Figures 5c and 7h), Biloculina sp. (Figure 5d and 7e) has been attributed to micritization besides modification of internal architectures of a few non-skeletal grains (Figure 5g).

Compaction

The process of sediment volume reduction under the influence of several variables including overburden, subsurface temperature and pressure, burial stress, pore pressure and the chemistry of pore-water, is referred to as compaction. Petrographic studies on Umlatdoh Limestone provide evidences in favour of both mechanical as well as chemical compaction. Modifications in grain contacts from point to long, concavo-convex, and sutured contact has been attributed to mechanical compaction (Figures 5g,f and 8d). In the studied thin sections, Assilina sp. (Figures 5e and 7a) generally display evidences of mechanical compaction due to progressive increase in the overburden pressure during burial.

The later stage of diagenesis resulted from increased compaction caused by overburden and tectonic stresses. Initially, grain-to-grain contacts formed due to the overburden, which gradually evolved into planar and sutured grain contacts. This process led to the development of stylolites (Figures 5f and 7b), also known as dissolution seams or chemical compaction.

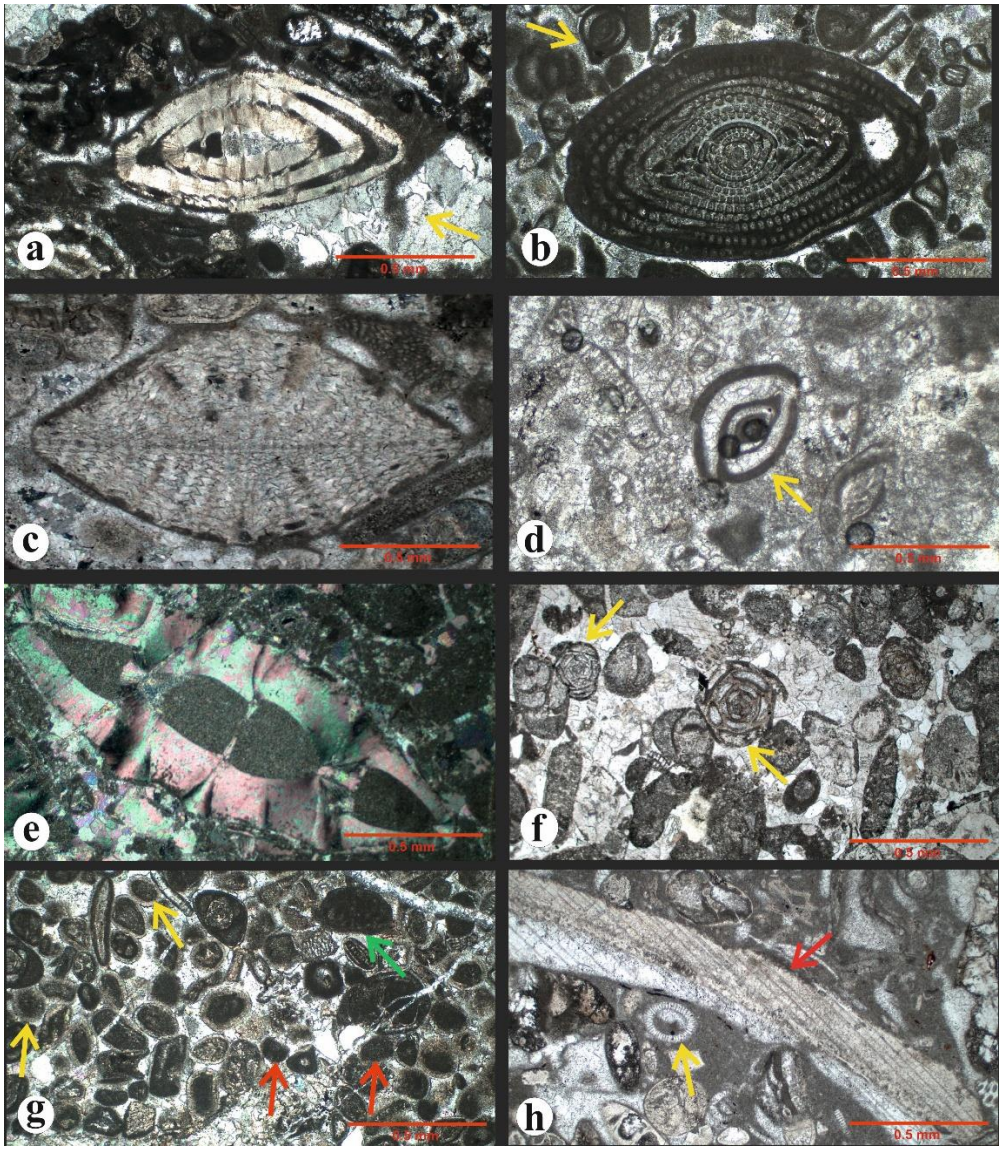

Figure 5. Photomicrographs of Umlatdoh Limestone showing **(a)** Nummulites sp. (PPL), **(b)** Alveolina sp. (PPL), **(c)** Discocyclina sp. (PPL), **(d)** Biloculina sp. (PPL), **(e)** Assilina sp. (XPL), **(f)** Quniqueloculina sp. (sutured grain contacts, yellow arrow, PPL), **(g)** Spherical ooids (yellow arrow) with complete micritization that has destroyed the internal structures of ooids, with outer rim preserved, Intraclast (green arrow), Peloids (red arrow), point and tangential grain contacts and calcite veinlets (PPL), **(h)** Calcite vein (red arrow) and Spherical ooids (yellow arrow, PPL).

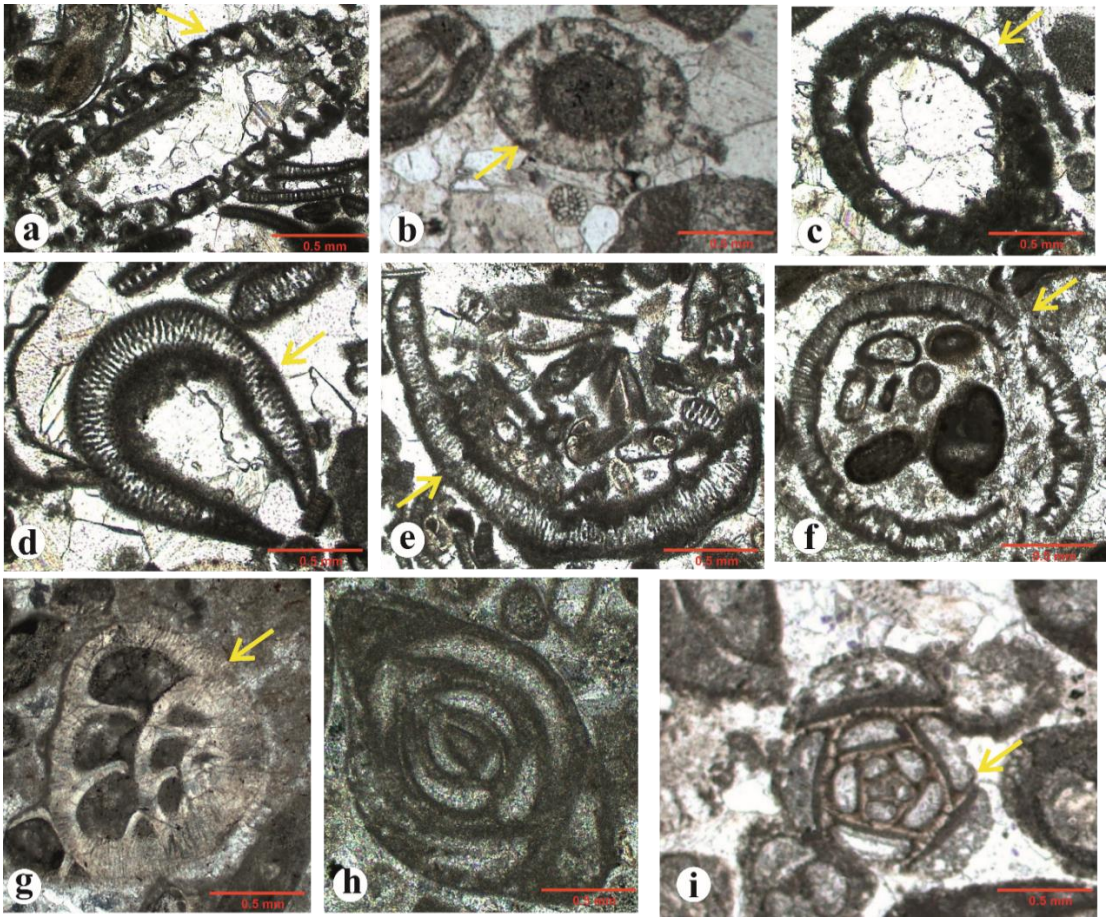

Figure 6. Photomicrographs of Umlatdoh Limestone showing **(a)** – **(f)** Dasycladalean algae with blocky calcite cement which occurs as a pore-filing in the intergranular pore spaces (PPL), **(g)** Lockhartia sp. (PPL), **(h)** Periloculina sp. with well-preserved micrite coating/envelope around the bioclasts indicating micritization (XPL), **(i)** Quniqueloculina sp. with well-preserved micrite coating/envelope around the bioclasts indicating micritization (yellow arrow, PPL).

Cementation

Cementation occurs throughout the entire diagenetic process, where chemical precipitates (in the form of new crystals) form within the pores of sediment, binding the grains together (McIlreath and Morrow, 1990). The mineralogy, shape, and crystal structure of carbonate cements evolve as the diagenetic environment and water chemistry transform from marine phreatic to meteoric phreatic, and then to shallow and deep subsurface waters (Ahr, 2008). The Umlatdoh Limestone contain various types of cements as follows.

Fibrous calcite cement

Fibrous calcite cement appeared as bundles of calcite crystals embedded within a micritic groundmass. It forms along the outer margins of allochem grains, occurring as fine crystalline spars with a thickness of 0.1–0.5 mm (Figure 8d), indicating a shallow marine environment (Flügel, 1982). The presence of fibrous cement is widely recognized as the clearest evidence of synsedimentary cementation (Longman, 1980; Flügel, 2010).

Granular calcite cement

Granular cement, also known as blocky cement, occupied both intergranular and intra-particle pore spaces (Figure 7g). It consists of subhedral to anhedral crystals with crystal size increasing as they grow away from the substrate. The presence of granular calcite cement in both skeletal and non-skeletal grains indicates a low Mg/Ca ratio in the fluids (Purser, 1978). In meteoric water environment, the low Mg^{2+} content promotes the precipitation of calcite in a granular or blocky form, indicate freshwater diagenesis. In the meteoric phreatic zone, where pore spaces are predominantly filled with water, the cementation is more uniform, resulting in larger blocky calcite crystals (Wright and Tucker, 1990; Khalifa, 2005; Zhang et al., 2006; Flügel, 2010; Abu El Ghar et al., 2015). The filling of macropores with coarse crystalline cements is interpreted as evidence of burial cementation (Guo et al., 2016).

Blocky calcite cement

The next generation after fibrous cement is the blocky calcite cement, filled the remaining voids between allochems. It consists of fine- to coarse-grained, subhedral to anhedral crystals ranging from 0.5 to 3 mm in size and also fills internal cavities within bioclasts as intergranular cement (Figure 6c & 7d). In meteoric water environments, low Mg^{2+} content promotes the precipitation of blocky calcite cements (Choquette et al., 1990; Tucker, 2001; Zhang et al., 2006; Flügel, 2010). These cementations occur during both eodiagenesis and mesodiagenesis, filling the voids.

In this study, some instances show dissolution features in the central blocky cement within pores, suggesting deep burial diagenesis (Oldershaw, 1971; Folk, 1974; Bathurst, 1975; Wong and Oldershaw, 1981; Ahmad et al., 2006). In other cases, blocky calcite cement is associated with calcite veins, marking the final phase of cementation and likely formed in a deep phreatic burial environment (Singh, 1987). Carbonate rocks containing this late-stage cement retain some of their primary porosity.

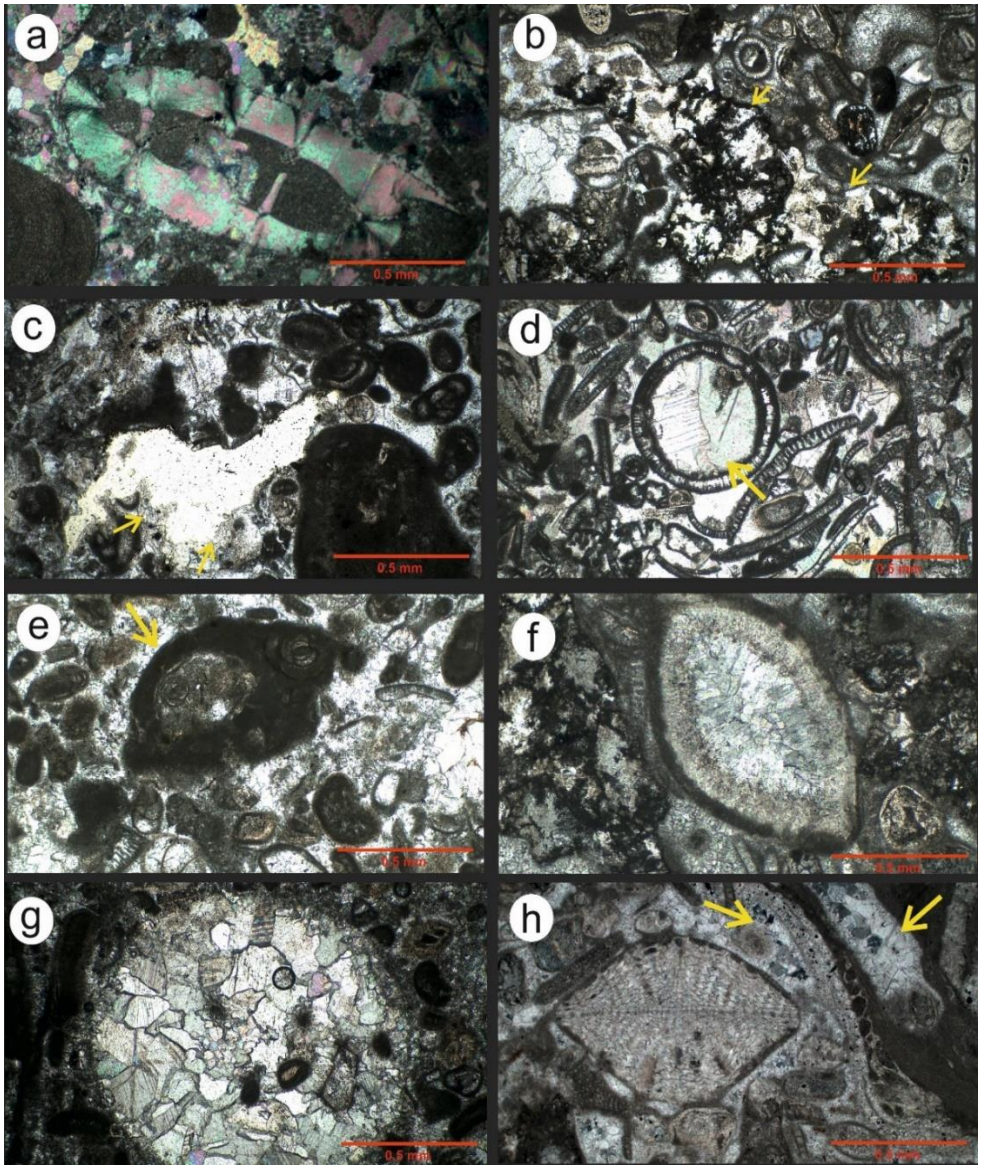

Figure 7. Photomicrographs of Umlatdoh Limestone showing **(a)** Compaction effects on Assilina sp. (XPL), **(b)** Development of stylolite (yellow arrows) due to compaction (PPL), **(c)** Development of stylolite (yellow arrows) due to pressure dissolution (PPL), **(d)** Blocky calcite cement occurs as a pore-filing in the intergranular pore spaces, (XPL), **(e)** Micritization around Biloculina sp. (PPL), **(f)** Growth of drusy calcite cement in Miliolid sp. (XPL), **(g)** Granular calcite cement exhibits fillings of intra-granular pores (XPL), **(h)** Growth of drusy calcite cement (yellow arrows, XPL).

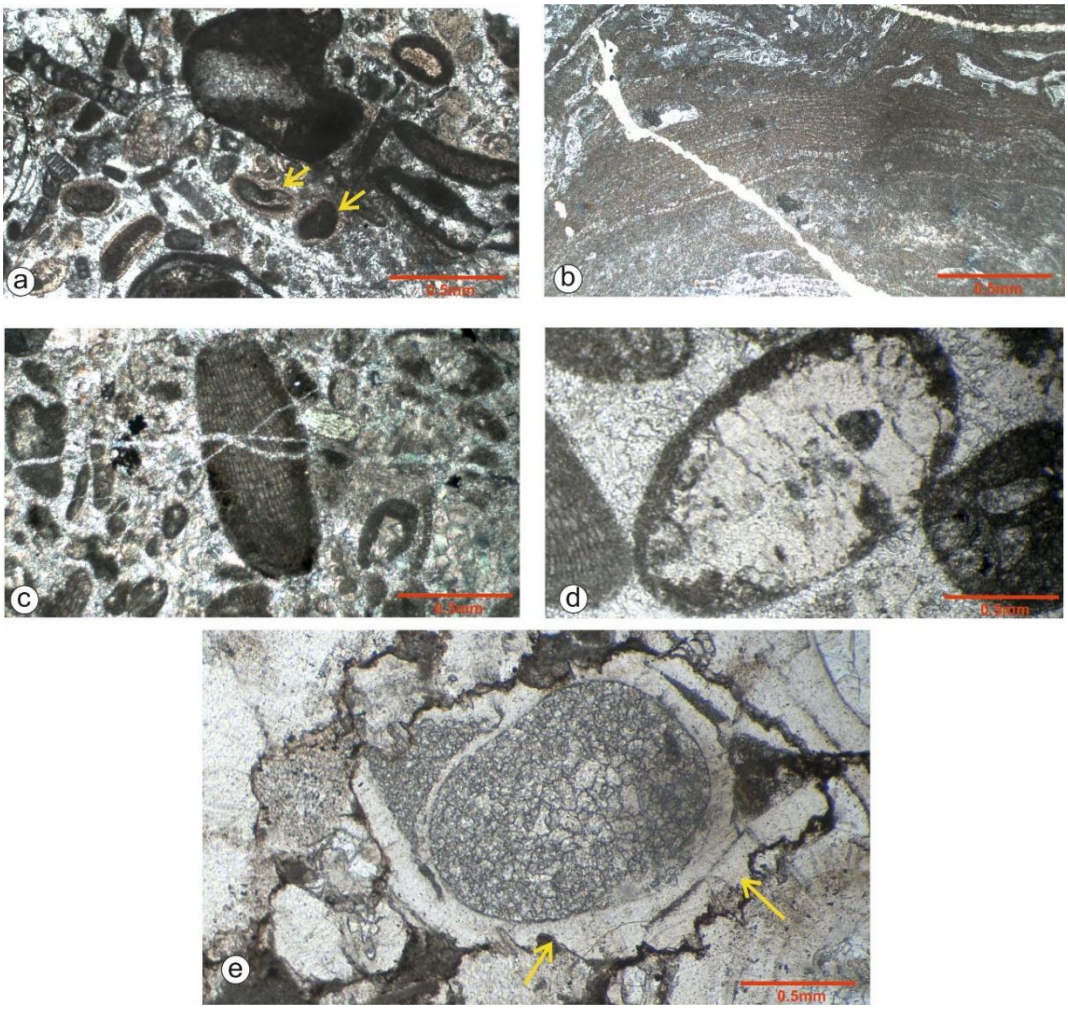

Figure 8. Photomicrographs of Umlatdoh Limestone showing **(a)** fine crystals of rim cements around intraclasts (arrows, PPL), **(b)** cement in fractures (PPL), **(c)** cement in fractures (XPL), **(d)** point contact (PPL), with isopachous fibrous cements around bioclasts, **(e)** Growth of syntaxial calcite cement (yellow arrow).

Neomorphism

Neomorphism encompasses both aggrading and degrading recrystallization, involving transformations within a mineral or its polymorph. The resulting crystals may vary in size or shape from the original ones. In the studied carbonate rock, a specific type of neomorphism, known as calcitization, is observed. This process involves the recrystallization of aragonite shells into sparry calcite, which plays a significant role in carbonate diagenesis (Figures 4a, b). Calcitization is well developed in the micritic matrix, indicating the influence of a meteoric phreatic environment (Choquette and James, 1987; Shaaban, 2004; Kiefer-Ollier et al., 2010; Heidari et al., 2014).

DISCUSSION

Petrographic studies of the Umlatdoh Limestone reveal distinct diagenetic environments as marine, meteoric, and burial realms based on diagenetic features, mineralogical compositions, cement types, and microfabrics. Characteristics of the marine environment include bioturbation, micritization, physical compaction, neomorphism, and isopachous fibrous calcite cement. The meteoric environment is marked by granular and blocky calcite cement, mechanical compaction, and neomorphism. In the burial environment, key processes include blocky calcite cement, mechanical and chemical compaction, fracturing, and the formation of calcite veins.

The petrographic analysis further indicates that the Umlatdoh Limestone underwent two primary diagenetic stages: eodiagenesis and mesodiagenesis, each associated with significant diagenetic events in distinct environments (Figure 9). During the eodiagenesis stage, micritization affected various allochems, including both skeletal (bioclasts, Figure 6h, i) and non-skeletal grains (Figure 5g). This process was

likely driven by microbial activity, including algae and fungi (Llinas, 2002; Vincent et al., 2007; Jadoul and Galli, 2008; Ronchi et al., 2011). Following micritization, marine isopachous rim cement formed around both skeletal and non-skeletal grains.

Marine environment

Marine diagenetic environments are characterized by early micritization and the formation of non-ferron-isopachous fibrous cements (Khalifa, 2005; Taghavi et al., 2006; Vincent et al., 2007; Mahboubi et al., 2010; Abu El Ghar et al., 2015). Micritization is one of the most prominent diagenetic features identified in the Umlatdoh Limestones, suggesting formation in a marine setting. It appears as micritic envelopes and micritized skeletal (bioclasts, Figure 6h, i) and non-skeletal grains (Figure 5g), likely caused by mechanical disintegration or bioerosion of large calcareous organisms, such as Nummulites and algae, by endolithic algae (El Ghar and Hussein, 2005; Khalifa, 2005; Melim et al., 2002). The precipitation of isopachous and pore-filling calcite and calcite overgrowths (Figure 8e) is typically associated with marine and mixed marine-meteoric processes.

Meteoric environment and Mesodiagenesis processes

The presence of granular calcite cement, early-stage blocky calcite cement, micritic cement, dissolution of molds, and neomorphism all indicate meteoric-phreatic diagenetic realms (Melim et al., 2002; Vincent et al., 2007; Abu El Ghar et al., 2015). Similarly, in the mesodiagenesis processes, such as mechanical and chemical compaction, cementation, neomorphism, formation of calcite veins, and fracturing processes impacted the studied limestone (Figures 5h, 8b, c).

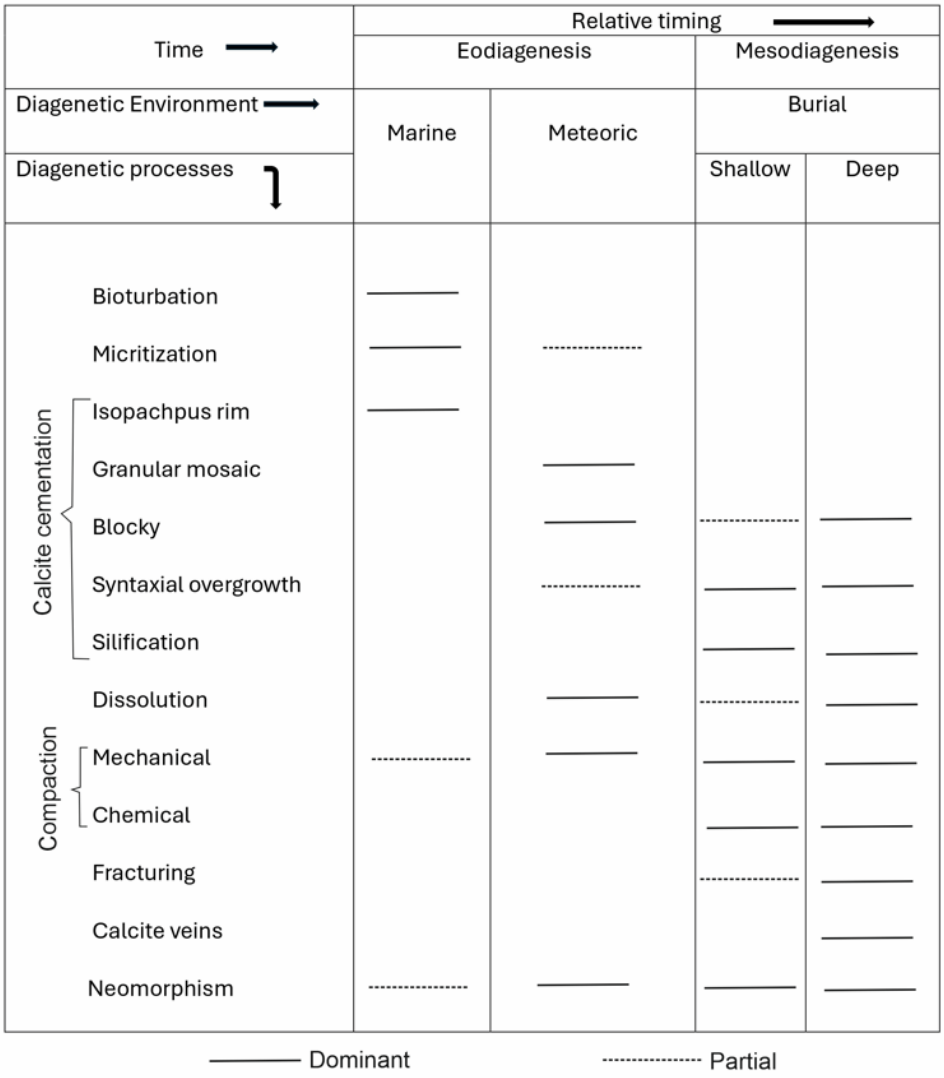

Figure 9. Detailed paragenetic sequence of the Umlatdoh Limestone, representing different diagenetic events observed in thin sections

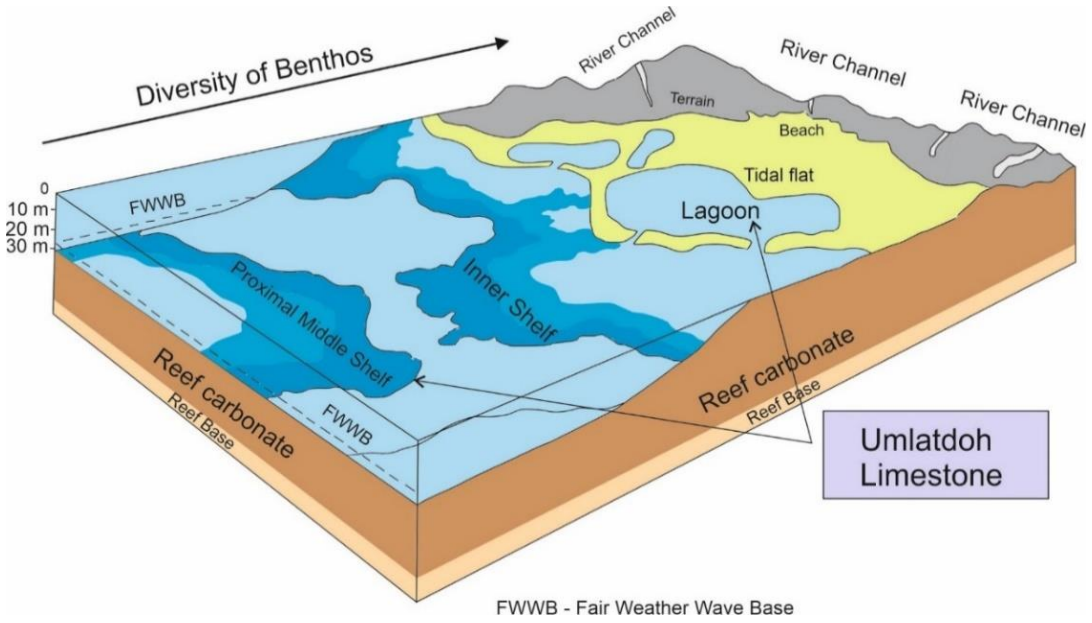

Figure 10. Conceptual depositional model of Umlatdoh Limestone of the study area.

Burial environment

The Umlatdoh Limestone possess features such as sutured and concavo-convex contacts, fractures, veins, and blocky and granular calcite cements. During cementation, calcite crystals formed as overgrowths and blocky textures, suggesting precipitation under burial conditions (Moore, 1989). Burial diagenetic realms are typically divided into shallow and deep burial, though the exact boundary between them is not clearly defined (Vincent et al., 2007; Flügel, 2010). Mechanical compaction features, such as suture and concavo-convex contacts, are indicative of shallow burial condition (Vincent et al., 2007; Mahboubi et al., 2010; Abuseda et al., 2015). Characteristics of chemical compaction such as stylolites and dissolution seams, also appear to develop in shallow burial environments (Mahboubi et al., 2010; Abuseda et al., 2015). In the deep burial realm, fractures, dissolution, and calcite veins, along with blocky calcite cements, are prevalent.

The Umlatdoh Limestone are rich in skeletal grains, including larger benthic foraminifera namely Nummulites sp., Assilina sp., Alveolina sp., Discocyclina sp., Biloculina sp., Quniqueloculina sp., Periloculina sp., Lockhartia sp., and Dasycladalean algae. Abundance of Dasycladalean algae and large benthic foraminifera in the Umlatdoh Limestone clearly indicate that these carbonates are analogous to modern shallow-marine carbonates. Based on biogenic assemblages, the depositional environment of the Umlatdoh Limestone is interpreted as an open lagoonal to proximal middle shelf environment (Figure 10).

CONCLUSIONS

The present study deals with the diagenetic characteristics and depositional environment of Umlatdoh Limestone exposed in southern Shillong Plateau, Meghalaya. The following conclusions are drawn from the present study:

(1) The fine- to medium-grained Umlatdoh Limestone are rich in both skeletal and non-skeletal grains classified as wackestone, packstone and grainstone.

(2) The non-skeletal grains consist of intraclasts, ooids, and peloids, while skeletal grains include foraminifera (Nummulites sp., Assilina sp., Alveolina sp., Discocyclina sp., Biloculina sp., Quniqueloculina sp., Periloculina sp., Lockhartia sp.), Dasycladalean algae and Coraline algae.

(3) The abundance of biogenic assemblages suggests that the depositional environment of the Umlatdoh Limestone was an open lagoonal to proximal middle shelf environment.

(4) The Umlatdoh Limestone underwent various diagenetic processes, including micritization, cementation, compaction, dissolution, and neomorphism.

(5) Based on mineralogical and textural variations in the studied limestones, distinct diagenetic environments were identified, including meteoric-phreatic (freshwater), marine phreatic, mixed marine phreatic, and burial diagenetic settings.

ACKNOWLEDGMENTS

We would like to express our sincere gratitude to Dr. O.P. Pandey for his invaluable contribution in reviewing the manuscript. We acknowledge the Regional Laboratory, ONGC, Sivasagar, Assam, for the necessary help during the preparation of thin sections. The authors also express their gratitude to two anonymous referees who made precise reviews, which helped us in the improvement of the final version of the manuscript.

Author Credit Statement

A Das, M Baruah and M K Pathak carried out fieldwork, analyzed the samples and performed interpretations and writing. D Walia conceptualized the idea, carried out fieldwork and performed writing and editing. S Kumar helped in compilation of research paper.

Data Availability

The data will be shared on request to the corresponding author.

Compliance with Ethical standards

No conflict of interest and adhere to copyright norms

REFERENCES

Abu El Ghar, M. S., Khalifa, M. A. and Hussein, A. W., 2015. Carbonate diagenesis of the mixed clastic–carbonate Galala formation, north eastern Desert, Egypt. Arabian J. Geosci., 8, 2551-2565.

Abuseda, H., Kassab, M. A., LaLa, A. M. and El Sayed, N. A., 2015. Integrated petrographical and petrophysical studies of some Eocene carbonate rocks, Southwest Sinai, Egypt. Egyptian J. Petr., 24(2), 213-230.

Acharyya, S.K., Mitra, N.D. and Nandy, D.R., 1986. Regional geology and tectonic setting of northeast India and adjoining region. Mem. Geol. Survey India, 119, 6-12.

Adabi, M.H., 2009. Multistage Dolomitization of Upper Jurassic Mozduran Formation, Kopet-Dagh Basin, N.E. Iran. Carbonates and Evaporites, 24(1),16-32.

Adams, A.E and Mackenzie, W.S., 1998. A Colour Atlas of Carbonate Sediments and Rocks Under the Microscope. 180.

Ahmad, A. H. M., Bhat, G. M. and Khan, M. H. A., 2006. Depositional environments and diagenesis of the kuldhar and Keera Dome carbonates (Late Bathonian–Early Callovian) of Western India. J. Asian Earth Sci., 27(6), 765-778.

Ahr, W.M., 2008. A new genetic classification of carbonate porosity and its application to reservoir characterization. In Am. Assoc. Petr. Geol. Annual convention (Abstract), San Antonio, Apr. 20-23.

Azizi, S.H.H., Shabestari, G.M. and Khazaei, A., 2014. Petrography and geochemistry of Paleocene–Eocene limestones in the Ching-dar syncline, eastern Iran. Geosci. Frontiers, 5(3), 429-438.

Bathurst, R. G. C., 1975. Carbonate sediments and their diagenesis (Developments in Sedimentology 12), Amsterdam, the Netherlands: Elsevier, 658.

Beavington-Penney, S. J. and Racey, A., 2004. Ecology of extant nummulitids and other larger benthic foraminifera: applications in palaeoenvironmental analysis. Earth-Sci. Rev., 67(3-4), 219-265.

Biswas, S., Coutand, I., Grujic, D., Hager, C., Stöckli, D. and Grasemann, B., 2007. Exhumation and uplift of the Shillong plateau and its influence on the eastern Himalayas: New constraints from apatite and zircon (U-Th-[Sm])/He and apatite fission track analyses. Tectonics, 26(6).

Boggs, Jr. S., 2009: Petrology of Sedimentary Rocks. 2nd Ed., Cambridge University Press, New York, 600.

Boothroyd, J.C., 1985. Tidal inlets and tidal deltas. In Coastal sedimentary environments. Springer, New York, 445-532.

Choquette, P. W. and James, N. P., 1987. Diagenesis# 12. Diagenesis in Limestones-3. The deep burial environment. Geosci. Can., 14(1), 3-35.

Choquette, P. W., James, N., McIlreath, I. and Morrow, D., 1990. Diagenesis. Geosci. Can., 10(4).

Desikachar, S.V., 1974. A review of the tectonic and geological history of eastern India in terms of 'plate tectonics' theory. J. Geol. Soc. India, 15, 137-149.

Dunham, R. J., 1962. Classification of carbonate rocks according to depositional textures, In: Classification of Carbonate Rocks — A Symposium . , ed. by Ham , William E.. AAPG Memoir, 1 . AAPG (American Association of Petroleum Geologists), Tulsa, Oklahoma, pp. 108-121

El Ghar, M. A. and Hussein, A. W., 2005. Post-depositional changes of the lower-middle Eocene limestones of the area between Assiut and Minia, West of the Nile Valley, Egypt. In Proc. first int. conf. on the geology of the Tethys, 224-248.

Evans, P., 1964. Tectonic framework of Assam. J. Geol. Soc. India, 5, 80-96.

Flügel, E., 1982. Introduction to facies analysis. Microfacies Analysis of Limestones, 1-26.

Flügel, E., 2010. Microfacies of carbonate rocks: Analysis, Interpretation and Application. Berlin Heidelberg: Springer-Verlag, 984.

Folk, R. L., 1974. The natural history of crystalline calcium carbonate; effect of magnesium content and salinity. J. Sediment. Res., 44(1), 40-53.

Garg, R. and Jain, K.P., 1995. Significance of the terminal Cretaceous calcareous nannofossil marker Micula prinsii at the Cretaceous–Tertiary boundary in the Um Sohryngkew section, Meghalaya, India. Curr. Sci., 69(12), 1012-1017.

Ghosh, A.K. and Sarkar, S., 2013. Palaeoecological implications of corallinacean red algae and halimedacean green algae from the Prang Formation of South Shillong Plateau, Meghalaya. J. Geol. Soc. India, 81, 531-542.

Gischler, E., Hauser, I., Heinrich, K. and Scheitel, U., 2003. Characterization of depositional environments in isolated carbonate platforms based on benthic foraminifera, Belize, Central America. Palaios, 18(3), 236-255.

Guo, C., Chen, D., Qing, H., Dong, S., Li, G., Wang, D. and Liu, C., 2016. Multiple dolomitization and later hydrothermal alteration on the Upper Cambrian-Lower Ordovician carbonates in the northern Tarim Basin, China. Mar. Pet. Geol., 72, 295–316.

Gupta, R.P. and Sen, A.K., 1988. Imprints of the ninety-east ridge in the Shillong Plateau, Indian Shield. Tectonophysics, 154(3-4), 335-341.

Hallock, P. and Glenn, E.C., 1986. Larger foraminifera: a tool for paleoenvironmental analysis of Cenozoic carbonate depositional facies. Palaios, 1, 55-64.

Heidari, A., Gonzalez, L. A., Mahboubi, A., Moussavi-Harami, R., Ludvigson, G. A. and Chakrapani, G. J., 2014. Diagenetic model of carbonate rocks of Guri Member of Mishan Formation (lower to middle Miocene) SE Zagros Basin, Iran. J. Geol. Soc. India, 84, 87-104.

Ishaq, M., Jan, I.U., Hanif, M. and Awais, M., 2019. Microfacies and diagenetic studies of the early Eocene Sakesar Limestone, Potwar Plateau, Pakistan: approach of reservoir evaluation using outcrop analogue. Carbonates Evaporites, 34(3), 623-656.

Jadoul, F. and Galli, M. T., 2008. The Hettangian shallow water carbonates after the Triassic/Jurassic biocalcification crisis: the Albenza Formation in the Western Southern Alps. Riv. Ital. Paleontol. Stratigr., 114(3), 453-470.

Jafarian, A., Fallah-Bagtash, R., Mattern F. and Heubeck C., 2017. Reservoir quality along a homoclinal carbonate ramp deposit: The Permian Upper Dalan Formation, South Pars Field, Persian Gulf Basin. Mar. Petrol. Geol., 88, 587–604.

Jafarian, A., Javanbakht, M., Koeshidayatullah, A., Pimentel, N., Salad Hersi, O., Yahyaei, A. and Beigi, M., 2018. Paleoenvironmental, diagenetic, and eustatic controls on the Permo–Triassic carbonate-evaporite reservoir quality, Upper Dalan and Kangan formations, Lavan Gas Field, Zagros Basin. Geol. J., 53(4), 1442–1457.

Jauhri, A.K., 1994. Carbonate buildup in the Lakadong Formation of the South Shillong Plateau, NE India: A micropaleontological perspective. Boll. Soc. Paleontol. Ital, 33, 157-170.

Jauhri, A.K., 1998. Miscellanea Pfender, 1935 (foraminiferida) from the south shillong region, NE India. J. Palaeontol. Soc. Ind, 43, 73-83.

Jauhri, A.K. and Agarwal, K.K., 2001. Early Palaeogene in the south Shillong Plateau, NE India: local biostratigraphic signals of global tectonic and oceanic changes. Palaeogeogr. Palaeoclimatol. Palaeoecol., 168(1-2), 187-203.

Jauhri, A. K., Kishore, S., Singh, A. P., Singh, S. K., Misra, P. K. and Tiwari, R. P., 2016. Coralline algal and larger foraminiferal facies in the Prang Formation (Middle-Upper Eocene), Jaintia Hills, Meghalaya, NE India. J. Palaeontol. Soc. Ind., 61(1), 99-109.

Jones, B. and Hunter, I.G., 1992. Very large boulders on the coast of Grand Cayman: the effects of giant waves on rocky coastlines. J. Coast. Res., 8(4), 763-774.

Kabanov, P.B., 2000. Grain micritization as facial indicator in shallow water marine carbonate rocks. Byull. Moskovsk. Obshch. Isp. Prir., Otd. Biol., 75(4), 39-48.

Kalita, K.D. and Gogoi, H., 2015. Microfacies types (MFT) and palaeoenvironment of the Umlatodoh carbonates in the Shillong Plateau of Meghalaya, NE India. J. Geol. Soc. India, 85(6), 686-696.

Khalifa, M. A., 2005. Lithofacies, diagenesis and cyclicity of the 'lowermember' of the Khuff Formation (Late Permian), Al Qasim Province, Saudi Arabia. J. Asian Earth Sci., 25(5), 719–734.

Kiefer-Ollier, E., Loisy, C. and Cerepi, A., 2010. Diagenetic signature of the Mid-Paleocene exposure surface in the southeastern Pyrenean platform. C. R. Geosci**.**, 342(6), 483-491.

Li, C., Jones, B. and Blanchon, P., 1997. Lagoon-shelf sediment exchange by storms--evidence from foraminiferal assemblages, east coast of Grand Cayman, British West Indies. J. Sediment. Res., 67(1), 17-25.

Li, C., Jones, B. and Kalbfleisch, W.B., 1998. Carbonate sediment transport pathways based on foraminifera: case study from Frank Sound, Grand Cayman, British West Indies. Sedimentology, 45(1), 109-120.

Llinas, J.C., 2002. Diagenetic history of the Upper Jurassic Smackover Formation and its Effects on Reservoir Properties: Vocation Field, Manila Sub-Basin, Eastern Gulf Coastal Plain. Trans. Gulf Coast Assoc. Geol. Soc. (GCAGS), 52, 631–644.

Longman, M.W., 1980. Carbonate diagenetic textures from near surface diagenetic environments. AAPG bull., 64(4), 461-487.

Mahboubi, A., Moussavi-Harami, R., Carpenter, S. J., Aghaei, A. and Collins, L. B., 2010. Petrographical and geochemical evidences for paragenetic sequence interpretation of diagenesis in mixed siliciclastic–carbonate sediments: Mozduran Formation (Upper Jurassic), south of Agh-Darband, NE Iran. Carbonates and Evaporites, 25, 231-246.

Mcllreath, I. A. and Morrow, D. W., 1990. Diagenesis. Reprint Series 4. Geosci. Canada. Geological Association of Canada, 338.

Mehrotra, K.K. and Banerji, R.K., 1973. Middle-Upper Eocene Biostratigraphy of Khasi and Jaintia Hills based on planktonic and larger foraminifera. J. Palaeontol. Soc. India, 18, 22-26.

Melim, L.A., Westphal, H., Swart, P.K., Eberli, G.P. and Munnecke, A., 2002. Questioning carbonate diagenetic paradigms: evidence from the Neogene of the Bahamas. Mar. Geol., 185(1-2), 27-53.

Moore, C.H., 1989. Carbonate diagenesis and porosity. Elsevier, 317.

Nader, F.H., 2017. Introduction. In: Multi-scale quantitative diagenesis and impacts on heterogeneity of Carbonate Reservoir Rocks. Springer, New York, 1–13.

Nagappa, Y., 1959. Foraminiferal biostratigraphy of the Cretaceous-Eocene succession in the India-Pakistan-Burma region. Micropaleontology, 5(2), 145-177.

Najman, Y., Bracciali, L., Parrish, R.R., Chisty, E. and Copley, A., 2016. Evolving strain partitioning in the Eastern Himalaya: The growth of the Shillong Plateau. Earth Planet. Sci. Lett., 433, 1-9.

Nandy, D.R., 1986. Tectonics, seismicity and gravity of northeastern India and adjoining region. Mem. Geol. Surv. India, 119, 13-17.

Nandy, D.R., 2017. Geodynamics of Northeastern India and the adjoining region. Scientific Book Centre.

Oldershaw, A. E., 1971. The significance of ferroan and nonferroan calcite cements in the Halkin and Wenlock limestones (Great Britain). Carbonate Cements: Johns Hopkins Univ. Studies in Geol, 19, 225-232.

Purser, B. H., 1978. Early diagenesis and the preservation of porosity in Jurassic limestones. J. Pet. Geol., 1(2), 83-94.

Ray, J., Saha, A., Ganguly, S., Balaram, V., Krishna, A.K. and Hazra, S., 2011. Geochemistry and petrogenesis of Neoproterozoic Mylliem granitoids, Meghalaya Plateau, northeastern India. J. Earth Syst. Sci., 120(3), 459-473.

Ronchi, P., Jadoul, F., Ceriani, A., Di Giulio, A., Scotti, P., Ortenzi, A. and Previde Massara, E., 2011. Multistage dolomitization and distribution of dolomitized bodies in Early Jurassic carbonate platforms (Southern Alps, Italy). Sedimentology, 58(2), 532-565.

Sahoo, S., Gogoi, B. and Mahanta, B. N., 2024. Petrology, mineral chemistry and geochemistry of lamprophyres from Rongjeng–Nongchram area, East Garo Hills, Shillong Plateau, Meghalaya, Northeast India. J. Earth Syst. Sci., 133(1), 16.

Saraswati, P. K., Khanolkar, S. and Banerjee, S., 2018. Paleogene stratigraphy of Kutch, India: an update about progress in foraminiferal biostratigraphy. Geodinamina Acta, 30(1), 100-118.

Sarkar, S., 2015a. Thanetian-Ilerdian coralline algae-benthic foraminifera from north-east India: microfacies analysis and new insights into the Tethyan perspective. Lethaia, 48, 13- 28.

Sarkar, S., 2015b. Calcareous algal-rich carbonate sediments from Assam Shelf, N-E India: An overview of the palaeoenvironmental implications. In: S. Mukherjee (Ed.), Pet. Geosci. Indian Contexts. Springer Geology, Switzerland, 175-189.

Sarkar, S., 2016. Early Eocene calcareous algae and benthic foraminifera from Meghalaya, NE India: A new record of microfacies and palaeoenvironment. J. Geol. Soc. India, 88(3), 281-294.

Sarkar, S., 2020. Ecostratigraphic implications of a Late Palaeocene shallow-marine benthic community from the Jaintia Hills, Meghalaya, NE India. J. Earth Syst. Sci., 129(1), 10.

Scoffin, T.P., 1993. The geological effects of hurricanes on coral reefs and the interpretation of storm deposits. Coral Reefs, 12(3), 203-221.

Shaaban, M. N., 2004. Diagenesis of the lower Eocene Thebes Formation, Gebel Rewagen area, Eastern Desert, Egypt. Sediment. Geol., 165(1-2), 53-65.

Shaghude, Y.W., Wannas, K.O. and Mahongo, S.B., 2002. Biogenic assemblage and hydrodynamic settings of the tidally dominated reef platform sediments of the Zanzibar Channel. West Indian Ocean J. Mar. Sci., 1(2), 107-116.

Singh, U., 1987. Ooids and cements from the Late Precambrian of the Flinders Ranges, South Australia. J. Sediment. Res., 57(1), 117–127.

Srivastava, V.K. and Singh, B.P., 2019. Depositional environments and sources for the middle Eocene Fulra Limestone Formation, Kachchh Basin, western India: Evidences from facies analysis, mineralogy, and geochemistry. Geol. J., 54(1), 62-82.

Taghavi, A. A., Mørk, A. and Emadi, M. A., 2006. Sequence stratigraphically controlled diagenesis governs reservoir quality in the carbonate Dehluran Field, southwest Iran. Pet. Geosci., 12(2), 115-126.

Tewari, V.C., Kumar, K., Lokho, K. and Siddaiah, N.S., 2010a. Lakadong limestone: Paleocene-Eocene boundary carbonates sedimentation in Meghalaya, northeastern India. Curr. Sci., 98, 88-95.

Tewari, V.C., Lokho, K., Kumar, K. and Siddaiah, N.S., 2010b. Late Cretaceous-Paleogene Basin Architecture and Evolution of the Shillong Shelf Sedimentation, Meghalaya, Northeast India. Jour. Indian Geol. Cong., 2, 61-73.

Tucker, M.E., 1993. Carbonate diagenesis and sequence stratigraphy. Sedimentology Review, 1, 51-72.

Tucker, M.E., 2001. Sedimentary Petrology: An Introduction to the Origin of Sedimentary Rocks. Blackwell Science, Oxford, p. 260.

Vincent, B., Emmanuel, L., Houel, P. and Loreau, J.P., 2007. Geodynamic control on carbonate diagenesis: petrographic and isotopic investigation of the Upper Jurassic formations of the Paris Basin (France). Sediment. Geol., 197(3-4), 267-289.

Wei, L.M., 1995. Study on the micritization of carbonate grains by bacteria and algae. Acta Sedimentol. Sin., 13(3), 89-97.

Wilson, B., Jones, B. and Birjue, K., 2010. Paleoenvironmental interpretations based on foraminiferal abundance biozones, Mayo Limestone, Trinidad, West Indies, including alpha and beta diversities. Palaios, 25(3), 158-166.

Wong, P. K. and Oldershaw, A., 1981. Burial cementation in the Devonian, Kaybob reef complex, Alberta, Canada. J. Sediment. Res., 51(2), 507-520.

Wright, V. P. and Tucker, M., 1990. Carbonate sediments and limestones: constituents. Carbonate Sedimentology. Blackwell, Oxford, 1-27.

Zhang, H., Ding, L., Wang, X., Wang, L., Wang, Q. and Xia, G., 2006. Carbonate diagenesis controlled by glacioeustatic sea-level changes: a case study from the Carboniferous-Permian Boundary Section at Xikou, China. J. China Univ. Geosci., 17(2), 103-114.

Received on: 08-02-2024 ; Revised on: 15-11-2024 ; Accepted on:18-11-2024

J. Ind. Geophys. Union, 29(1) (2025), 26-37
https://doi.org/10.71122/JIGU.29(1)2025.003

Reservoir characterization using a hybrid of particle swarm optimization: A case study from the Blackfoot field, Canada

Ravi Kant[1*], S.P. Maurya[1], Nitin Verma[1], Raghav Singh[1], K.H. Singh[2], Ajay P. Singh[1], Prabodh K. Kushwaha[1], M.K. Srivastava[1], G. Hema[1], Harsha Raghuvanshi[1] and Richa[1]

[1]Department of Geophysics, Institute of Science, Banaras Hindu University, Varanasi-221005, India
[2]Department of Earth Sciences, Indian Institute of Technology, Bombay, Mumbai-400076, India
[*]Corresponding author: ravigeo@bhu.ac.in

ABSTRACT

The development, management, and optimization of a reservoir depend on precise reservoir characterization. There are several methods for doing this, however in the current work, seismic inversion based on the hybrid particle swarm optimization (HPSO) methodology is used. In this method, a local optimization method called quasi-newton method (QNM), combined with a global optimization method called PSO to maximize their benefits and minimize their downsides are used. The global optimization method takes a lot of time to converge whereas, Quasi-Newton method is rapid, but heavily dependent on the initial model. The present study takes these two limitations into account. To characterize the reservoir, the hybrid PSO uses post-stack seismic data to predict acoustic impedance and porosity in the inter-well zone. The effectiveness of this newly devised method is first evaluated using synthetic data, and then it is applied to the real data from the Blackfoot area in Canada. The findings show that for both the synthetic and real data, the inverted outcomes closely match the observed data. The analysis anticipated that the inter-well acoustic impedance and porosity volume would vary from 6000 to 12000 m/s*g/cc and 5-22%, respectively. These volumes display extremely detailed subsurface data. The analysis of inverted findings reveals an abnormal zone inside the two-way transit time frame of 1045 to 1065 ms, ranging from low-impedance 6500-9000m/s*g/cc, and high porosity >15%. This unconventional area is classified as a reservoir. The method is particularly useful in nearby regions where detailed subsurface information needs to be estimated, even with limited prior data.

Keywords: Seismic inversion, Hybrid optimization, Particle swarm optimization, Quasi-newton method, Reservoir characterization, Blackfoot field (Canada)

INTRODUCTION

Reservoir characterization is a multidisciplinary process in the field of geosciences encompassing geology, geophysics and petroleum engineering. It involves the detailed analysis and description of subsurface reservoirs to understand their properties and behaviour. The primary goal of reservoir characterization is to obtain a comprehensive understanding of the reservoir's geological, petrophysical, and fluid properties (Maurya et al., 2020; Kumar et., 2024; Singh et al., 2024). This information is crucial for optimizing oil and gas recovery strategies and making informed decisions throughout the life cycle of a reservoir. Reservoir characterization based on seismic inversion is a crucial process, a technique used to extract detailed information about the subsurface properties of a reservoir by analyzing seismic data that includes properties such as rock and fluid types, porosity, permeability and acoustic impedance. Several techniques are available, but seismic inversion is used here to characterize the reservoir. This method has become quite popular and requires less prior information for implementation (Maurya and Singh, 2018; Kant et al., 2024a).

Various techniques for seismic inversion are continually evolving (Russell et al., 2003; Kant et al., 2024b), which are broadly classified into two categories: direct inversion and indirect inversion. In direct inversion methods, the acquired data is directly used to derive subsurface information. Conversely, indirect inversion methods involve creating a subsurface model and generating synthetic data, adjusting the model to minimize the difference between synthetic and recorded data. This indirect approach is advantageous as it is less affected by inaccuracies or noise in the data, leading to more robust results (Maurya and Sarkar, 2016; Hema et al., 2024). To adjust the subsurface model in seismic inversion, various optimization methods are typically employed. Optimization seeks to determine input values for an objective function that maximize or minimize its output, essentially minimizing the discrepancy between the model and the real Earth data. These techniques are categorized into local and global optimization methods. In local optimization, algorithms follow the downward slope of the cost function's topology, using gradient information to adjust the model and converge to the nearest minimum, based on the starting model's position. However, local methods may get trapped in a local minimum unless the initial guess is close to the global minimum, especially when dealing with multimodal cost functions. On the other hand, global optimization algorithms aim to converge to the global minimum, even in the presence of complex, multimodal cost functions. Examples of global optimization methods include the Monte Carlo method, genetic algorithms, particle swarm optimization (PSO), simulated annealing, while local optimization methods include, steepest descent, conjugate-gradient, Newton's method and Quasi-Newton methods.

The primary objective of any optimization technique is to determine the optimal solution to a problem, which often

involves multiple factors. The distinction between local and global optimization reflects the different search strategies employed by these algorithms. The initial choice of the model significantly impacts the effectiveness of optimization methods such as matrix inversion, gradient descent, or the conjugate gradient method (Maurya et al., 2023). For handling erratic multimodal functions, PSO and the quasi-Newton method are effective strategies. Quasi-Newton methods, which extend Newton's approach by using updated approximations of the Hessian matrix, allow for faster convergence without the need to compute the entire Hessian matrix (Shanno, 1970). In seismic inversion, the primary objective is to determine subsurface acoustic impedance and porosity, which are key geophysical parameters that reveal rock and fluid types beneath the Earth's surface.

Seismic reservoir characterization is essential in integrated exploration and reservoir studies, providing a comprehensive understanding of reservoir structures and properties (Bosch et al., 2010; Bonnans et al., 2006; Kushwaha et al., 2023). In modern prospect evaluation, in reservoir characterization and geological modelling, geophysical techniques have become critically important. Identifying deeper reservoirs has historically posed challenges in exploration, with traditional reservoir characterization methods often increasing both costs as well as risks. Integrated seismic inversion and reservoir characterization have emerged as vital tools to address these challenges, offering critical insights that enhance exploration and production processes, particularly in complex and deep reservoirs (Broyden, 1970; Du and Macgregor, 2010). The main objectives of this study are to evaluate the efficiency of hybrid optimization-based seismic inversion, leveraging seismic data, and to identify potentially productive zones within the Blackfoot field of Alberta, Canada (Simin at al., 1996; Dufour et al., 2002). This analysis is especially relevant for offshore projects, where identifying promising zones can be difficult due to the lack of well-log data. The analytical procedures are conducted using MATLAB and the findings are presented through a comparative analysis of the outcomes obtained from the hybrid optimization approach.

HYBRID PARTICLE SWARM OPTIMIZATIONS (HPSO)

A hybrid algorithm combines two or more distinct approaches to address the same problem, commonly implemented in programming languages such as C++ or Matlab. Depending on the data, the algorithm may dynamically choose between these approaches. This integration is typically performed to amalgamate desirable features from each approach, resulting in an algorithm that surpasses the individual strengths of its components (Nocedal and Wright, 1999). Unlike the simple combination of various algorithms targeting different problems, a hybrid algorithm specifically involves blending approaches designed to solve the same problem but with differences, particularly in performance. Many algorithms can be viewed as compositions of smaller components, and hybrid optimization stands out for its success in maximizing the advantages of diverse techniques while minimizing their respective drawbacks, ultimately leading to enhanced results (Maurya and Singh, 2020). In the context of optimization, a hybrid function persists with the optimization process after the initial solver concludes. In this scenario, a hybrid function incorporates elements of both the quasi-newton's method and the particle swarm optimization solver. By refining the relatively coarse solution provided by the first solver, a hybrid function can converge to a more precise and accurate solution. The flow chart of hybrid particle swarm optimization shown in Figure 1.

In this study, we conducted the inversion of post-stack seismic reflection data to derive subsurface acoustic impedance and porosity, utilizing the global optimization technique known as particle swarm optimization along with quasi-newton method. While global optimization is not influenced by the starting model, its drawback lies in the prolonged time it takes to reach the optimal solution, thereby extending the timeline and increasing the costs of exploration projects. On the other hand, the convergent time of local optimization, specifically quasi-newton method, is very less but needs good starting model. If the starting model is distant from the globally optimal solution, the process can become trapped in local minima, yielding unsatisfactory results. The present work aims to address these challenges by proposing a method that combines particle swarm optimization with quasi-newton method. The objective is to allow particle swarm optimization in a specific time frame to obtain results close to the ideal solution. As achieving the exact optimal solution may take an indefinite amount of time, expecting it within the allocated time frame is impractical. Once a reasonable proximity to the ideal solution is reached, local optimization techniques can be applied, using the particle swarm optimization results as a baseline model. This approach reduces the reliance on local optimization on the initial model, facilitating a rapid convergence to the optimal outcome. Given the simplicity and minimal specialized knowledge required for particle swarm optimization and quasi-newton method, they are recommended for global and local optimization, respectively. In this study, the integration of global and local optimization was achieved through the execution of the following steps.

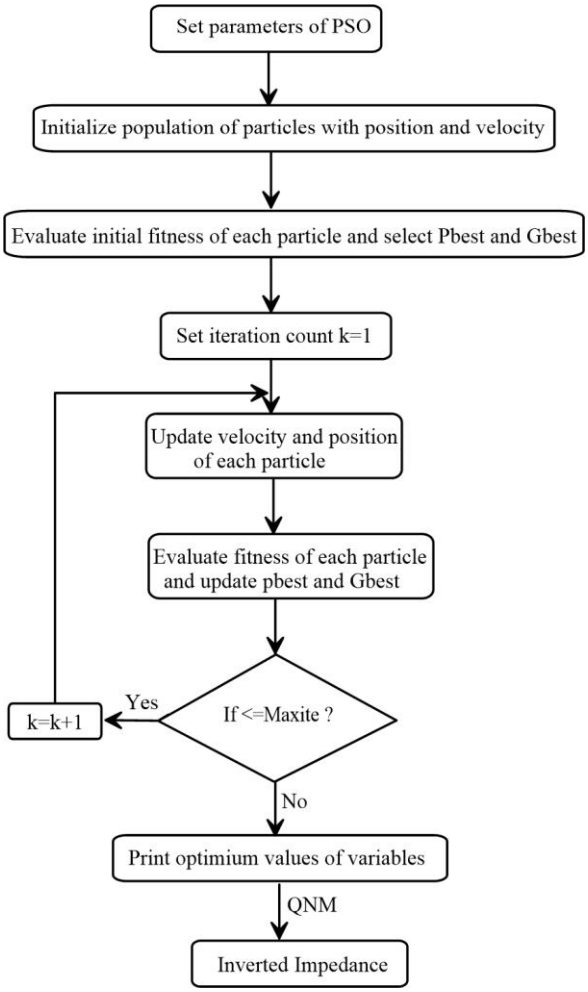

Figure 1. The flowchart representing the workflow of the developed methodology to combine the particle swam optimization and quasi-newton method**.**

1. Select desired seismic and well-log data as input.
2. Transforming depth into time is undertaken to enable the utilization of seismic data in the time domain alongside well-log data in the depth domain.
3. The initial population, comprising acoustic impedances and porosity is generated using a chosen PSO operator implemented for this purpose.
4. Utilizing the given formula, reflectivity is calculated from impedance as follows.

$$R_{modeled(i)} = \frac{Z_{modeled}(i+1) - Z_{modeled}(i)}{\left(Z_{modeled}(i+1) + Z_{modeled}(i)\right)} \quad (1)$$

5. Compute synthetic trace using the formula below.

$$Synthetic\ trace\ (t) = w * r = \int_0^{\infty} r(n)w(n-t)dn \quad (2)$$

where t is time and n is the data index number. When using sampled data, the linear discrete convolution's integral transforms into a sum and can be written as,

$$Synthetic\ trace\ (t) = w * r = \sum_{n=0}^{n=N} r(n)w(n-t) \quad (3)$$

6. Use the formula below to determine the RMS error (fitness function) between the synthetic data and the input seismic data.

$$\text{RMS Error (E)} = \frac{1}{n}\sqrt{\sum_{j=1}^{n}(S_{obs}^{i} - S_{mod}^{i})^2} + \frac{1}{n}\sqrt{\sum_{j=1}^{n}(Z_{obs}^{i} - Z_{mod}^{i})^2} \quad (4)$$

Where n is the total number of sample points, S^{i}_{obs} is input seismic data at the i^{th} sample, S^{i}_{mod} is the synthetic trace at the i^{th} sample. The other part of the equation is used here to constraints solution and this information comes from the prior study i.e. well-log in our case. Z^{i}_{obs} is the impedance at i^{th} sample estimated directly from well log data and Z^{i}_{mod} is the impedance at i^{th} sample generated by the genetic algorithm in its population.

7. Modify the initial population to reduce RMS error as much as possible within a limited time interval by repeating steps 3 to 6. The output of this step will be acoustic impedance (say, AI_0) that satisfies equation 4.
8. Use a QNM by choosing the initial model (AI_0) as the output of the Particle Swarm Optimization.
9. Compute the Hessian matrix with the value of gradient, model, and objective function.
10. Calculate the RMS error using equation 4.
11. Identify the best solution based on the RMS error and modify the new solution based on the best solution.
12. Check whether the new solution is better than the existing best solution or not.
13. Repeat steps 9 to 12 to terminate the program, and get desired acoustic impedance.

After the mathematical formulation of the hybrid approach, which integrates particle swarm optimization with the quasi-Newton method, the methodology was assessed using synthetic data.

RESULTS AND DISCUSSION

Synthetic example to test algorithm

To test the developed hybrid particle swarm optimization, a synthetic data inversion was conducted. Since the synthetic model has known impedance, it allows for comparison with the inverted impedance, enabling us to monitor the algorithm's effectiveness. The synthetic data is generated using a convolution model, where a seismic wavelet is convolved with the Earth's reflectivity. In convolution modeling, it is assumed that plane waves travel across horizontally homogeneous layers' boundaries, disregarding the impacts of geometric divergence, elastic absorption, wavelet dispersion, transmission losses, mode conversions, and multiple reflections. To retrieve the plane-wave amplitudes of primary P-wave reflections, the seismic data needs to undergo processing to eliminate these effects.

Equations 1, 2, and 3 are employed to generate a synthetic seismogram, utilizing a seventeen-layer model and a Ricker wavelet. The Ricker wavelet is selected due to its effectiveness in representing seismic sources with a zero-phase wavelet, which is commonly used in seismic modeling. The Ricker wavelet employed in this study has a central frequency of 45 Hz, which is chosen to match the dominant frequency typically observed in the target geological formations. The wavelet's amplitude spectrum is characterized by its peak at the central frequency, with symmetrical decay on either side, ensuring that it effectively captures the seismic response of the modeled subsurface layers. The time duration of the wavelet was selected to provide adequate resolution while maintaining the wavelet's compact nature, ensuring minimal side lobes and reducing interference between reflections from different layers. By using this specific Ricker wavelet, we aimed to balance resolution and penetration depth, providing a clear and accurate synthetic seismogram that aligns well with the characteristics of the seventeen-layer model. Input parameters essential for generating synthetic data are presented in Table 1. The equation $AI = denstiy\ (\rho) * velocity(V_p)$ is utilized to calculate acoustic impedance, incorporating the provided values for density and the p-wave velocity model.

Subsequently, the synthetic data underwent the hybrid optimization process. The objective is to employ an algorithm for the conversion of synthetic data into subsurface acoustic impedance. Addtionally, the generating synthetic data generated to cross-verify the inverted impedance with the predicted impedance. The initial two panels of Figure 2 illustrate the velocities and densities of the 17 layers, utilized as input for synthetic data creation. Futhermore, by multiplying the velocity and density values depicted in panels 1 and 2, one can promptly derive an acoustic impedance. This impedance is then further transformed into reflectivity to produce synthetic data, which is convolved with a Ricker wavelet. Figure 2 panels 3, display this synthetic data along with a solid black line.

In Figure 2, panel 4 illustrates the outcome obtained after applying hybrid optimization to convert it into acoustic impedance. Given the expectation that these two impedances should closely resemble each other, the inverted impedance is compared against the original impedance, which is synthetically generated. Moreover, panel 3 of the hybrid optimization presents a synthetic trace produced using the inverted impedance, allowing a comparison with the original synthetic trace. Figure 2 demonstrates a notable alignment between the inverted impedances and the recreated synthetic impedances for hybrid approaches. The correlation between the hybrid optimization and the modeled original trace is recorded at 0.99. The figure indicates a strong fit between both impedances, affirming the effectiveness of the

technique, as evidenced by the 0.99 correlation between the original and inverted impedance from the hybrid. Further, Figure 3 showcases a cross-plot depicting the original and inverted acoustic impedances achieved through hybrid optimization techniques. The close alignment of results is evident in these cross plots, where scatter points closely approximate the best-fit line. A thorough examination of the cross plot highlights the proximity of data points from the hybrid optimization strategy to the best-fit line, underscoring the effectiveness of the Hybrid algorithm. Based on the analysis, it is decided to apply the created hybrid optimization to real data from the Blackfoot Field in Canada.

Table 1. Observed and modeled AI for synthetic data case comparison.

S.No.	Layers	Impedance	Inverted impedance	Change (%)
1	Layer 1	7040	7147.44	1.0744
2	Layer 2	9065	8662.75	4.0225
3	Layer 3	5700	6341.70	6.417
4	Layer 4	7425	7399.50	0.255
5	Layer 5	10040	9999.57	0.4043
6	Layer 6	8225	8099.61	1.2539
7	Layer 7	9500	10184.16	6.8416
8	Layer 8	11700	11500.89	1.9911
9	Layer 9	6300	6533.15	2.3315
10	Layer 10	10455	10597.13	1.4213
11	Layer 11	7425	7423.60	0.014
12	Layer 12	13500	13700.36	2.0036
13	Layer 13	11700	12156.97	4.5697
14	Layer 14	10000	10198.94	1.9894
15	Layer 15	14144	13999.97	1.4403
16	Layer 16	15568	16041.08	4.7308
17	Layer 17	12720	12911.08	1.9108

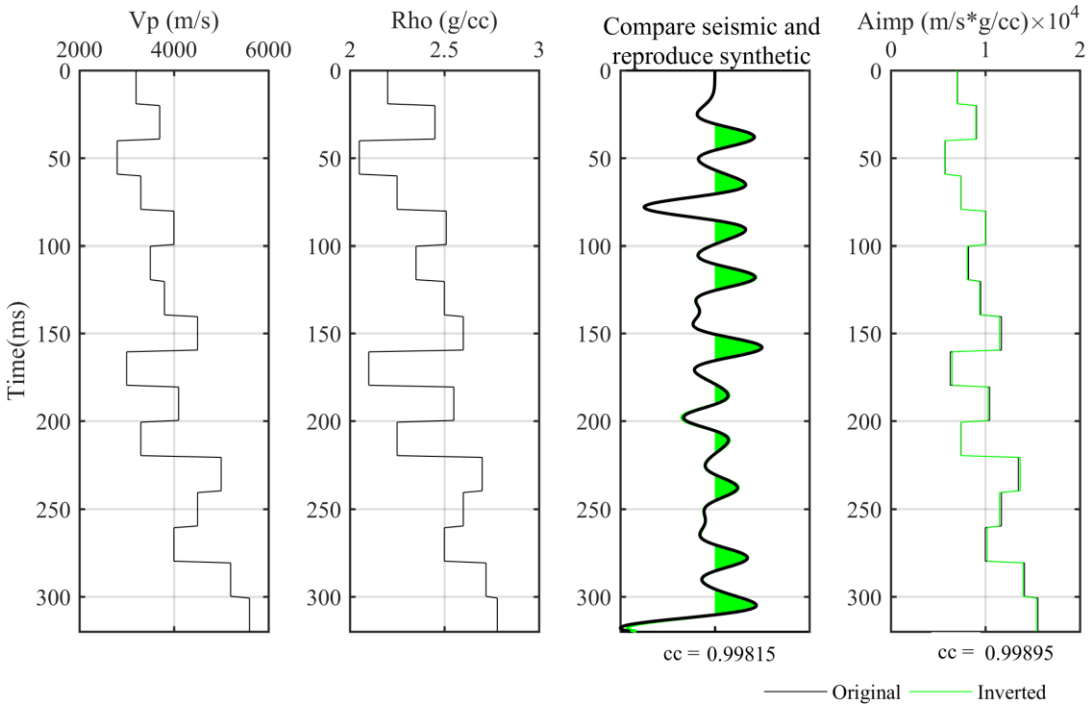

Figure 2. Display of the outcomes of the 1D convolution model applied to synthetic data and seismic inversion.

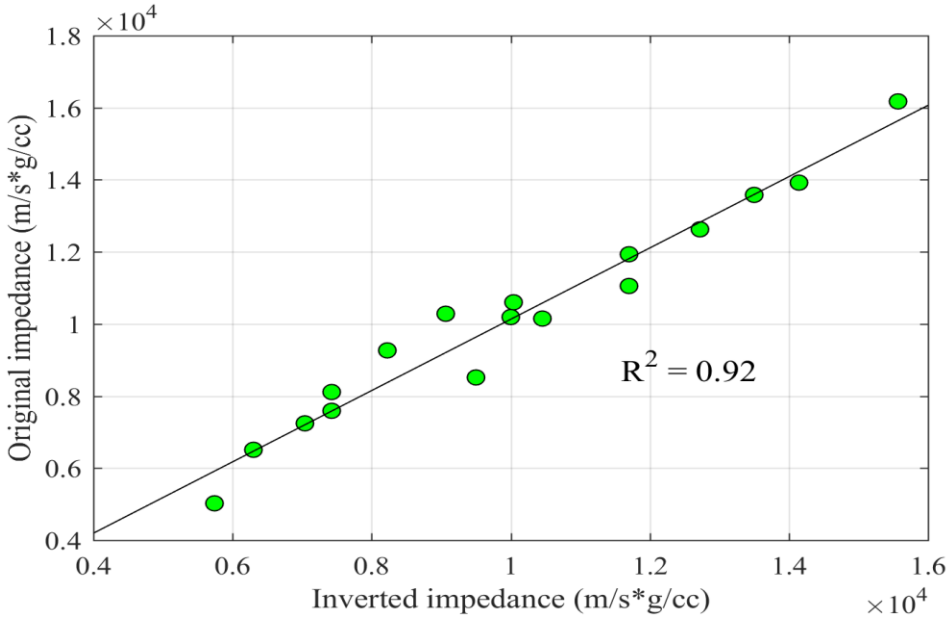

Figure 3. Cross plot between original impedance and inverted impedance

Application to real field data from the Blackfoot field, Canada

The hybrid PSO is applied to data from the Blackfoot Field, Alberta, Canada, in a two-step process. First, a specific seismic trace (composite trace) corresponding to the location of a well or a nearby area is selected, and hybrid optimization is performed on this trace. In the second step, the entire seismic volume is inverted to generate acoustic impedance and porosity volume for the zone between the wells. In this study, well-log data is utilized alongside seismic data to constrain the solution. Since the well-log data is recorded in depth and the seismic data in time, these two datasets cannot be directly integrated. Therefore, a depth-to-time conversion is crucial before performing the inversion. Interpreting horizons within several kilometers of the study area, offers valuable insights into the subsurface structure and helps estimate the depth of geological units. Although the well-log data is manually converted from depth to time (ms), directly aligning it with seismic data is not feasible. Before commencing the inversion process, it is imperative to compute the connection between porosity reflectivity (R_φ) and impedance reflectivity (R_Z), employing the following formula.

$$R_Z = \frac{1}{2}[\log(z_{i+1}) - \log(z_i)] \quad (5)$$

$$R_\emptyset = \frac{1}{2}\left[\left(log\left(\frac{\emptyset_{i+1}}{1-\emptyset_{i+1}}\right)\right) - \log\left(\frac{\emptyset_i}{1-\emptyset_i}\right)\right] \quad (6)$$

In this context, where z_{i+1} and $\emptyset_{i+1}$ represent the impedance and porosity of the $(i+1)^{th}$ layer, and (z_i) and $(\emptyset_i)$ denote the impedance and porosity of the ith layer, respectively. Eqs. 5 and 6 are employed to compute the correlation factor (g), representing the slope of the fitted line. Figure 4a displays a cross plot of porosity reflectivity and acoustic reflectivity, where the best-fit line yields a slope of -0.14. This correlation factor is utilized to generate a porosity wavelet by multiplying the g factor with the impedance wavelet directly extracted from the seismic data. Figure 4b illustrates a comparison between the porosity wavelet and the impedance wavelet, revealing their reverse polarity and the inverse proportionality between porosity and impedance.

Additionally, lower and upper bounds are employed to further confine the search space within the desired range. In this research, the upper and lower bounds were based on the well-log data, and Figure 5 illustrates the results of the inversion analysis for the composite trace near wells 01-08 using HPSO. Figure 5 presents the low frequency impedance and porosity model model (blue solid lines) generated from well log data alongside the lower and upper bounds (dotted blue lines). A comparison of the original (black solid line) and inverted acoustic impedance and porosity (red solid line) is depicted. The AI and porosity derived from well-defined data and inverted data exhibit good agreement. The peak-to-peak values of acoustic impedances and porosity may not match due to the frequency range difference between well log data (20 to 40 kHz) and seismic data (typically 10 to 80 Hz). The correlation between well-log data of impedance and porosity with inverted impedance and porosity obtained through HPSO is 0.79 and 0.71, respectively.

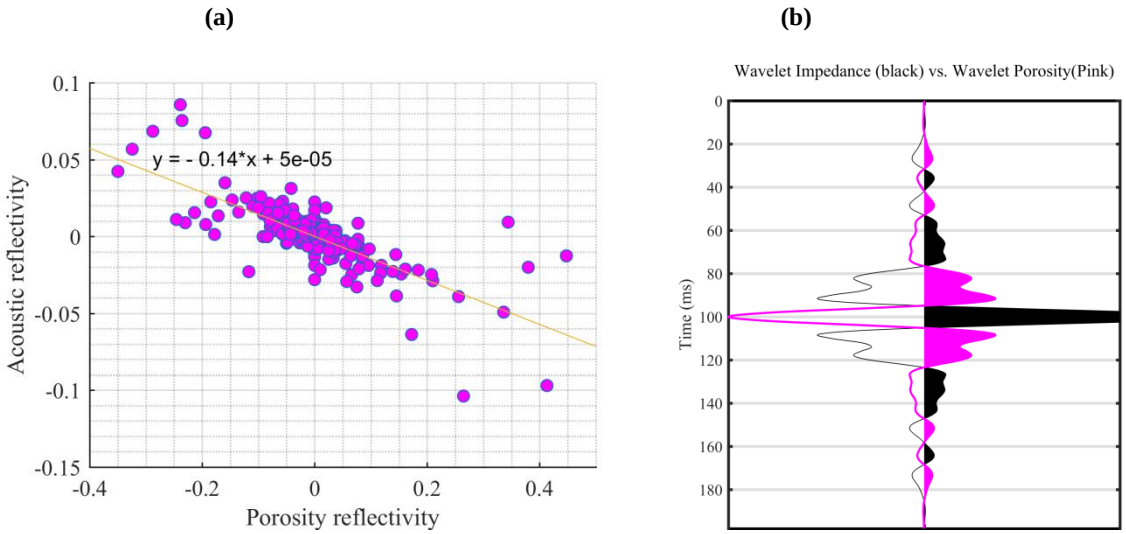

Figure 4. **(a)** A cross plot depicting the relationship between acoustic reflectivity and porosity reflectivity for well 01 − 08_logs, is indicated by a best-fit linear trend, revealing a correlation factor (g = −0.12). **(b)** Comparison between the statistical wavelet (black) and the porosity wavelet (pink), which is generated through the multiplication of the correlation factor with the statistical wavelet.

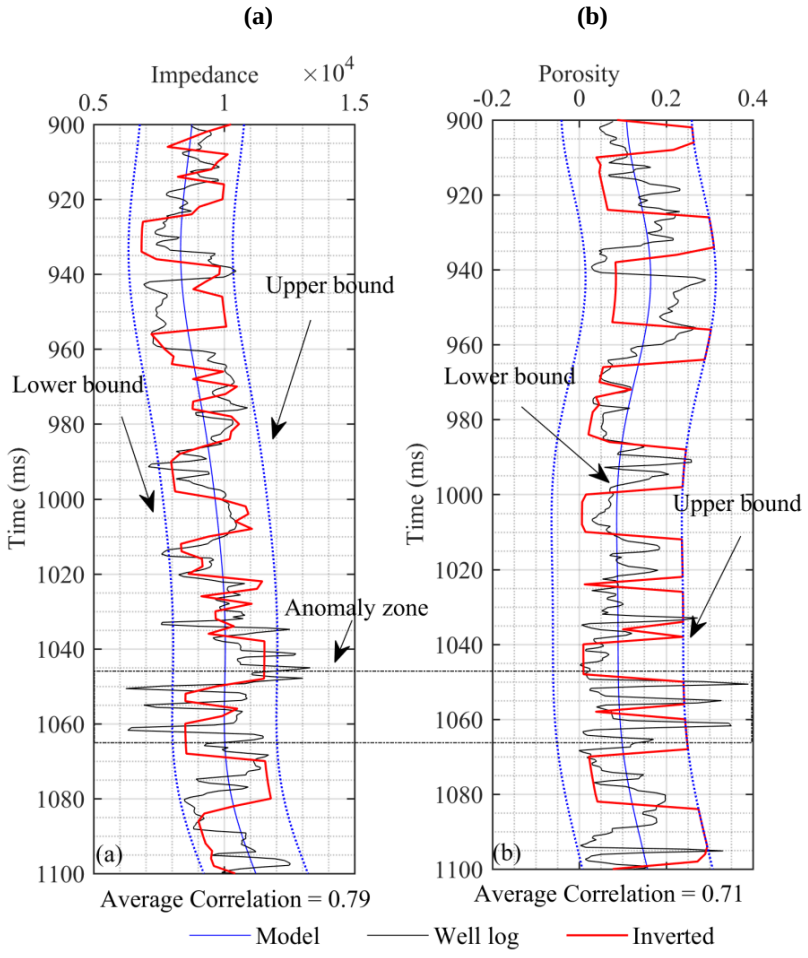

Figure 5. Composite trace analysis near the well 01-08 logs, **(a)** impedance, **(b)** porosity

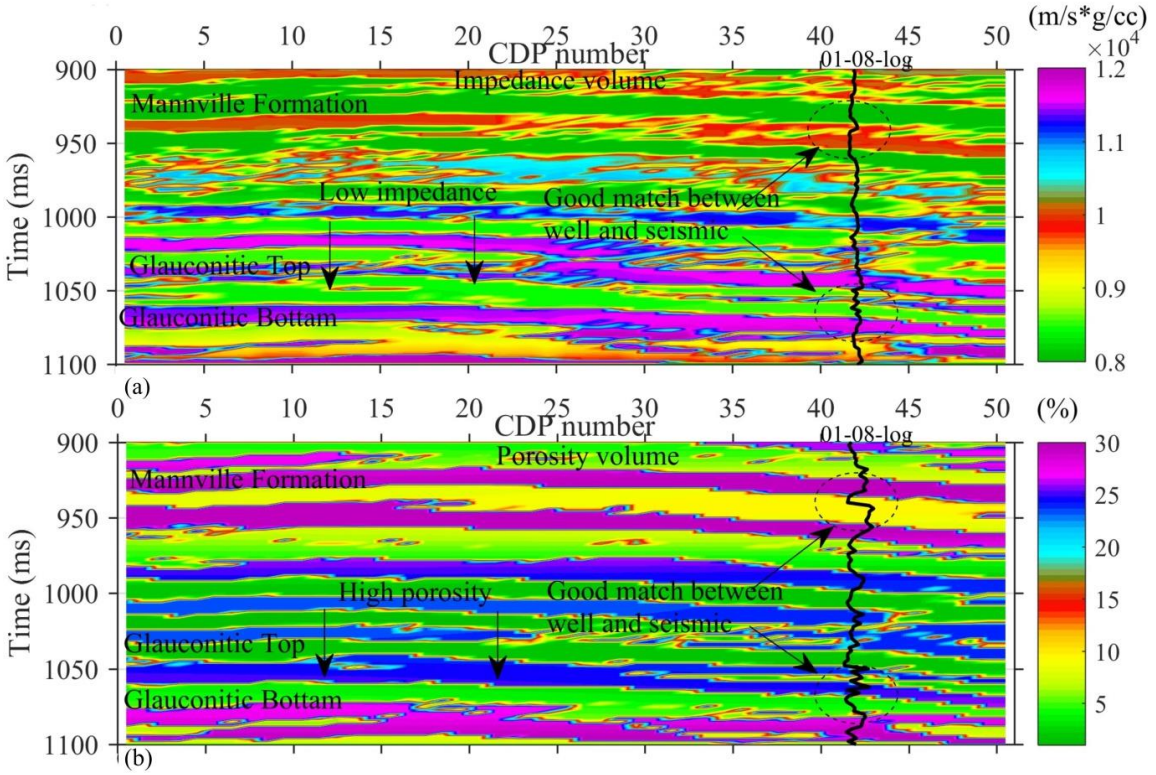

Figure 6. Inverted volume section estimated through HPSO. **(a)** Inverted impedance section and **(b)** porosity volume with well log01-08 log

Following that, the hybrid optimization techniques are applied trace by trace to the CDP stack section to determine the impedance and porosity volume. The inversion is conducted trace by trace, and after inverting all seismic traces using HPSO, the results are plotted against two-way travel time in Figure 6a and 6b, respectively. Figure 6a indicates a good match between the 01-08 log impedance with inverted impedance, with the low impedance zone identified between 1040 and 1065 ms. The boundary at 1040 ms is recognized as a high reflecting layer, as it is surrounded by a high impedance layer (> 11000 m/s ∗ g/cc). Subsequently, Figure 6b presents the porosity volume created by projecting porosity throughout the entire seismic section and the variation of the porosity section at inline 1 with a two-way travel time of 900-1100 milliseconds. The inverted results reveal a very high resolution of the subsurface with layer information, surpassing the interface information provided by the input seismic data. It is observed that the porosity varies from 1 to 30 percent in the study region, and the high porosity zone (> 20%) is situated between 1040 and 1065 ms two-way travel time. The well-log porosity also exhibits a very good agreement with the inverted porosity. Analysis of Figures 6a and 6b reveals that the low impedance zone identified in the inverted impedance section, corresponds to a region of high porosity. This unusual zone, already interpreted in the composite trace between 1040 to 1065 ms two-way travel time, is characterized as a reservoir, specifically a sand channel. In Figure 7, the total variance in inverted impedance and porosity across the 3D volume is illustrated, making it easier to distinguish different zones in this region.

Furthermore, the inverted synthetic traces, generated from the inverted impedance using forward modeling, are compared with the Blackfoot seismic data in Figure 8. Additionally, an inverted synthetic derived from porosity is estimated and similarly compared with the Blackfoot seismic data. The figure is organized into two columns: the first column presents the comparison between the Blackfoot seismic data and the reproduced synthetic traces from both inverted impedance and porosity, while the second column highlights the differences between these comparisons. The replicated synthetic and Blackfoot seismic closely align with each other, as evident in the images. The calculated average correlation between Blackfoot seismic and reproduced synthetically is 0.97 and 0.88, demonstrating a notably high value. These qualitative and quantitative analyses, showcase the effectiveness of the algorithm in this context.

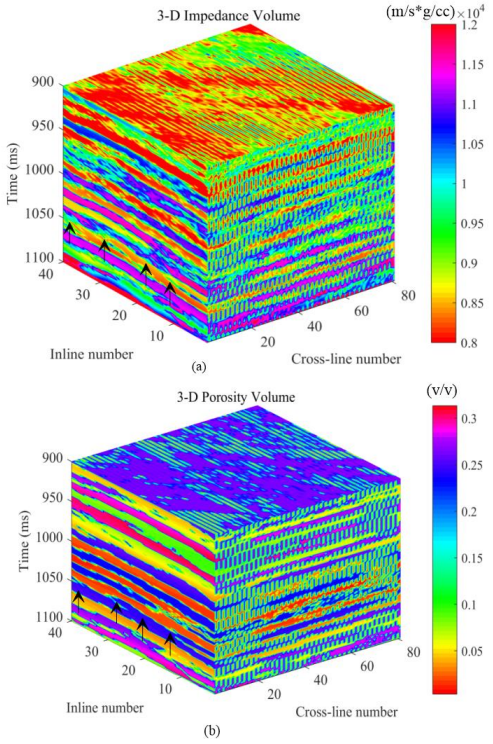

Figure 7. (a) The 3D volume of inverted impedance, and **(b)** porosity, along with the black arrow, highlights the sand channel characterized by low acoustic impedance and high porosity.

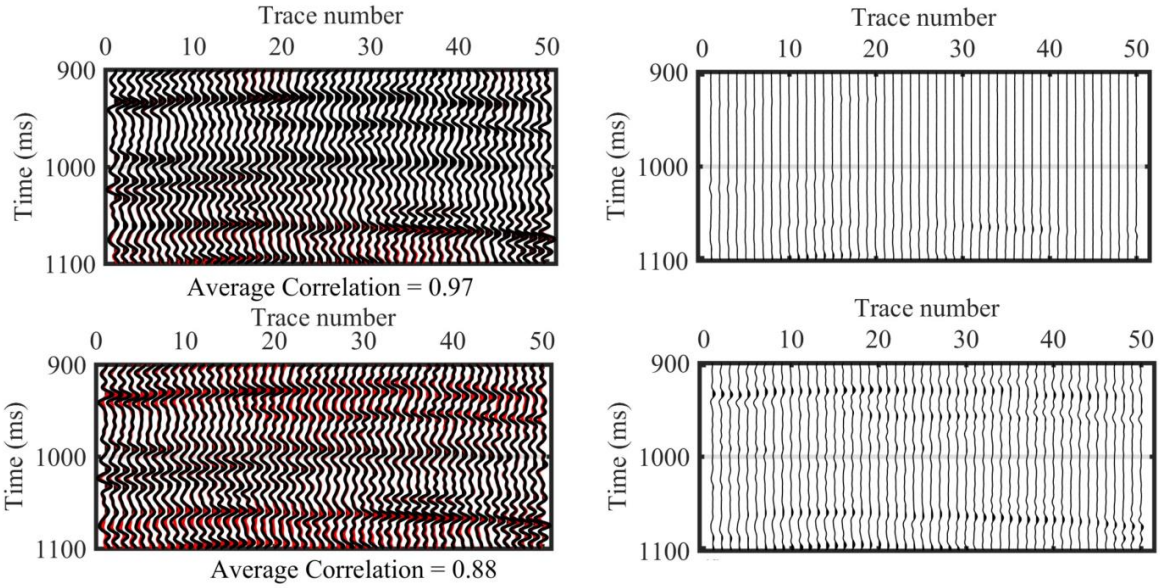

Figure 8. The first columns, Blackfoot seismic and replicated synthetic sections derived from the inverted impedance and porosity estimated through HPSO, respectively. The second column, shows the difference between real and synthetic traces.

Figure 9 illustrates the variance in error with iterations for impedance and porosity. In Figure 9a, the average error for impedance decreases from 2.0 to 1.7 when the stopping criterion is set to 1800, underscoring the effectiveness of particle swarm optimization in yielding improved outcomes. Furthermore, the quasi-Newton method has undergone 1700 iterations, significantly reducing the iteration error. In the case of porosity, Figure 9b demonstrates the error minimization from 2 to 0.55 achieved by HPSO, spanning up to iteration 3100.

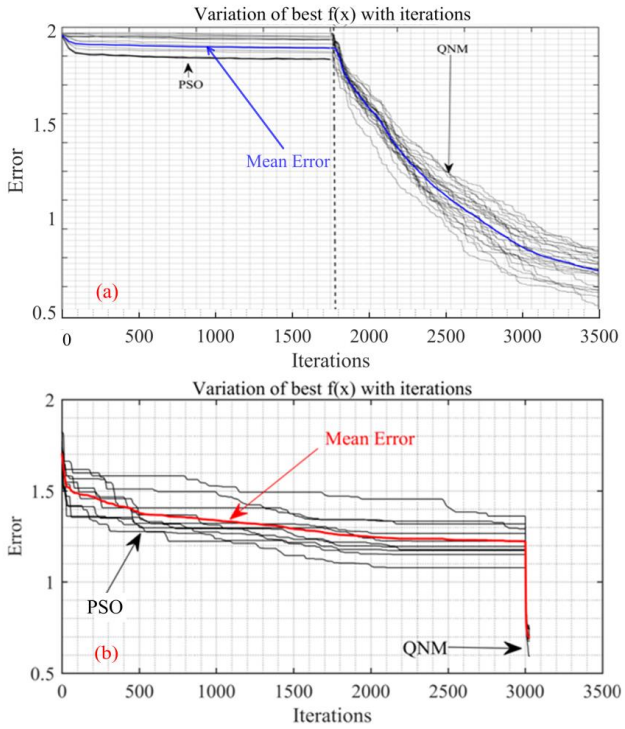

Figure 9. The error variation with iteration is depicted **(a)** for impedance inversion and **(b**) for porosity inversion.

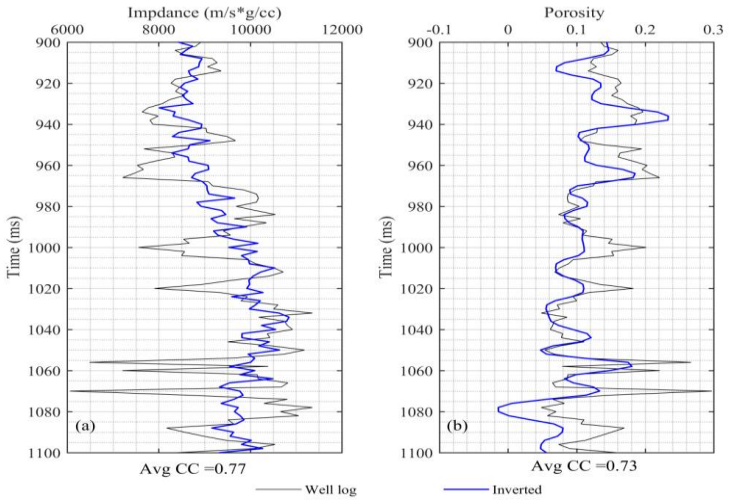

Figure 10. Composite trace analysis near the well 01-08 logs, **(a)** impedance, **(b)** porosity.

Standard inversion results

To compare our results, we selected model-based inversion (MBI), a standard seismic inversion technique widely recognized for its accuracy and reliability in estimating subsurface properties. By comparing our outcomes with those from MBI, we can effectively evaluate the accuracy of our hybrid optimization approach. MBI is a form of local optimization that relies on the least squares method, and its effectiveness is highly dependent on the accuracy of the initial model. If the initial model is inaccurate, the optimization process may become trapped in a local minimum of the misfit function, hindering the accurate extraction of the true subsurface earth model, including impedance and porosity. We first applied MBI techniques at the well location, where the inverted results for impedance and porosity, closely matched the well's actual impedance and porosity, as shown in Figure 10

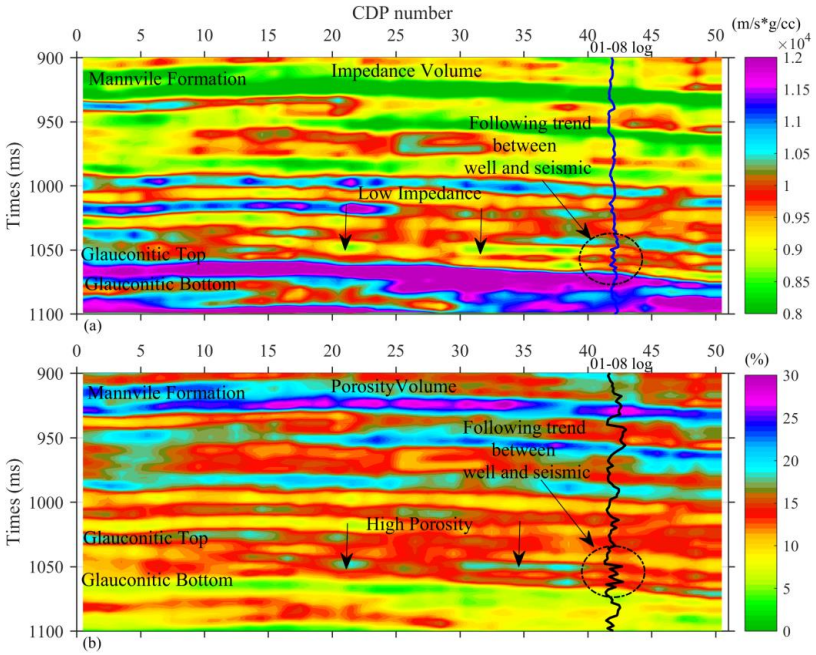

Figure 11. The application of model based inversion and its use for prediction of **(a)** impedance and **(b)** porosity volume

Following these successful results at the well location, we extended MBI to the full volume of seismic data to extract impedance and porosity, as illustrated in Figure 11. Figure 11a shows the inverted impedance, demonstrating that the anomaly zone aligns well with the well data, while Figure 11b presents the porosity volume, revealing the anomaly in patches. However, compared to the hybrid method, these results more effectively resolve thin layers within the anomaly zone, producing high-resolution impedance and porosity volumes. In conclusion, while MBI struggles to resolve thin layers and produces results in a patchy form, the hybrid PSO method effectively resolves both impedance and porosity zones, offering more detailed information about the reservoir zone.

CONCLUSIONS

In the present study, a seismic inversion based on hybrid optimization techniques namely particle swarm optimization (PSO) along with quasi-newton methods (QNM) is applied. The PSO is a global optimization technique which takes large time to converge, whereas QNM is local optimization technique and largely depends on the initial model. The present study combines these two methods together in order to reduce their drawback and enhance their benefits in order to characterize reservoir. These optimization methods require advanced computing capabilities and expertise, they prove to be powerful tools for obtaining high-resolution subsurface information. The inclusion of prior information (well log) in these inversion methods has been demonstrated to reduce convergence time and generate detailed subsurface information. The developed method of seismic inversion based on HPSO has been tested with both synthetic and real data. In synthetic data, the inverted impedance trace closely follows the trend of real impedance, achieving correlation coefficients of 0.99. In real data, HPSO inversions exhibit high-resolution subsurface information, with impedance varying from 6000 to 16000 m/s∗g/cc and porosity from 1 to 30%. The interpretation of inverted sections identifies a low impedance (6000 to 9000 m/s∗g/cc) and high porosity (> 15%) anomaly in the time interval of 1040-1065 ms two-way travel time. This anomalous zone, also interpreted in well-log data, is characterized as a reservoir (sand channel).

ACKNOWLEDGMENTS

The authors would like to extend their appreciation to CGG Geo software for their generous provision of the Hampson Russell software and data, which significantly contributed to the success of this research. Furthermore, one of the authors, S.P. Maurya, expresses sincere gratitude to the funding agencies UGC-BSR (M-14-0585) and IoE BHU (Dev. Scheme no. 6031B) for their crucial financial support, which made this research possible. Special thanks are also owed to www.mathworks.com and www.norsar.no for providing academic licenses for Matlab (2022b). These invaluable resources played an essential role in the successful completion of this work.

Author Credit Statement

RK was involved in conceptualization, methodology design, software development and original draft writing. SPM supervised throughout the research. NV, RS and HR undertook thorough review and editing. APS, R, and KHS conducted validation. GH and PKK took charge of investigations. MKS conducted visualization.

Data availability

The authors do not have permission to share data..

Compliance with Ethical Standards

The authors assert the absence of any competing interests and adhere to copyright norms.

REFERENCES

Bonnans, J.F., Gilbert, J.C., Lemaréchal, C. and Sagastizábal, C.A., 2006. Numerical optimization: theoretical and practical aspects. Springer Science & Business Media.

Bosch, M., Mukerji, T. and Gonzalez, E.F., 2010. Seismic inversion for reservoir properties combining statistical rock physics and geostatistics: a review. Geophysics, 75(5),75A165-75A176

Broyden, C.G., 1970. The convergence of a class of double-rank minimization algorithms 1. General considerations. IMA J. Appl. Math., 6(1), 76-90.

Du, Z. and Macgregor, L.M., 2010. Reservoir characterization from joint inversion of marine CSEM and seismic AVA data using Genetic Algorithms: a case study based on the Luva gas field. In SEG Technical Program Expanded Abstracts. Society of Exploration Geophysicists, 737-741.

Dufour, J., Squires, J., Goodway, W.N., Edmunds, A. and Shook, I., 2002. Case History: Integrated geological and geophysical interpretation case study, and Lamé rock parameter extractions using AVO analysis on the Blackfoot 3C-3D seismic data, southern Alberta, Canada. Geophysics, 67(1), 27-37.

Hema, G., Maurya, S.P., Kant, R., Singh, A.P., Verma, N., Singh, R. and Singh, K.H., 2024. Enhancement of CO2 monitoring in the Sleipner field (North Sea) using seismic inversion based on simulated annealing of time-lapse seismic data. Marine Petrol. Geol., 106962.

Kant, R., Maurya, S.P., Singh, K.H., Nisar, K.S. and Tiwari, A.K., 2024a. Qualitative and quantitative reservoir characterization using seismic inversion based on particle swarm optimization and genetic algorithm: a comparative case study. Sci. Rep., 14(1),22581.

Kant, R., Kumar, B., Maurya, S.P., Singh, R. and Tiwari, A.K., 2024b. Exploring the utility of nonlinear hybrid optimization algorithms in seismic inversion: A comparative analysis. Phys. Chem. Earth, 103754.

Kumar, B., Kant, R. and Maurya, S.P., 2024. Qualitative and quantitative reservoir characterisation using seismic inversion based on global optimization: A comparative case study. J. Earth Syst. Sci., 133(2), 87.

Kushwaha, P.K., Singh, R., Maurya, S.P. and Rai, P., 2023. Prediction of petrophysical properties using post stack seismic inversion and geostatistical techniques over F-3 block, Netherlands-A comparative study. Int. J. Petrol. Technol., 10, 53-70.

Maurya, S.P. and Sarkar, P., 2016. Comparison of post-stack seismic inversion methods: a case study from Blackfoot Field, Canada. IJSER,7(8),1091–1101

Maurya, S.P. and Singh, N.P., 2018. Comparing pre-and post-stack seismic inversion methods-a case study from Scotian Shelf, Canada. J. Indian Geophys. Union, 22(6), 585-597.

Maurya, S.P. and Singh, N.P., 2020. Effect of Gaussian noise on seismic inversion methods. J. Indian Geophys. Union, 24(1), 7-26.

Maurya, S.P., Singh, N.P. and Singh, K.H., 2020. Seismic inversion methods: a practical approach. Springer.

Maurya, S.P., Singh, R., Mahadasu, P., Singh, U.P., Singh, K.H., Singh, R., Kumar, R. and Kushwaha, P.K., 2023. Qualitative and quantitative comparison of the genetic and hybrid genetic algorithm to estimate acoustic impedance from post-stack seismic data of Blackfoot field, Canada. Geophys. J. Int., 233(2), 932-949.

Nocedal, J. and Wright, S.J. eds., 1999. Numerical optimization. New York, NY: Springer New York.

Russell, B.H., Lines, L.R. and Hampson, D.P., 2003. Application of the radial basis function neural network to the prediction of log properties from seismic attributes. Expl. Geophys., 34, 15–23.

Shanno, D.F., 1970. Conditioning of quasi-Newton methods for function minimization. Mathematics of computation, 24(111), 647-656.

Simin, V., Harrison, M.P. and Lorentz, G.A., 1996. Processing the Blackfoot 3C-3D seismic survey. Crewes Res Rep, 8, 39- 1.

Singh, A.P., Maurya, S.P., Kant, R., Singh, K.H., Singh, R., Srivastava, M.K., Hema, G. and Verma, N., 2024. Implementing 4D seismic inversion based on Linear Programming techniques for CO2 monitoring at the Sleipner field CCS site in the North Sea, Norway. Acta Geophysica,1-23.

Received on: 30-09-2024 ; Revised on: 15-10-2024 ; Accepted on:18-11-2024

J. Ind. Geophys. Union, 29(1) (2025), 38-44
https://doi.org/10.71122/JIGU.29(1)2025.004

Impact of solar activity on ~200-year cyclic variations in groundwater recharge rates in the Badain Jaran Desert, Inner Mongolia, Northwest China

Rajesh Rekapalli[1,2], R.K.Tiwari[1] and Animesh Mandal[3]
[1]CSIR-National Geophysical Research Institute, Hyderabad-500007, India
[2]AcSIR- National Geophysical Research Institute, Hyderabad-500007, India
[3]Indian Institute of Technology, Kanpur-208016, India

ABSTRACT

Understanding groundwater recharge variations is crucial for assessing the impact of climatic and solar influences on water resources. We attempt here to quantify the cyclic solar forcing on groundwater recharge rate (GRR) through the analysis of ~ 700 years of GRR data from the dry lands of the Badain Jaran Desert in Northwest China and Total Solar Irradiance (TSI) data using principal component analysis and statistical methods. Our results confirm a significant role of solar activity in groundwater recharge variations. Singular spectrum analysis of GRR and TSI time series reconstructed from the first three principal modes, revealed common spectral peaks, indicating a significant influence of solar activity on GRR. We observed that a small portion of solar variation (~ 0.021%) of TSI appeared in the second and third eigenmodes of TSI, is found to be responsible for the ~200-year cyclic variability. Approximately 33.66% of the GRR variability is attributed to long-term solar activity trends, while 11.81% is associated with the ~200-year Suess solar cycle. Additionally, residual spectral analysis suggests potential influences of shorter solar cycles (63±10 years, 33±3 years, 24±2 years, and 18±2 years) and non-linear solar phenomena. Thus, this study provides critical insights into the coupling between solar activity and groundwater recharge, emphasizing the importance of long-term and cyclic solar influences, in modeling future groundwater scenarios under changing climatic conditions.

Keywords: Groundwater recharge rate, Spectrum analysis, Total Solar Irradiance, Eigenmode, Badain Jaran Desert.

INTRODUCTION

Understanding changes in groundwater recharge is crucial for society, as it requires analyzing the sensitivity of recharge processes to both internal and external factors that influence groundwater availability. These changes are predominantly driven by climatic variations, with temperature, precipitation, and evapotranspiration being among the key factors. Numerous studies have explored the potential links between climate change and water resources (Goderniaux et al., 2009; Green et al., 2011; Newcomer et al., 2014; Rossman et al., 2014; Zhang et al., 2014; Shamir et al., 2015). A detailed statistical or mathematical analysis to identify trends and cyclic patterns in long-term groundwater fluctuation rates, as well as their potential links to influencing processes, is crucial for improving the modeling of groundwater recharge. Since groundwater recharge is increasingly recognized as a proxy for climate change, such an analysis would provide valuable insights into climate and environmental changes. Researchers have compared groundwater recharge rate (GRR) data with various climatic indicators, including tree rings, unsaturated zone profiles, and sunspot numbers, to explore these relationships (Gates et al., 2008; Tiwari and Rajesh, 2014).

Tiwari and Rajesh (2014) have shown evidence of a ~200-year solar suess cycle and its impact on the long-term groundwater recharge rates by analyzing proxy reconstructed GRR (Gates et al., 2008) and Sunspot Number (Solanki et al, 2004) data. They have suggested that ~48% of the recharge is controlled by this ~200-year solar cycle. However, in the above study, a quantified relationship between solar energy (TSI) and GRR was not established. According to them, during the reversal phase of sunspot, the increased TSI through facular excess emission (Frohlich, 2000, 2009) enhances the evaporation of surface water and thereby reduces the infiltration. Such an increase in TSI will also cause a change in the timing and intensity of precipitation, which might affect the groundwater recharge. However, the TSI data was not used in their study to quantify the percentage of TSI variation that drives the groundwater recharge rate variation at ~200-year periodicity. Therefore, in the present study, we use advanced statistical and spectral methods to identify the significant correlations between GRR and TSI, to estimate the percentage of TSI variation responsible for ~200-year cyclic variation in GRR.

METHODS AND DATA SOURCES

Singular Spectrum Analysis (SSA)

The time series X(t) of length N is embedded into the trajectory matrix $T_{l\times k}$ using an appropriate window length 'l' guided by weighted correlation (here k=N-l+1). In the next step, we apply singular value decomposition to decompose the trajectory matrix into eigenvectors and eigenvalues as shown in Equation 1.

$$T = \sum_{i=1}^{d} \sqrt{\lambda_i} U_i V_i^T \qquad (1)$$

Where λ_i is the i^{th} Eigen value corresponding to the i^{th} eigenvector U_i of TT^T. The triple ($\sqrt{\lambda_i}$,U_i, V_i) is called the i^{th} Eigen triple and d is the number of Eigen triples with nonzero Eigenvalues. We identify the significant individual and paired Eigen triplets from proper analysis of Eigen spectrum

and Eigenvectors for principal component/Eigenmode reconstruction. From these identified Eigen triplets, we reconstruct the trajectory matrix using the following equation 2.

$$Tr = \sum_{G} \sqrt{\lambda_i}\, U_i V_i^T \quad (2)$$

Here the summation is over the selected Eigen triplets denoted by group G. Finally, the Eigenmodes / principal components can be obtained through the diagonal averaging of the reconstructed trajectory matrix (Vautard and Ghil, 1989; Golyandina et al., 2001; Tiwari and Rajesh, 2014; Rekapalli and Tiwari, 2015).

Eigen weighted cross-correlation

Although the qualitative analysis of eigenmodes of different data sets explains the physical process and relationship between them, cross-correlation coefficients help to quantify the relation. Pearson's cross-correlation coefficients are computed between the principal/eigenmodes of two-time series data to identify their association or dynamical influences. The cross-correlation coefficients between different eigenmodes are generally calculated by giving equal weight to each Eigenmode. However, we have noticed a problem with the standard sample cross-correlation coefficient calculation approach as different eigenmodes contribute differently to the entire process. We suggested a new approach in which Eigenvalues are introduced as weights in the correlation coefficient computation to overcome the above (Rajesh and Tiwari, 2018). Eigen weighted cross-correlation coefficient (ECC) between Eigenmodes A and B of two different time series with eigenvalue percentages 'a' and 'b' is given as

$$c_{net} = \frac{c * (a + b)}{2} \quad (3)$$

Here 'c' is the sample cross-correlation coefficient between the eigenmodes A and B. The following example illustrates the above idea. Consider the cross-correlation coefficient estimated between two modes of respective eigenvalue percentages 0.2 and 0.5 is 0.9. However, this value (i.e., 0.9) may not suggest a strong correlation between the two data sets because the Eigenmodes with 0.2 and 0.5 eigenvalue percentages represent 20% and 50% of the respective time series. Hence, we propose the above formula (eq. 3) for more accurate quantification of Eigenmode correlations that signify the physical relationship between the source data.

If we use equation (1) for the above example, the net Eigen weighted correlation between the two eigenmodes with eigenvalue percentages 0.2 and 0.5 respectively and a standard cross-correlation of 0.9 is

$$c_{net} = \frac{0.9 * (0.2 + 0.5)}{2} = 0.315$$

If a single eigenmode from the first dataset correlates with multiple eigenmodes from the second dataset, the net correlation coefficient is calculated by summing the correlation coefficients of all individual correlating pairs. This net correlation gives us the quantitative estimate for the physical relationship between two processes related to the two Eigenmodes.

Groundwater recharge rate (GRR) data

Groundwater recharge history (mm/year) of 700 years reconstructed using the mass balance of chloride from densely sampled homogeneous profile (Edmunds et al., 2006) of the unsaturated zone, taken from Gates et al (2008), is used in the present analysis (Tiwari and Rajesh, 2014). According to Gates et al (2008), the timing of decadal or century-scale fluctuations cannot be reliably discerned due to the uncertainty in chloride (CL) inputs. Hence, the groundwater recharge record may show some resolution problems and phase errors (Gates et al, 2008; Tiwari and Rajesh, 2014). However, the recharge history shows the wet periods around AD 1380, 1580, and 1750, approximately with ~ 200-year intervals with dominant quasi-periodic dry phases in between. Also, some intermittent short-term wet and dry periods were observed between 1800 – 1900 (Tiwari and Rajesh, 2014).

Total Solar Irradiance (TSI) data

The TSI data used in the present study is part of 9300 years of solar irradiance reconstructed from the open solar magnetic field, estimated from cosmogenic radionuclide ^{10}Be (Steinhilber et al., 2008, 2009) measured in ice cores GRIP (Vonmoos et al., 2006) and South Pole (McCracken et al., 2004), besides neutron monitor count rates (Usoskin et al., 2005). The data at 5 years resolution are re-sampled from 40-year running means. This is one of the best available TSI data to test the claimed links between groundwater recharge rate and TSI.

RESULTS and DISCUSSION

Role of solar activity on groundwater recharge

The raw data of GRR and TSI (Figures 1a and 1b) show a common long-term trend along with superimposed short-term nonstationary oscillations. Pearson's correlation coefficient of 0.61 was noticed between the groundwater recharge rate and TSI raw data sets. SSA allows us to

scrutinize such complex data to identify independent principal modes for physical interpretation. The GRR and TSI data (Fig. 1) are decomposed using the SSA method using the window length of 40 and 200 years respectively. We have estimated these window length values using the weighted correlation method (Tiwari and Rajesh, 2014; Tiwari et al., 2016). The statistical validation of errors and resolution of the GRR and TSI data are systematically verified and discussed by us and by several other researchers (Gates et al, 2008; Steinhilber et al., 2008, 2009; Tiwari and Rajesh, 2014). The first three principal modes of GRR and TSI data sets represent the long periodic trend and oscillatory components. Hence, we analyze the GRR and TSI signals reconstructed from the first three principal modes shown in Figure 2a (Tiwari and Rajesh, 2014) to demonstrate the relationship between GRR and TSI. The amplitude of ~200-year periodic variation in GRR increased gradually from 1305 to 1985. But, the amplitude of the ~ 200-year cyclic mode of TSI gradually decreased from 1305 to 1985. One can visually see from Figure 2a that the peak changes appeared in GRR amplitudes (maximum to minimum) during the lowest TSI variation. The standard sample cross-correlation (Box et al., 1994) along with the p-value of the Null hypothesis rejection test for randomness in correlation and Eigen-weighted cross-correlation coefficients computed between the SSA reconstructed signals (Fig. 2a) at different Lags are shown in Figure 2b. The sample cross-correlation coefficient is higher compared to Eigen-weighted cross-correlation coefficients. The cyclic pattern observed in the correlation analysis (Fig. 2b) attests to the common ~200-220-year periodic component in both data sets as discussed in our previous study (Tiwari and Rajesh, 2014). The shift in peak cross-correlation from zero value may be either due to errors in the dating process or the 40-year running average used in the reconstruction of TSI data. However, as we are not interested in searching for the periodic oscillations of periods less than 40 years, the lag observed in the cross-correlation is not significant enough to influence our results. Further, Figure 2c and Figure 2d show the spectrum of SSA-reconstructed GRR and TSI signals respectively. The spectrum of GRR and TSI data reveal dominant common spectral peaks at periods of ~200±20 (Suess cycle), and 512±25 (Trend) years with more than 99% confidence levels (Tiwari et al., 2016). Hence, our results suggest a persuasive role of solar activity on groundwater recharge rate via a long-term trend and ~200±20-year solar Suess cycle.

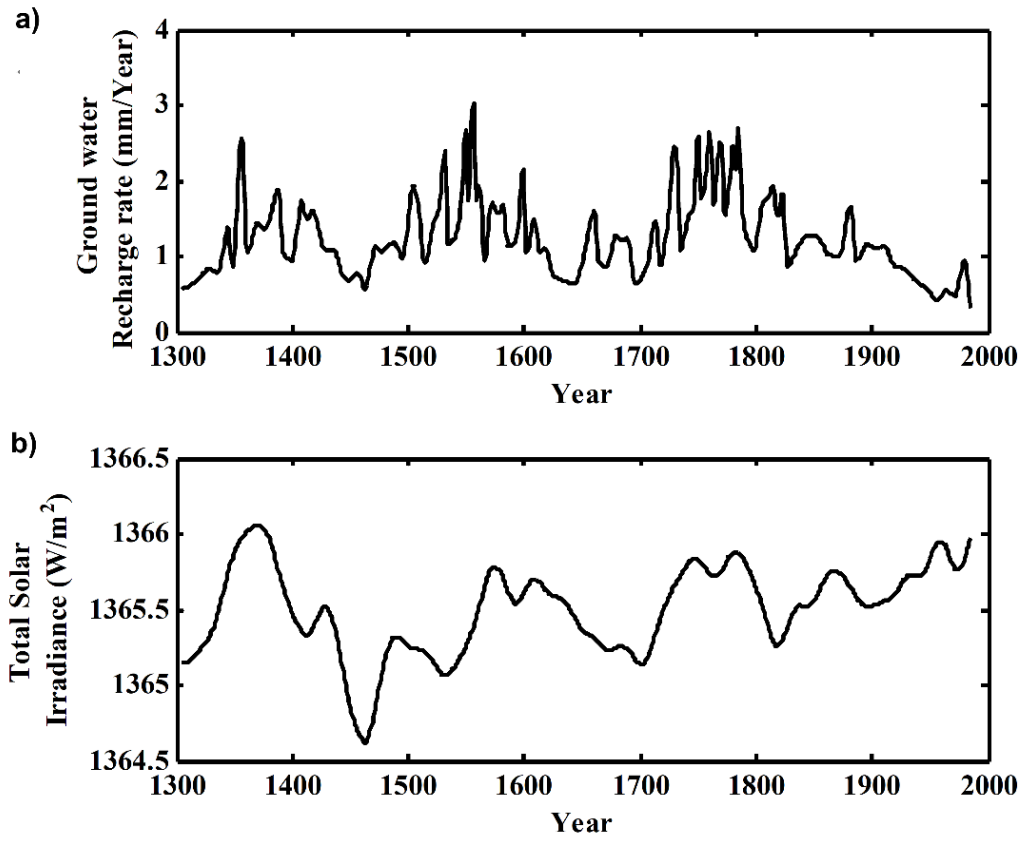

Figure 1. Raw data of (**a**) Groundwater recharge rates, and (**b**) Total Solar Irradiance data

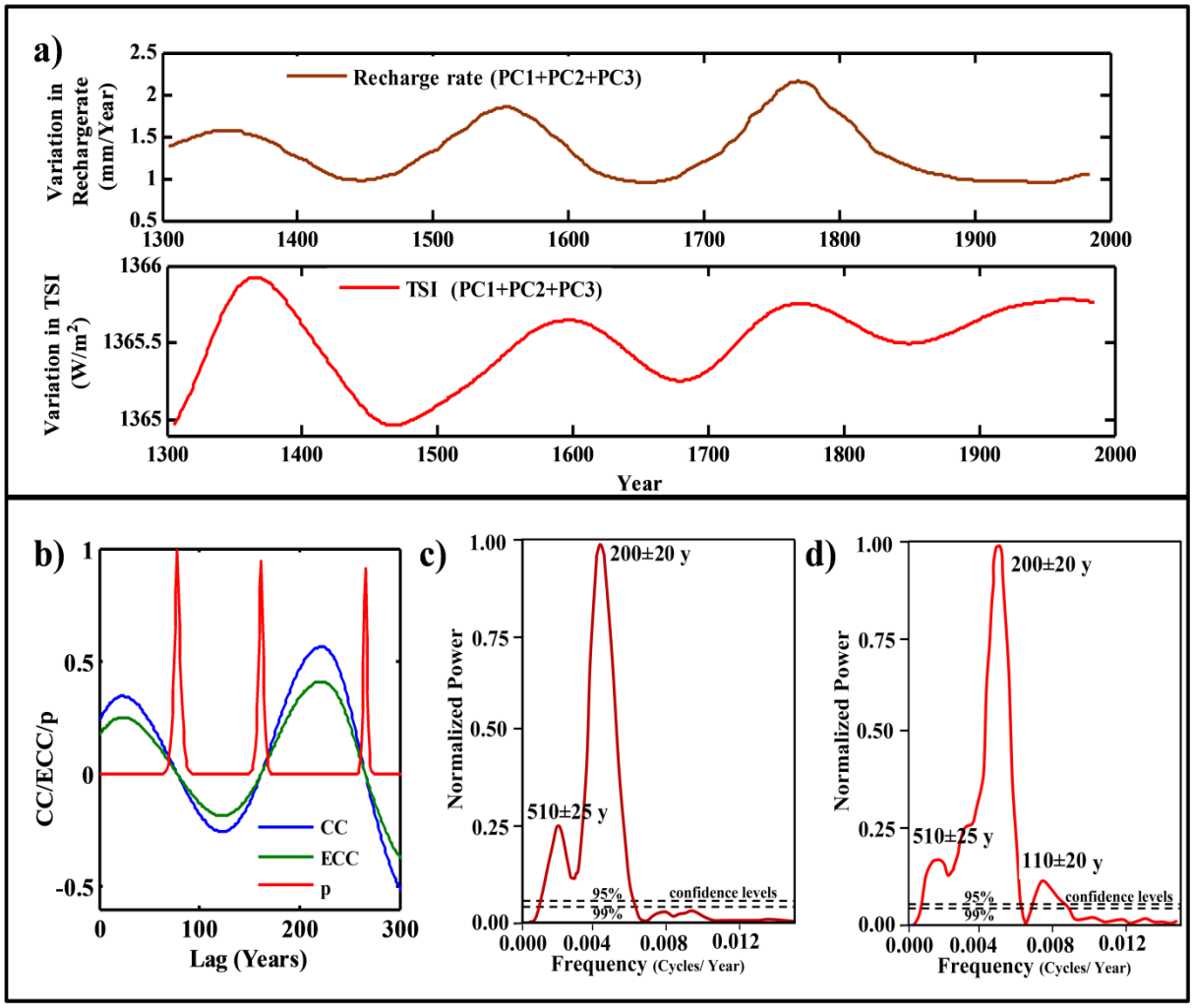

Figure 2. (**a**) Groundwater recharge rate (top panel) and total solar irradiance (bottom panel) data reconstructed using SSA from principal components 1 to 3. (**b**) Correlation coefficients estimated using conventional cross-correlation (CC) along with the probability (p) estimated for the rejection of null hypothesis and Eigen weighted cross-correlation (ECC). (**c**) Spectrum of SSA reconstructed recharge rate data. (**d**) Spectrum of SSA reconstructed TSI data

Sensitivity of 200-year groundwater cycle to TSI variation

As discussed above, TSI influences the GRR via long-term trend and ~200±20 year Suess cycle. The first Eigenmodes of GRR and TSI data shown in Figure 3a, contribute nearly 33.66% and 99.94% variance of total recharge and solar irradiance respectively and also depict long-term trends. The trend components of GRR and TSI seem to be part of long periodic cycles with periodicity greater than or equal to the length of the data, which is not discernible here (Rekapalli and Tiwari, 2020). The first mode of GRR correlates well with the long-term trend of TSI with an eigen-weighted correlation coefficient of 0.52 (sample cross-correlation coefficient: 0.79) as shown in Figure 3b. Eigen weighted cross-correlation coefficient suggests that the forcing by the trend of the TSI on GRR is quite significant for modeling future patterns of groundwater recharge scenarios. Unlike groundwater recharge, solar irradiance follows cycles up to million-year periodicities or greater (Tiwari, 2005). The trend in the TSI replicates the parts of several long periodic solar cycles. Hence, it is inappropriate to conclude that the 99.94% variability in the first principal component of TSI is responsible for the observed 33.66% variability in the GRR. In the future, the availability of longer records may allow for discerning the percentage of solar irradiance responsible for 33.66% variability in the GRR. However, we infer here that the 33.66% groundwater recharge rates do not follow the ~200-year solar cycle and may be regarded as a part of some higher-order cycles.

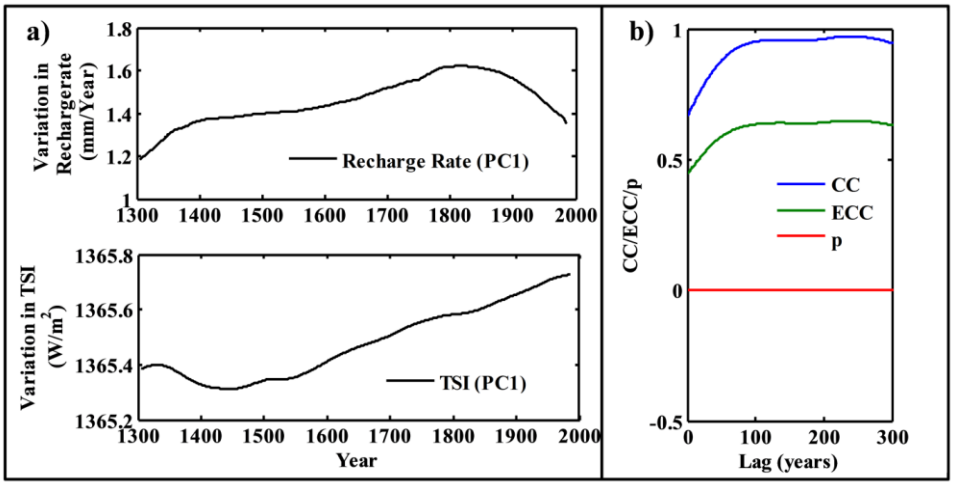

Figure 3. (**a**) The first principal component of Groundwater recharge rate (PC1) and TSI (PC1) reconstructed using SSA. (**b**) Cross-correlation coefficient (CC) along with the probability (p) for rejection of null-hypothesis on their correlation (red line) and Eigen weighted cross-correlation coefficient (ECC) computed between first principal components of GRR and TSI.

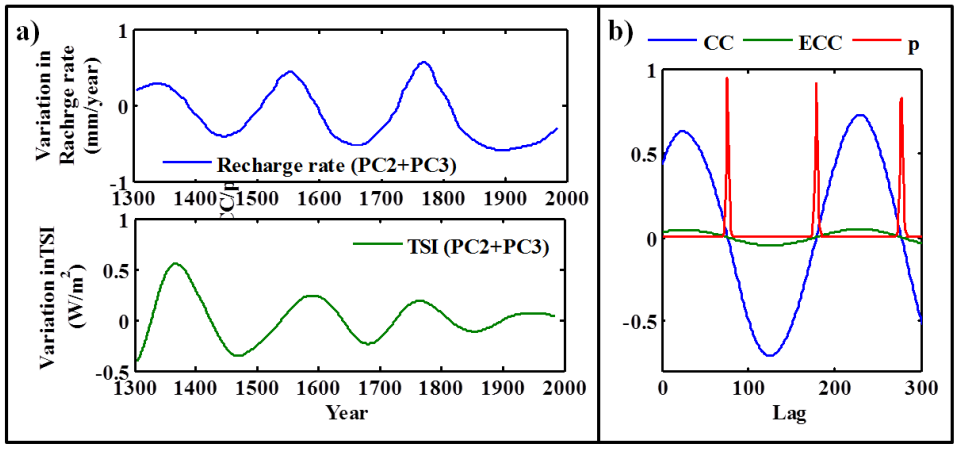

Figure 4. (**a**) Variation in Groundwater recharge rate (PC2+PC3) and TSI (PC2+PC3) reconstructed using SSA. (**b**) Cross-correlation coefficient (CC) along with the probability of Null hypothesis rejection (red line) and Eigen weighted cross-correlation coefficient (ECC) of Groundwater recharge rate (PC2+PC3) and TSI(PC2+PC3).

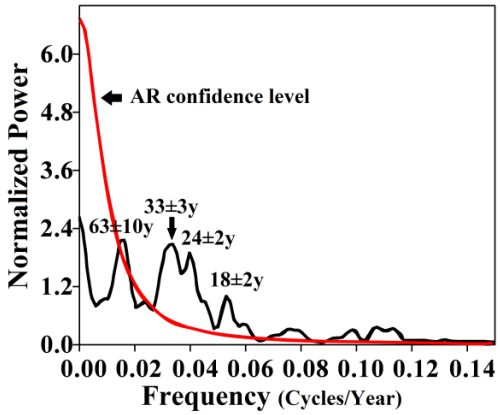

Figure 5. The power spectrum of the residual GRR signal was reconstructed from eigen modes 2 to 40 using SSA, which depicted the spectral peaks at some solar and other nonlinear periods due to beats and modulations.

The second and third modes of TSI (0.012%, 0.009%) and GRR (6.45%, 5.36%) shown in Figure 4a, are cyclic with a periodicity of ~200-205 years. There is a gradual increase in the amplitude of this cycle in GRR from 1305 to 1985 whereas, a gradual decrease in the ~200-year cyclic component of TSI. This suggests the enhanced groundwater recharge conditions due to the reduction in the evapotranspiration of surface water, caused by reduced surface temperatures during low TSI. The cross-correlation along with the null hypothesis probabilities and Eigen Weighted cross-correlation estimated at different lags, are shown in Figure 4b. The pure cyclic nature of the correlation suggests the existence of the same periodicity in both data sets. The peak correlation is observed at lag 23. From the eigenvalue percentage of these modes, only 0.021% of total solar irradiance is responsible for such a ~200 cyclic variation (11.81%) in the groundwater recharge. A sample correlation coefficient of 0.63 was noticed between the SSA reconstructed signal (from PC2 and PC3) of GRR and TSI. However, low-value eigen-weighted cross-correlation suggests (0.044) relatively low significance of this mode (only 11.81% of the total variance) in the groundwater recharge. This year solar cycle is prominent in many paleoclimate indicators (Tiwari, 2005). The correlation of climate processes with solar activity has been pervasive in the past 10,000 years, especially in dry and wet spells (Verschuren et al., 2000; Zang et al., 2008; Lean, 2010). Several studies inferred the ~200-year solar cycle as a dominant and important cycle that influenced the Earth's climate during Holocene (Eddy, 1976; Vasilev et al., 1999; Muscheler et al., 2003; Tiwari, 2005).

Although Tiwari and Rajesh (2014) have successfully discussed the first three eigenmodes in the GRR data, the contribution of 54.53% residual signal to the total GRR was not analyzed. Finally, we estimated the spectral content of the residual (PC4 to PC40) of GRR as shown in Figure 5. We have computed an Auto Regression (AR) based confidence level to avoid the influence of erratic noise present in the record. The spectral peaks identified with 63±10y, 33±3y, and 24±2y, are consistent and may correspond to some lower-order solar periods. The component with 18±2y may be due to some nonlinear phenomenon of solar components as discussed in Scafetta (2012). The spectral analysis of residual signals, within the limits of the data resolution, also stands as evidence of solar forcing on groundwater recharge rates. Chapanov et al. (2017) calculated the decadal harmonics of TSI, LOD-Length Of Day, MSL-Mean Sea Level precipitation, and temperature over Eastern Europe are analyzed using models of the Jose, de Vries, and Suess cycles (periods: 178.7, 208, and 231 years) and their phase differences. The periodic decadal cycles (e.g., 33.0, 29.7, 25.7, 23.1 years) seen in the modeling results highlight solar-terrestrial interactions. This further suggests the role of solar-terrestrial interactions on the decadal cycles observed in GRR residual.

CONCLUSIONS

We analyzed the principal components/eigenmodes in the 700-year record of groundwater recharge rate data from China along with solar activity (Total Solar Irradiance) using a new eigen-weighted cross-correlation method to report the percentage of solar radiation that is responsible for observed trends and cyclic patterns in GRR. Our result suggests that only 11.81% of GRR is associated with the solar Suess cycle. A part of GRR (33.66%) is associated with the long-term trend in solar activity. A small fraction i.e., 0.021% of the total solar radiation is responsible for the observed 200±10y cyclic groundwater recharge variations. Although the data resolution is limited, the residual analysis revealed the influence of short-term solar periods and some non-linear beating phenomena on groundwater recharge rates from China.

Acknowledgments

We thank the Director, CSIR-NGRI for his kind permission to publish this work. We acknowledge Prof. John. B. Gates for groundwater recharge rate data and Prof. F. Steinhilber for TSI data. (Ref: NGRI/Lib/2024/Pub-138)

Author Credit Statement

Rajesh Rekapalli: Conceptualization, methodology, formal analysis, interpretation and writing the original draft and edits. R. K. Tiwari: Interpretation and writing the original draft and edits. Animesh Mandal: Interpretation and writing the original draft and edits.

Data Availability

The data sets used in this study are can be accessed from the sources cited in the manuscript.

Compliance with Ethical Standards

The authors declare no conflict of interest and adhere to copyright norms.

REFERENCES

Box, G. E. P., Jenkins, G. M. and Reinsel, G. C., 1994. Time Series Analysis: Forecasting and Control. 3rd ed. Englewood Cliffs, NJ: Prentice Hall.

Chapanov, Y., Ron, C. and Vondrak, J., 2017. Decadal cycles of Earth rotation, mean sea level and climate, excited by solar activity. Acta Geodyn. Geomater, 14, 241-250.

Eddy, J. A., 1976. The Maunder Minimum: The reign of Louis XIV appears to have been a time of real anomaly in the behavior of the sun. Science, 192(4245), 1189-1202.

Edmunds, W. M., Ma, J., Aeschbach-Hertig, W., Kipfer, R. and Darbyshire, D. P. F., 2006. Groundwater recharge history and hydrogeochemical evolution in the Minqin Basin, North West China. Appl. geochemistry, 21(12), 2148-2170.

Frohlich, C., 2000. Observations of Irradiance Variations. Space Sci. Rev., 94(1-2), 15-24.

Fröhlich, C., 2009. Observational evidence of a long-term trend in total solar irradiance. Astron. Astrophys., 501, 27–30, doi:10.1051/0004-6361/200912318.

Gates, J. B., Edmunds, W. M., Ma, J. and Sheppard, P. R., 2008. A 700-year history of groundwater recharge in the drylands of NW China. The Holocene, 18(7), 1045-1054.

Goderniaux, P., Brouyere, S., Fowler, H.J., Blenkinsop, S., Therrien, R., Orban, P. and Dassargues, A., 2009. Large scale surface-subsurface hydrological model to assess climate change impacts on groundwater reserves. J. Hydrology, 373, 122–138. doi:10.1016/j. jhydrol.2009.04.017

Golyandina, N., Nekrutkin, V. and Zhigljavsky, A. A., 2001. Analysis of time series structure: SSA and related techniques. CRC press

Green, T.R., Taniguchi, M., Kooi, H., Gurdak, J.J., Allen, D.M., Hiscock, K.M., Treidel, H. and Aureli, A., 2011. Beneath the surface of global change: impacts of climate change on groundwater. J. Hydrology, 405, 532–560.

Lean, J. L., 2010. Cycles and trends in solar irradiance and climate. Wiley interdisciplinary reviews: climate change, 1(1), 111-122.

McCracken, K.G., McDonald, F.B., Beer, J., Raisbeck, G. and Yiou. F., 2004. A phenomenological study of the long term cosmic ray modulation, 850-1958AD. J. Geophys. Res., 109, A12103, doi:10.1029/2004JA010685

Muscheler, R., Beer, J. and Kromer, B., 2003. Long-term climate variations and solar effects. Proceedings of the ISCS 2003 on Solar Variability as an Input to the Earth's Environment, vol. 535, pp. 305-316

.Newcomer M.E., Gurdak, J.J., Sklar, L.S. and Nanus, L., 2014. Urban recharge beneath low impact development and effects of climate variability and change. Water Resour. Res., 50, 1716–1734

Rajesh, R. and Tiwari, R.K., 2018. Impact of solar cycles on groundwater recharge on decadal to centennial scale: A case study from Northwest China. Abstract volume, 55th Annual Convention of Indian Geophysical Union, Dec 2018, p14.

Rekapalli, R. and Tiwari, R. K., 2015. A short note on the application of Singular Spectrum Analysis for Geophysical Data processing. J. Ind. Geophys. Union 19(1), 77-85.

Rekappali, R. and Tiwari R.K., 2020. Breaks in linear trends or parts of cycles?, Pure Appl. Geophys. 177 (2020), 5469–5474, https://doi.org/10.1007/s00024-020-02577-y

Rossman, N.R., Zlotnik, V.A., Rowe, C.M. and Szilagyi, J., 2014. Vadose zone lag time and potential 21st century climate change effects on spatially distributed groundwater recharge in the semi-arid Nebraska Sand Hills. J. Hydrology 519, 656-669.

Scafetta, N., 2012. Multi-scale harmonic model for solar and climate cyclical variation throughout the Holocene based on Jupiter–Saturn tidal frequencies plus the 11-year solar dynamo cycle. J. Atmosph. Solar-Terrestrial Phys., 80, 296-311.

Shamir, E., Megdal, S.B., Carrillo, C., Castro, C.L., Chang, H.I., Chief, K., Corkhill, F.E., Eden, S., Georgakakos, K.P., Nelson, K.M. and Prietto, J., 2015. Climate change and water resources management in the Upper Santa Cruz River, Arizona. J. Hydrology, 521, 18-33.

Solanki, S. K., Usoskin, I. G., Kromer, B., Schüssler, M. and Beer, J., 2004. Unusual activity of the Sun during recent decades compared to the previous 11,000 years. Nature, 431(7012), 1084-1087.

Steinhilber, F., Abreu, J. A. and Beer, J.,2008. Solar modulation during the Holocene. Astrophys. Space Sci. Trans., 4, 1-6

Steinhilber, F., Beer, J. and Fröhlich, C., 2009. Total solar irradiance during the Holocene. Geophys. Res. Lett., 36, L19704, doi:10.1029/2009GL040142.

Tiwari, R. K., 2005. Geo-spectroscopy. Capital Publishing Company.

Tiwari, R. K. and Rajesh, R., 2014. Imprint of long-term solar signal in groundwater recharge fluctuation rates from Northwest China. Geophys. Res. Lett., 41(9), 3103-3109.

Tiwari, R. K., Rajesh, R. and Padmavathi, B., 2016. Evidence of Higher-Order Solar Periodicities in China Temperature Record. Pure Appl. Geophys., 1-10.

Usoskin, I.G., Alanko-Huotari, K., Kovaltsov, G.A. and K. Mursula. 2005. Heliospheric modulation of cosmic rays: Monthly reconstruction for 1951-2004. J. Geophys. Res., 110, A12108, doi:10.1029/2005JA011250

Vasil'ev, S. S., Dergachev, V. A. and Raspopov, O. M., 1999. Sources of long-term variations in the radiocarbon concentration in the earth's atmosphere. Geomag. Aeronomy, 39(6), 749.

Vautard, R. and Ghil, M., 1989. Singular spectrum analysis in nonlinear dynamics, with applications to paleoclimatic time series. Physica, D 35, 395-424.

Verschuren, D., Laird, K.R. and Cumming, B.F., 2000. Rainfall and drought in equatorial east Africa during the past 1100 years. Nature, 403, 410–414.

Vonmoos, M., Beer, J. and Muscheler, R., 2006. Large variations in Holocene solar activity: Constraints from 10Be in the Greenland Ice Core Project ice core. J. Geophys. Res., 111, A10105, doi:10.1029/2005JA011500

Zhang, P., Cheng, H., Edwards, R. L., Chen, F., Wang, Y., Yang, X.et al., 2008. A test of climate, sun, and culture relationships from an 1810-year Chinese cave record. Science, 322(5903), 940-942.

Zhang, Y., Wang, J.C., Jing, J.H. and Sun, J.C., 2014. Response of groundwater to climate change under extreme climate conditions in North China Plain. J. Earth Sci. China, 25, 612–618.

Received on: 11-06-2024 ; Revised on: 08-01-2025 ; Accepted on: 08-01-2025

J. Ind. Geophys. Union, 29(1) (2025), 45-55
https://doi.org/10.71122/JIGU.29(1)2025.005

Finite Element solutions of Maxwell fluid flow towards a stretching surface with addition of thermal radiation, porous medium and magnetic field

Nagaraju Bathula* and Kishan Naikoti
Department of Mathematics, Osmania University, Hyderabad-500007, Telangana, India.
*Corresponding author: bnag2014@gmail.com

ABSTRACT

Numerical simulations were used to study the flow of a Maxwell fluid across a non-linear stretching sheet. The effects of thermal radiation, magnetic field, and porous media, were all taken into account within the parameters of the experiment. The non-linear governing equations and the associated boundary conditions were solved using an approach called the finite element technique. Several technical features were used to examine the effects of various factors on the temperature, concentration, and velocity profiles. This study considered parameters like, the magnetic field , permeability , non-linear stretching sheet, Prandtl number, and the thermal radiation. The study also examines the graphical depictions of how the physical elements affect the skin-friction coefficients along the *x* and *y* - directions and heat transfer rate. This was done in tandem with the findings, which are shown graphically.

Keywords: Maxwell fluid; Magnetic field; Thermal radiation; Porous medium; Finite element metho

INTRODUCTION

Fluids play a critical role in numerous industrial processes, with non-Newtonian fluids exhibiting particularly unique rheological properties. Applications such as plastic sheet extrusion, paper manufacturing, metal spinning, and glass fiber production, exemplify the widespread use of these materials. Maxwell's model, a cornerstone of non-Newtonian fluid theory, provides a framework for predicting stress relaxation behavior in these complex systems. Furthermore, magnetohydrodynamics (MHD) elucidates the interaction between magnetic fields and electrically conductive fluids in motion. This interaction generates forces within the fluid, enabling novel control mechanisms and applications in various industrial settings.

Sandeep and Sulochana (2018) conducted a comprehensive investigation into the stretching surface flows of Oldroyd-B, Jeffrey, and Maxwell fluids, considering the effects of nonuniform heat source/sink perturbations and radiation. In a subsequent study, Farooq et al. (2019) delved into the exponentially expanding sheet flow of Maxwell-type nanomaterials. Wang et al. (2019) and Sun et al. (2019) developed a model for incompressible Maxwell fluid flow through a tube with a triangular cross section, which could be either rectangular or isosceles. The unsteady flow of viscoelastic fluid with a fractional Maxwell model in a channel, was investigated by Haitao and Mingyu (2007). Wenchang et al. (2003) utilized the fractional Maxwell model to investigate the unsteady flows of a viscoelastic fluid between two parallel plates. Qi and Liu (2011) explored analogue duct flows of a fractional Maxwell fluid. On the other hand, Saleem et al. (2017) examined the 3D mixed convective Maxwell fluid, using mass and heat Catteneo-Christov heat flow models, while considering heat production. Similarly, Fetecau and Fetecau (2003) discovered an exact numerical solution for fluid flow in Maxwell's law.

Apart from the above studies , the propagation of Maxwell fluid in a porous medium was studied by Wang and Hayat (2008) and the behaviour of fraction Maxwell fluid in unsteady flow was investigated by Fetecau et al. (2014). A two-dimensional magnetohydrodynamic (MHD) Maxwell fluid was also studied by Hayat et al. (2009). Similarly, Heyhat and Khabzi (2011) investigated the upper-convicted Maxwell (UCM) fluid flow across a flat rigid region in a magnetohydrodynamic (MHD) system and series solutions for two-dimensional magnetohydrodynamic circulation with thermophoresis and Joule heating, were obtained by Hayat and Qasim (2010). Similarly, Jamil and Fetecau (2010) studied Maxwell fluid in relation to helical flows between coaxial cylinders. Zheng et al. (2011) found exact mathematical solutions for a rotating flow model based on a generalized Maxwell fluid. To better understand how Maxwell fluid behaves in the presence of porous media, double-diffusive convection, and Soret effects, Wang and Tan (2011) also undertook a stability study. Sivaiah et al. (2012a,b,c) modeled and analyzed heat and mass transfer effects on unsteady MHD convection flow via finite element method. Motsa et al. (2012) examined the UCM flow in a porous structure. Reddy et al. (2012) too studied heat and mass transfer effects on unsteady MHD free convection flow past a vertical permeable moving plate with radiation. Further, the dynamics of thermally radiative Maxwell fluid flow over a continuously permeable expanding surface were characterized by Mukhopadhyay et al. (2013). Ramesh et al. (2017) too examined the Maxwell fluid with nanomaterials for magnetohydrodynamic (MHD) flow in a Riga plate computationally. In addition to above mentioned studies, Deepa and Murali. (2014) and Deepa and Gundagani (2014)

analyzed the viscous dissipation, soret and dufour effects on unsteady MHD flow using finite difference method.

In the realm of magnetohydrodynamic (MHD) driven systems, the finite element solutions found by Murali et al. (2023) and Murali and Babu (2023) represented a significant advancement. The comprehension of these solutions was greatly enriched by the foundational research of Babu et al. (2015, 2018), whose seminal works are meticulously cited throughout the literature. Besides, heat and mass transfer effects were studied by a large number of researchers like Singh et al. (2023), Gundagani et al. (2012, 2013a,b, 2024a,b), Tanuku et.al (2024), Gundagani and Babu (2012) and Murali et al. (2015a,b). The interplay of these scholarly contributions has undeniably propelled the field forward, offering a robust framework for future explorations and applications within the domain of MHD systems.

An analysis is presented here on the magnetohydrodynamic (MHD) flow of a non-Newtonian, non-viscous Maxwell fluid via a stretched surface in a porous medium, considering the influence of heat radiation. Non-linear ordinary differential equations are solved using the finite element treatment. The temperature, velocity (in the x and y-directions), and profiles are examined by the use of graphs derived from the solutions obtained by the finite element method. Data on the Skin-friction coefficients in the x and y directions, along with the local Nusselt number, are analyzed using tabular representations. The obtained findings show a high level of concordance with past data in comparison to currently available data.

MATHEMATICAL FORMULATION

In this section, the effects of thermal radiation and magnetic field on three-dimensional, steady, incompressible, viscous, non-Newtonian Maxwell fluid flow, past a stretching surface embedded in porous medium, has been dealt. The geometry of the fluid flow is shown in Figure 1. To undertake this inquiry, the following premises are assumed:

i. The magnetic Reynolds number is considered as low as possible to neglect the induced magnetic field.

ii. The velocities of the sheet along the x - and y - directions are assumed to be U_w (x) = ax and V_w (y) = by respectively.

iii. A magnetic field of strength B_o is applied to the flow.

iv. In energy equation, Ohmic heating, Thermophoresis, Brownian motion, Viscous dissipation, Diffusion thermo, Heat source and Joule heating effects are neglected.

v. Let T_w be the constant temperature at the sheet, whereas T_∞ denotes the fluid temperature outside the thermal boundary layer.

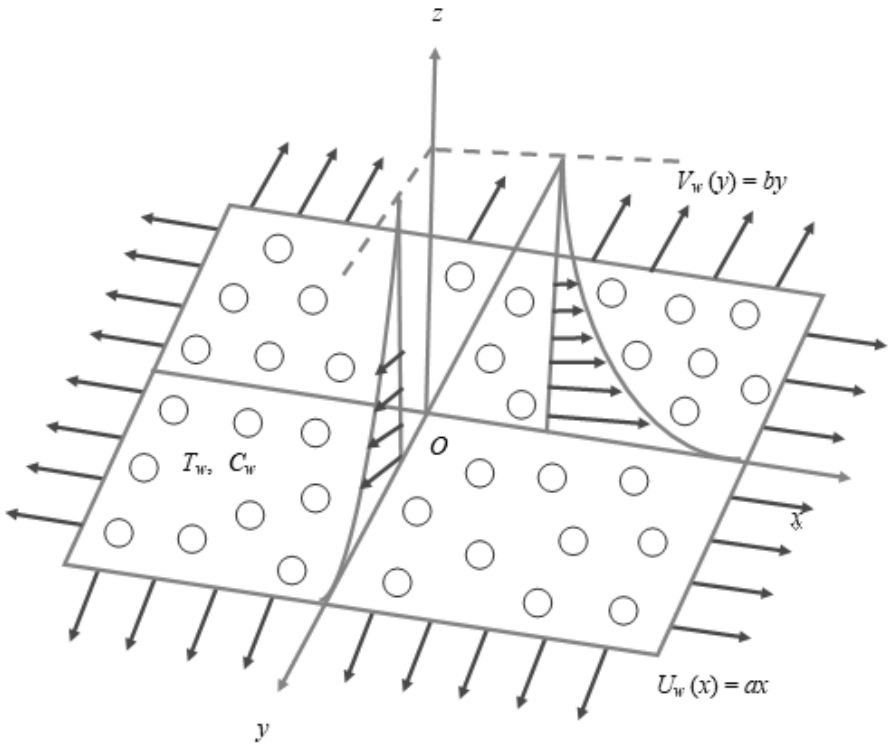

Figure 1. Geometrical representation of Maxwell fluid flow

Based on the above assumptions, the basic governing equations for Maxwell-Nanofluid flow are,

Continuity Equation:

$$\frac{\partial u}{\partial x}+\frac{\partial v}{\partial y}+\frac{\partial w}{\partial z}=0 \tag{1}$$

Momentum Equation:

$$u(u_x)+v(u_y)+w(u_z)+\lambda\left[u^2(u_{xx})+v^2(u_{yy})+w^2(u_{zz})+2uv(u_{xy})+2vw(u_{yz})+2uw(u_{xz})\right]=u_{zz}-(\frac{v}{k^*})u-[\frac{\sigma(B_o)^2}{\rho}]u \tag{2}$$

$$u(v_x)+v(v_y)+w(v_z)+\lambda\left[u^2(v_{xx})+v^2(u_{yy})+w^2(u_{zz})+2uv(v_{xy})+2vw(v_{yz})+2uw(v_{xz})\right]=v_{zz}-(\frac{v}{k})u-[\frac{\sigma(B_o)^2}{\rho}]v \tag{3}$$

Equation of thermal energy:

$$u\left(\frac{\partial T}{\partial x}\right)+v\left(\frac{\partial T}{\partial y}\right)+w\left(\frac{\partial T}{\partial z}\right)=\alpha\left(\frac{\partial^2 T}{\partial z^2}\right)-\frac{1}{\rho C_p}\left(\frac{\partial q_r}{\partial z}\right) \tag{4}$$

The boundary conditions for this flow are

$$u=U_w=ax,\ v=V_w=by,\ w=0,\ T=T_w\ at\ z=0\ \&\ u\to 0,\ v\to 0,\ T\to T_\infty\ as\ z\to\infty \tag{5}$$

The radiative heat flux q_r (using Roseland approximation) is defined as

$$q_r=-\frac{4\sigma^*}{3K^*}\left(\frac{\partial T^4}{\partial z}\right) \tag{6}$$

We assume that the temperature variances inside the flow are such that the term T^4 can be represented as linear function of temperature. This is accomplished by expanding T^4 in a Taylor series about a free

stream temperature T_∞ as follows:

$$T^4=T_\infty^4+4T_\infty^3\left(T-T_\infty\right)+6T_\infty^2\left(T-T_\infty\right)^2+..... \tag{7}$$

After neglecting higher-order terms in the above equation beyond the first-degree term in $\left(T-T_\infty\right)$, we get

$$T^4\cong 4T_\infty^3T-3T_\infty^4 \tag{8}$$

Thus substituting Eq. (8) in Eq. (6), we get

$$q_r=-\frac{16T_\infty^3\sigma^*}{3K^*}\left(\frac{\partial T}{\partial z}\right) \tag{9}$$

Using (9), Eq. (4) can be written as

$$u\left(\frac{\partial T}{\partial x}\right)+v\left(\frac{\partial T}{\partial y}\right)+w\left(\frac{\partial T}{\partial z}\right)=\alpha\left(\frac{\partial^2 T}{\partial z^2}\right)+\frac{1}{\rho C_p}\left(\frac{16T_\infty^3\sigma^*}{3\kappa k^*}\right)\left(\frac{\partial^2 T}{\partial z^2}\right) \tag{10}$$

Initiating the following similarity transformations

$$\eta=\left(\sqrt{\frac{a}{\nu}}\right)z,\ u=axf'(\eta),\ v=ayg'(\eta),\ \theta=\frac{T-T_\infty}{T_w-T_\infty},\ w=\nu\sqrt{\nu a}\left\{f(\eta)+g(\eta)\right\} \tag{11}$$

Making use of Eq. (11), equation of continuity (1) is identically satisfied and Eqs. (2), (3), and (10) take the following form

$$f'''-f'^2+ff''+gf''-Mf'+K\left\{2ff'f''+2gf'f''-(f+g)^2f'''\right\}-\delta f'=0 \tag{12}$$

$$g'''-g'^2+fg''+gg''-Mg'+K\left\{2fg'g''+2gg'g''-(f+g)^2g'''\right\}-\delta f'=0 \tag{13}$$

$$\left\{\frac{d}{d\eta}\left[\left(1+R\left(1+\left(\theta_w-1\right)\theta\right)^3\right)\theta'\right]\right\}+\Pr f\theta'+\Pr g\theta'=0 \tag{14}$$

the corresponding boundary conditions (5) becomes

$$f(0)=0,\ g(0)=0,\ f'(0)=1,\ g'(0)=C,\ \theta(0)=1,\ f'(\infty)\to 0,\ g'(\infty)\to 0,\ \theta(\infty)\to 0 \tag{15}$$

where the involved physical parameters are defined as

$$M=\frac{\sigma B_o^2}{\rho U_o},\ K=\lambda_1 a,\ C=\frac{b}{a},\ \theta_w=\frac{T_w}{T_\infty},\ \Pr=\frac{\nu}{\alpha},\ R=\frac{16\sigma^*T_\infty^3}{3\kappa k^*},\ \delta=\frac{\nu}{aK_o} \tag{16}$$

Quantities of physical interest, the physical parameters of the skin-friction coefficient along *x* and *y* - directions, local Nusselt number are presented as follows:

$$C_{fx}=\frac{\tau_{wx}}{\rho U_w^2}=\frac{1}{\rho U_w^2}\mu\left(\frac{\partial u}{\partial y}\right)_{y=0}\Rightarrow Cfx=C_{fx}\left(\sqrt{\mathrm{Re}_x}\right)=f''(0) \tag{17}$$

$$C_{fy}=\frac{\tau_{wy}}{\rho V_w^2}=\frac{\mu}{\rho V_w^2}\left(\frac{\partial v}{\partial y}\right)_{y=0}\Rightarrow Cfy=C_{fy}\left(\sqrt{\mathrm{Re}_y}\right)=g''(0) \tag{18}$$

$$Nu=\frac{xq_w}{\kappa\left(T_w-T_\infty\right)}=-\frac{x\left(\frac{\partial T}{\partial y}+\frac{\partial q_r}{\partial y}\right)_{y=0}}{\kappa\left(T_w-T_\infty\right)}\Rightarrow Nu=-\left(1+R\theta_w^3\right)\left(\sqrt{\mathrm{Re}_x}\right)\theta'(0) \tag{19}$$

Where $\mathrm{Re}_x=\frac{U_w x}{\nu}$ is local Reynolds number based on the stretching velocity U_w (*x*) and $\mathrm{Re}_y=\frac{V_w y}{\nu}$ is local Reynolds number based on the stretching velocity V_w(*y*).

METHOD OF SOLUTION

Numerous numerical techniques, including as the LU decomposition approach, the Gauss elimination method, and others, can be used to solve built equations. It is crucial to keep in mind the form functions used to approximately approximate real functions while working with real numbers. The flow domain is made up of 10,000 identically sized quadratic components and a total of 20,001 nodes. 10,000 quadratic components of identical size make up the flow domain. We were given 80,04 nonlinear equations to

research after constructing the fundamental equations. The remaining system of nonlinear equations is then numerically solved with a precision of 0.00001 using the Gauss elimination method, once the boundary conditions have been applied. The use of Gaussian quadrature makes integrates solutions easier. The method's computer software was written in the MATHEMATICA programming language and executed on a desktop machine.

PROGRAM CODE VALIDATION

The validation of present numerical results is compared with the published results of Mushtaq et al. (2016) in Table 1 in absence of magnetic field and porous medium effects for various values of C at Pr = 1.0. From this table, it is observed that, the present results are in very good agreement with their results.

RESULTS AND DISCUSSION

In the previous section, the set of ordinary differential equations (12), (13) and (14) are solved using the finite element method with the help of boundary equations (12). In this section, we demonstrate the effects of various parameters such as M = 0.5, K = 0.5, C = 0.5, Pr = 0.22, R= 0.5, and δ = 0.1, θ_w = 0.5 on velocity (velocity components along the x - and y - axes) and temperature profiles (Figures 2-12). Also, the numerical values of Skin-friction coefficients along x - and y - axes and rate of heat transfer coefficient with the same parameter variations are discussed in Tables 2, 3 and 4 respectively.

Figures 2 and 3 show the effect of magnetic field parameter (M) on velocity profiles along x - and y - directions respectively. It has been shown that the velocity fields diminish as the value of M rises. The fluid flow tends to slow down in the presence of a magnetic field. The influence of Maxwell fluid parameter or Deborah number (K) on the x - and y - components of velocity is sketched in the Figures 4 and 5 respectively. The fluid's relaxation period's deviation from its basic time scale is quantified by the Deborah number. The relaxation period is the amount of time the fluid requires to reach equilibrium following the application of the shear force. It is anticipated that fluids with a higher viscosity may take longer to relax.

Table 1. Validation of present numerical results with the published results of Mushtaq et al. (2016) for different values of C at Pr = 1.0 when M = 0, and δ = 0.

C	Present numerical results			Obtained by Mushtaq et al. (2016)		
	$-f''(0)$	$-g''(0)$	$-\theta'(0)$	$-f''(0)$	$-g''(0)$	$-\theta'(0)$
0.25	1.0256378487	0.1181027022	0.6515670171	1.048811	0.194564	0.665926
0.50	1.0859659654	0.4526534797	0.7234146547	1.093095	0.465205	0.735333
0.75	1.1287554899	0.7865763453	0.7753675487	1.134486	0.794618	0.796472
1.00	1.1645765434	1.1609873546	0.8409867124	1.173721	1.173721	0.851992

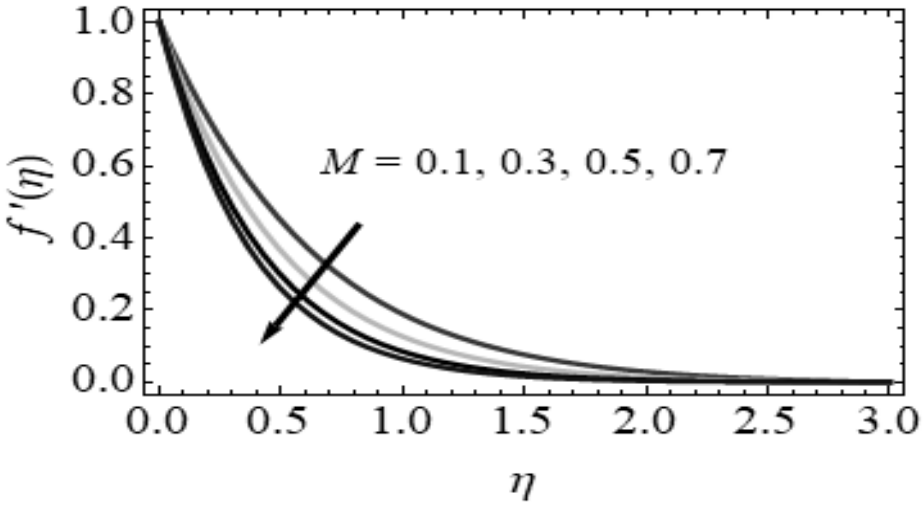

Figure 2. Primary velocity profiles (f') for different values of Magnetic field parameter (M)

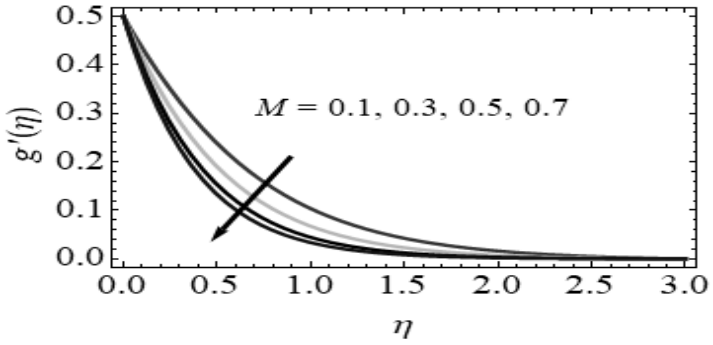

Figure 3. Secondary velocity profiles (g') for different values of Magnetic field parameter (M)

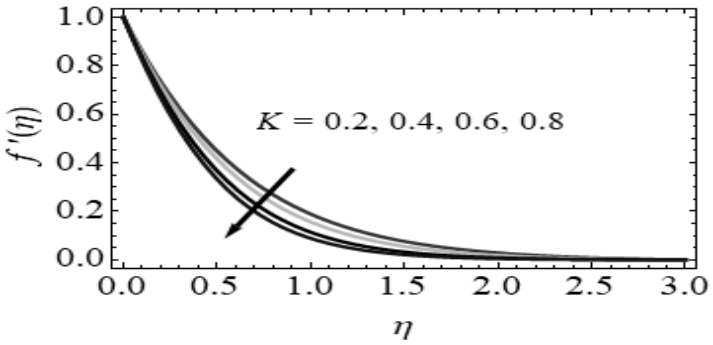

Figure 4. Primary velocity profiles (f') for different values of Maxwell fluid parameter (K)

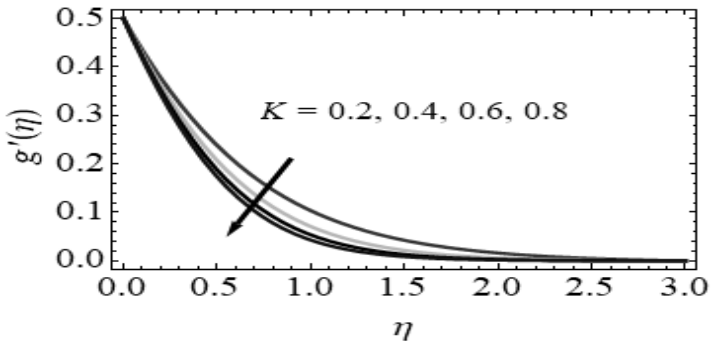

Figure 5. Secondary velocity profiles(g') for different values of Maxwell fluid parameter (K)

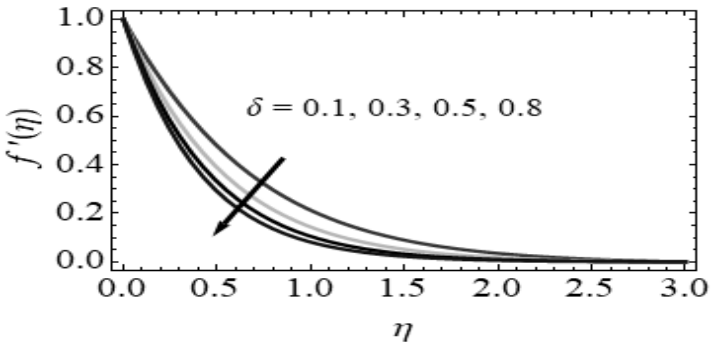

Figure 6. Primary velocity profiles (f') for different values of permeability parameter (δ)

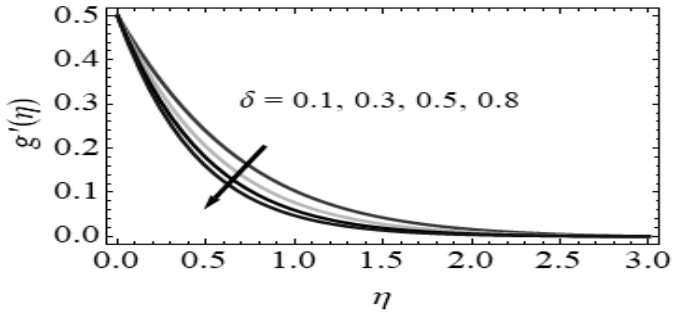

Figure 7. Secondary velocity profiles(g') for different values of permeability parameter (δ)

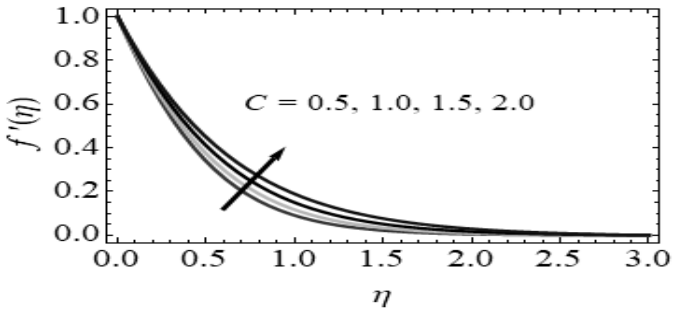

Figure 8. Primary velocity Profiles **(***f ′)* for different values of velocity ratio parameter (C)

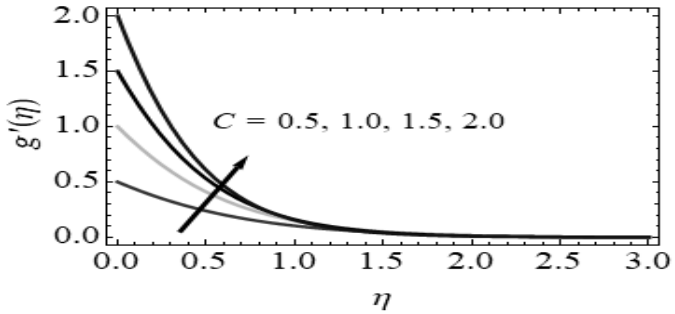

Figure 9. Secondary velocity profiles(g') for different values of velocity ratio parameter (C)

It is possible to interpret an increase in *K* in this way because fluid viscosity restricts fluid motion and lowers velocity. As a result, the hydrodynamic boundary layer thins when *K* is increased. It is also noted that change in the velocity fields f' and g' is larger in the three-dimensional flow when compared with the two-dimensional and axi-symmetric flows. Figures 6 and 7 illustrate the effect of permeability parameter (δ) on the velocity distributions along x - and y - directions respectively. From these figures, it is observed that the velocity profiles decreases with the increase in permeability (porosity) parameter *K*. This arises because an increase in *K* amplifies the porous layer and thereby reduces the thickness of momentum boundary layer.

Figures 8 and 9 show the behaviour of velocity ratio parameter (*C*) on primary and secondary velocity profiles respectively. From these figures, it is observed that, both the primary and secondary velocity profiles increase with rising values of velocity ratio parameter. The variation of Prandtl number on temperature outlines is shown in Figure 10. It is concluded that increasing values of Prandtl number result in a thinner temperature boundary layer thickness. Fluids having larger Prandtl number have lower thermal diffusivity, and hence the temperature decreases. Figure 11 shows the variation that are seen in temperature profiles due to increase in the values of (*R*). Because the conduction effect of the nanofluid increases in the presence of *R*, it is noticed that the fluid temperature rises as *R* increases. Higher values of *R* thus imply higher surface heat flow, which raises the temperature in the boundary layer area.

Figure 12 includes the behaviour of temperature ratio parameter θ_w on the temperature distribution. Bigger values of θ_w corresponds to a larger temperature and thicker thermal boundary layer.

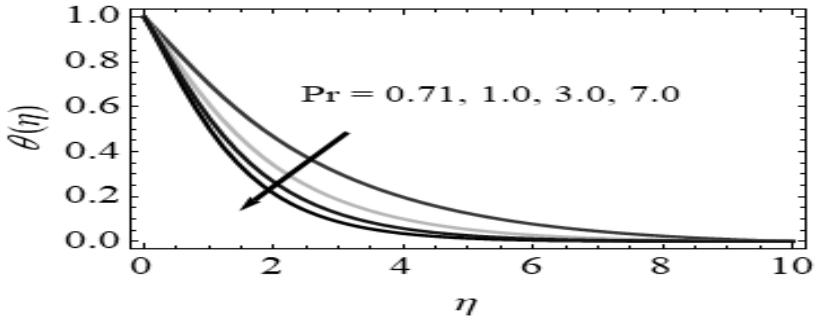

Figure 10. Temperature profiles for different values of Prandtl number (Pr)

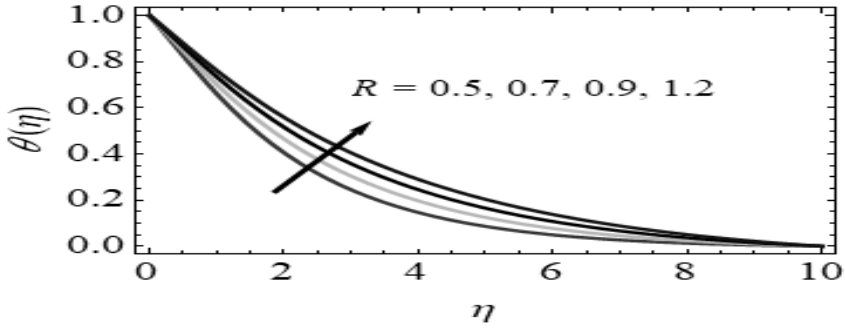

Figure 11. Temperature profiles for different values of thermal radiation parameter (*R)*

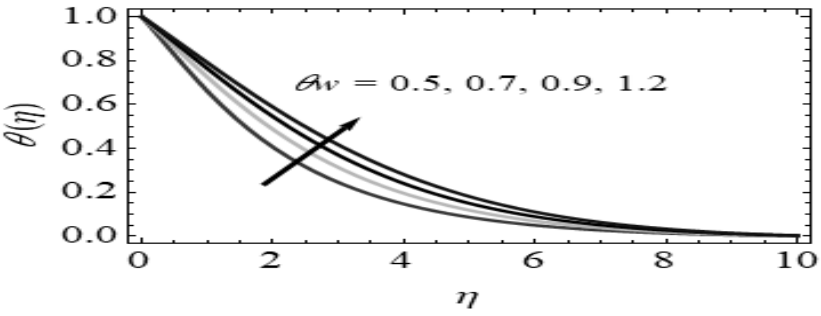

Figure 12. Temperature profiles for different values of temperature ratio parameter(*θw)*

This is explained as follows. It is clear from energy Eq. (14) that effective thermal diffusivity is the sum of classical thermal diffusivity (α) and thermal diffusivity due to the radiation effect. Thus one anticipates that parameter θ_w, being the coefficient of the later term, would support the thermal boundary layer thickness. It can be further noticed that the profiles attain special *S*-shaped form when θ_w enlarges, which dictates the existence of adiabatic case. In other words, the wall temperature gradient approaches zero value when wall to ambient temperature ratio is sufficiently large.

The numerical values of various parameters namely, *M*, *K*, *C*, δ, Pr, *R*, θ_w on Skin-friction coefficients along *x* - (*Cfx*) and *y* - (*Cfy*) directions are discussed in Tables 2 and 3 respectively. From these tables, it is observed that, the Skin-friction coefficients along *x* - (*Cfx*) and *y* - (*Cfy*) directions are increasing with increasing values of *C*, *R*, θ_w and is decreasing with increasing values of *M*, *K*, and Pr. From these tables, it is observed that, the Skin-friction coefficients along *x* - (*Cfx*) and *y* - (*Cfy*) directions are increasing with increasing values of *C*, *R*, θ_w and is decreasing with increasing values of *M*, *K*, and Pr. The tabular values of rate of heat transfer coefficient or Nusselt number (*Nu*) for different values of Pr, *R*, and θ_w are shown in Table 4. From this table, it is observed that, the rate of heat transfer coefficient is increasing with rising values of *R*, θ_w, and opposite effect is observed with the effect of Pr.

Table 2. Results of Skin-friction coefficient along *x*-direction

M	*K*	δ	*C*	Pr	*R*	θ_w	*Cfx*
0.1	0.2	0.1	0.5	0.71	0.5	0.5	3.5667620975
0.3							3.5014748743
0.5							3.4867190992
	0.4						3.5153646203
	0.6						3.4714674308
		0.3					3.5125675082
		0.5					3.4956748481
			1.0				3.5966573450
			1.5				3.6145780621
				1.00			3.5045465823
				3.00			3.4714665621
					0.7		3.5856187502
					0.9		3.6064720278
						0.7	3.5856586580
						0.9	3.6036465591

Table 3. Results of Skin-friction coefficient along *y*-direction

M	*K*	δ	*C*	Pr	*R*	θ_w	*Cfy*
0.1	0.2	0.1	0.5	0.71	0.5	0.5	2.7590650945
0.3							2.7254704872
0.5							2.6947557921
	0.4						2.7215627057
	0.6						2.6945469252
		0.3					2.7105657871
		0.5					2.6845586825
			1.0				2.7857501722
			1.5				2.8045252876
				1.00			2.7156706702
				3.00			2.6835456924
					0.7		2.7845645923
					0.9		2.8056756108
						0.7	2.7756701011
						0.9	2.7956750572

Table 4. Rate of heat transfer coefficient results

Pr	*R*	θ_w	*Nu*
0.71	0.5	0.5	1.8548832158
1.00			1.8113760176
3.00			1.7859060651
	0.7		1.8838604560
	0.9		1.9075789431
		0.7	1.8945457965
		0.9	1.9036460934

The tabular values of rate of heat transfer coefficient or Nusselt number (*Nu*) for different values of Pr, *R*, and θ_w are shown in Table 4. From this table, it is observed that, the rate of heat transfer coefficient is increasing with rising values of *R*, θ_w, and opposite effect is observed with the effect of Pr.

CONCLUSIONS

The present study investigates the combined impact of heat radiation and magnetic field on a stable, two-dimensional, incompressible, viscous, non-Newtonian Maxwell fluid flowing towards a stretched sheet in the presence of a

porous material. The fundamental partial differential equations are used to represent the present problem prior to their transformation into ordinary differential equations. Next, the finite element approach is used to numerically solve these equations. Hence, it is feasible to analyze and communicate the velocity and temperature patterns graphically. Key aspects of this effort are:

i. The velocity profiles along x - and y - directions decrease with increasing values of Maxwell fluid parameter, magnetic field parameter, permeability parameter, and the reverse effect is observed in the case of velocity ratio parameter.
ii. The temperature profiles show increasing trend with increasing values of thermal radiation parameter, and temperature ratio parameter while reverse effect is observed in the case of Prandtl number.
iii. Finally, the present numerical results are very good agreement with the published results of Mushtaq et al. (2016).

List of Symbols:

u, v, w : Velocity components in x, y and $z$axes respectively (m/s)
x, y, z : Cartesian coordinates measured along the stretching sheet (m)
f : Dimensionless stream function along x - direction ($kg / m.\ s$)
f' : Fluid velocity along x - direction(m/s)
K_o: Dimensional Permeability parameter
g : Dimensionless stream function along y - direction ($kg / m.\ s$)
g' : Fluid velocity along y - direction(m/s)
Pr: Prandtl number
T: Fluid temperature (K)
T_∞ : Temperature of the fluid far away from the stretching sheet (K)
Cf_x : Skin-friction coefficient along x - direction (s^{-1})
Cfx : Non-dimensional skin-friction coefficient along x - direction (s^{-1})
M : Magnetic field parameter
B_o : Uniform magnetic field (*Tesla*)
a, b : Constants
T_w : Temperature at the surface (K)
O : Origin
K : Maxwell fluid parameter
R : Thermal radiation parameter
q_r : Radiative heat flux
Cf_y : Skin-friction coefficient along y - direction (s^{-1})
Cfy : Non-dimensionalSkin-friction coefficient along y - direction (s^{-1})
$U_w(x)$: Stretching velocity of the fluid along x - direction (m/s)
$V_w(y)$: Stretching velocity of the fluid along y - direction (m/s)
q_w : Heat flux coefficient
Nu : Rate of heat transfer coefficient (or) Nusselt number
C_p : Specific heat capacity of nano particles ($J / kg / K$)
C : Stretching sheet parameter
Re_x : Reynolds number along x - direction
Re_y : Reynolds number along y - direction
K^* : Mean absorption coefficient

Greek symbols:

η : Dimensionless similarity variable (m)
θ : Dimensionless temperature (K)
ν : Kinematic viscosity (m^2 / s)
σ : Electrical Conductivity
ρ : Fluid density (kg / m^3)
κ : Thermal conductivity of the fluid
τ_{wx} : Wall shear stress along x - direction
τ_{wy} : Wall shear stress along y - direction
δ : Permeability parameter
α : Thermal diffusivity, (m^2 / s)
θ_w : Temperature ratio parameter
σ^* : Stefan-Boltzmann constant
λ : The fluid relaxation time
μ : Dynamic viscosity of the fluid
ρ_f : Density of the fluid (kg / m^3)

Superscript:

$'$: Differentiation w.r.t η

Subscripts:

f : Fluid
w : Condition on the sheet
∞ : Ambient Conditions

ACKNOWLEDGMENTS

The authors express their gratitude to Dr. O. P. Pandey, the Chief Editor, for his insightful feedback and for editing the final manuscript. The authors are also thankful to reviewers for their comments and suggestions. No funding was received

Author Credit Statement

All authors have contributed equally. All authors have read and approved the manuscript

Data availability

On reasonable request, the datasets used and/or analyzed during the current investigation are accessible from the corresponding author, and all data created or analyzed during this study are included in this published publication.

Compliance with ethical standards

Declare no conflict of interest and adhere to copyright norms

REFERENCES

Babu, N.V.N., Gundagani, M. and Paul, A., 2015. Soret and Dufour effects on unsteady hydromagnetic free convective fluid flow past an infinite vertical porous plate in the presence of chemical reaction. J. Science and Arts, 15 (1), 99-111

Babu, N.V.N., Murali, G., Bhati, S.M., 2018. Casson fluid performance on natural convective dissipative couette flow past an infinite vertically inclined plate filled in porous medium with heat transfer, MHD and hall current effects. In. J. Pharmaceutical Res., 10(4), 809-819.

Deepa, G. and Murali, G., 2014. Effects of viscous dissipation on unsteady MHD free convective flow with thermophoresis past a radiate inclined permeable plate. Iranian J. Sci. Technology (Sciences), 38A3, DOI: 10.22099/IJSTS.2014.2437.

Deepa, G. and Gundagani, M., 2014.Analysis of soret and dufour effects on unsteady MHD flow past a semi infinite vertical porous plate via finite difference method. Int. J. Appl. phys. and math., 4(5), 332-344, DOI: 10.7763/IJAPM.2014.V4.306.

Farooq, U., Lu, D., Munir, S., Ramzan, M., Suleman, M. and Hussain, S., 2019. MHD flow of Maxwell fluid with nanomaterials due to an exponentially stretching surface, Scientific Reports. 9, 7312, doi: 10.1038/s41598-019-43549-0

Fetecau C. and Fetecau, C., 2003. A new exact solution for the flow of Maxwell fluid past an infinite plate. Int. J. Nonlin. Mech. 38(3), 423-427.

Fetecau, C., Athar, M. and Fetecau, C., 2014. Unsteady flow of a generalized Maxwell fluid with fractional derivative due to a constantly accelerating plate. Comput. Math. Appl. 57(4), 596-603.

Gundagani, M. and Babu, N.V.N., 2012. Effect of Radiation on MHD Convection Flow Past a Vertical Permeable Moving Plate**.** Int. J. Advances in Appl. Sci., (IJAAS)**,**1(1), 19-28.

Gundagani, M., Sivaiah, S., Babu, NVN. and Reddy, M.C.K. 2012. Finite element solution of thermal radiation effect on unsteady MHD flow past a vertical porous plate with variable suction. Int. J. Engineering & Techn., 1(3), DOI:10.14419/ijet.v1i3.52.

Gundagani, M, Sheri, S., Paul, A. and Reddy, M. C. K., 2013a. Unsteady magnetohydrodynamic free convective flow past a vertical porous plate, Int. J .Appl. Sci. and Engineering, 11 (3), 267–275

Gundagani, M., Sheri, S., Paul, A. and Reddy, M. C. K., 2013b. Radiation Effects on an Unsteady MHD Convective Flow Past a Semi-Infinite Vertical Permeable Moving Plate Embedded in a Porous Medium with Viscous Dissipation. Walailak J. Sci & Tech., 10(5), 499–515. DOI- 10.2004/wjst.v10i5.380

Gundagani, M., Babu, N.V.N., Gadially, D. et al., 2024a. Study of Nano-Powell-Erying fluid flow past a porous stretching sheet by the effects of MHD, thermal and mass convective boundary conditions. J. Umm Al-Qura Univ. Eng. Archit.,15, 271-281. https://doi.org/10.1007/s43995-024-00056-2,

Gundagani, M., Mamidi, L.P. and Tanuku, P.K., 2024b. Finite element solutions of Double diffusion effects on three-dimensional MHD Nano-Powell-Erying fluid flow in presence of thermal and mass Biot numbers. J. Eng. Appl. Sci., 71, Article 9 . https://doi.org/10.1186/s44147-023-00347-w

Haitao, Q. and Mingyu, X., 2007. Unsteady flow of viscoelastic fluid with fractional Maxwell model in a channel. Mechanics Res. Comm., 34(2), 210-212, https://doi.org/10.1016/j.mechrescom.2006.09.003.

Hayat, T. and Qasim, M., 2010. Influence of thermal radiation and Joule heating on MHD flow of a Maxwell fluid in the presence of thermophoresis. Int. J. Heat. Mass. Tran., 53 (21-22), 4780-4788.

Hayat, T., Abbas, Z. and Sajid, M., 2009. MHD stagnation point flow of an upper-convected Maxwell fluid over a stretching surface. Chaos. Soliton. Fract., 39(2), 840-849.

Heyhyat, M. M. and Khabazi, N., 2011. Non-isothermal flow of Maxwell fluids above fixed flat plates under the influence of a transverse magnetic field. Proc. Institution of Mechanical Engineers, Part C: J. Mech. Eng. Sci., 225, 909-916. doi:10.1243/09544062JMES2245.

Jamil, M. and Fetecau, C., 2010. Helical flows of Maxwell fluid between coaxial cylinders with given shear stresses on the boundary. Nonlin. Analy: Real. World. App. 11(5), 4302-4311.

Motsa, S. S., Hayat, T. and Aldossary, O. M., 2012. MHD flow of upper-convected Maxwell fluid over porous stretching sheet using successive Taylor series linearization method. J. Appl. Math. Mech., 33(8), 975-990.

Mukhopadhyay, S., De, P.R. and Layek, G.C., 2013. Heat transfer characteristics for the Maxwell fluid flow past an unsteady stretching permeable surface embedded in a porous medium with thermal radiation. J. Appl. Mech and Technical Phys. 54(3), 385-396.

Murali, G. and Babu, N.V.N., 2023. Convective MHD Jeffrey Fluid Flow Due to Vertical Plates with Pulsed Fluid Suction: A Numerical Study. J. Computational Appl. Mechanics, 54 (1), 36-48, DOI: 10.22059/ JCAMECH.2023.351326.773

Murali, G., Paul, A., and Babu, N.V.N., 2015a. Heat and mass transfer effects on an unsteady hydromagnetic free convective flow over an infinite vertical plate embedded in a porous medium with heat absorption. Int. J. Open Problems Compt. Math, 8 (1), 15-27.

Murali, G., Paul, A. and Babu, N.V.N., 2015b. Numerical study of chemical reaction effects on unsteady MHD fluid flow past an infinite vertical plate embedded in a porous medium with variable suction. Electronic J. mathematical analysis and appl.,3(2), 179-192,2015.

Murali, G., Deepa, G., Nirmala Kasturi, V. and Poornakantha, T., 2023. Joint effects of thermal diffusion and diffusion thermo on MHD three dimensional nanofluid flow towards a stretching sheet. Mathematical models in engineering, DOI: https://doi.org/10.21595/mme.2023.23590.

Mushtaq, A., Mustafa, M., Hayat, T. and Alsaedi, A., 2016. A numerical study for three-dimensional viscoelastic flow inspired by non-linear radiative heat flux. Int. J. Non-Linear Mechanics, 79, 83-87.

Qi, H. T. and Liu, J. G., 2011. Some duct flows of a fractional Maxwell fluid. The European Physical J. Special Topics, 193(1), 71-79, https://doi.org/10.1140/epjst/e2011-01382-6, 2-s2.0-79953717430.

Ramesh, G. K., Roopa, G. S., Gireesha, B. J., Shehzad, S. A. and Abbasi, F. M., 2017. An electro-magneto-hydrodynamic flow Maxwell nanoliquid past a Riga plate: a numerical study. J. Braz. Soc. Mech. Sci. Eng., 39, 4547-4554.

Reddy, M.K., Murali, G., Sivaiah, S. and Babu, N.V.N., 2012. Heat and mass transfer effects on unsteady MHD free convection flow past a vertical permeable moving plate with radiation. Int. J. Appl. Mathematical Res., 1 (2), 189-205. DOI:10.14419/ijamr.v1i2.45

Saleem, S., Awais, M., Nadeem, S., Sandeep N. and Mustafa, M. T., 2017.Theoretical analysis of upper-convected Maxwell fluid flow with Cattaneo-Christov heat flux model. Chinese J. Physics. https://doi.org/10.1016/j.cjph.2017.04.005.

Sandeep N. and Sulochana C., 2018. Momentum and heat transfer behaviour of Jeffrey, Maxwell and Oldroyd-B nanofluids past a stretching surface with non-uniform heat source/sink. Ain Shams Engineering J., 9(4), 517-524, https://doi.org/10.1016/j.asej.2016.02.008.

Singh, N., Kaur, J., Thakur, P., Murali, G., 2023. Structural behaviour of annular isotropic disk made of steel/copper material with gradually varying thickness subjected to internal pressure. Structural integrity and life, 23 (3), 293–297.

Sivaiah, S., Gundagani, M. and Karanamu, M. P., 2012a. Analysis of Heat and Mass Transfer Effects on an Isothermal Vertical Oscillating Plate. Walailak J. Sci. Tech., (WJST), 9(4), 407–415.

Sivaiah, S., Murali, G. and Reddy, M.C.K., 2012b. Finite Element Analysis of Chemical Reaction and Radiation Effects on Isothermal Vertical Oscillating Plate with Variable Mass Diffusion. Int. Scholarly Res. Network ISRN Mathematical Physics, Vol. 2012, Article ID 401515, doi:10.5402/2012/401515.

Sivaiah, S. , Muraligoud, G., Murali, G. and Reddy, M.C.K. ,2012c. Unsteady MHD mixed convection flow past a vertical porous plate in presence of radiation. Int. J. Basic and App. Sc., 1(4), 651-666, DOI:10.14419/ijbas.v1i4.106.

Sun, X., Wang, S. and Zhao, M., 2019. Oscillatory flow of Maxwell fluid in a tube of isosceles right triangular cross section. Phys. of Fluids, 31, 123101, https://doi.org/10.1063/1.5128764.

Tanuku, P. K. ., Mamidi, L. P. and Gundagani, M., 2024. Modelling and analysis of three-dimensional chemically reacting, radiating Casson-nanofluid flow: thermophoresis and Brownian motion effects. Acta Polytechnica, 64(5), 455–463. https://doi.org/10.14311/AP.2024.64.0455

Wang, Y. and Hayat, T., 2008. Fluctuating flow of Maxwell fluid past a porous plate with variable suction. Nonlin. Analysis: Real. World. Appl., 9(4), 1269-1268.

Wang, S. and Tan, W. C., 2011. Stability analysis of soret driven double-diffusive convection of Maxwell fluid in a porous medium. Int. J. Heat and Fluid flow, 32(1), 88-94.

Wang S., Li P. and Zhao M., 2019. Analytical study of oscillatory flow of Maxwell fluid through a rectangular tube, Phys. Fluids, 31, 063102, https://doi.org/10.1063/1.5100220.

Wenchang, T., Wenxiao, P. and Mingyu, X., 2003. A note on unsteady flows of a viscoelastic fluid with the fractional Maxwell model between two parallel plates. Int. J. Non-linear Mechanics,38(5), 645-650, https://doi.org/10.1016/s0020-7462(01)00121-4.

Zheng, L., Li, C., Zhang, X. and Gao, Y., 2011. Exact solutions for the unsteady rotating flows of a generalized Maxwell coaxial cylinders. Comput. Math. Appl., 62, 1105-1115

.

Received on: 12-05-2024; Revised on: 14-01-2025 ; Accepted on: 15-01-2025

J. Ind. Geophys. Union, 29(1) (2025), 56-63
https://doi.org/10.71122/JIGU.29(1)2025.006

Kinematics of the Capricorn microplate and its surrounding regions as inferred from the analyses of GPS data

A.Akilan*[1], K. K. Abdul Azeez[1], Sravan K. Kotluri[2], H.V.S. Satyanarayana[1], S. Padhy[3] and O.P. Pandey[1]
[1]CSIR-National Geophysical Research Institute, Uppal Road, Hyderabad- 500 007, India
[2]National Centre for Earth Science Studies, Triuvanthapuram-695011, India
[3]Department of Earth Sciences, Indian Institute of Technology, Roorkee-247667, India
*Corresponding author: akilan@ngri.res.in

ABSTRACT

The Capricorn microplate, located between the Indian and Australian Plates, is a prominent tectonic block introduced between the two plates, primarily to explain the inconsistency observed in the Indian oceanic plate motions and the prevailing intraplate seismicity. We evaluated the kinematics of this microplate, relative to adjacently located other tectonic plates using GPS data to understand the underlying plate tectonic processes and associated deformation/strain patterns. The lengths of baseline are computed from the DGAR GPS site, placed at the northern fringe of the Capricorn Plate, and adjacently positioned other GPS sites in different geotectonic blocks. The estimated baseline lengths indicate a relative convergent tectonics between Capricorn microplate and southern tip of India with a rate of 1 mm/yr. In comparison, a much higher rate of convergence (about 18 mm/yr) is seen between the Capricorn microplate and the Sunda Plates. Such a high rate of convergence, if persists, would considerably shrink the wide diffusive boundary that currently exists between the Capricorn microplate and the Sunda blocks. Similarly, the baseline length changes between Capricorn microplate and Australia, indicate a shortening at a rate of about 10 mm/yr, which is in good agreement with earlier findings with a diffusive convergent boundary inferred between Capricorn microplate and Australia. A complex rate of change in baseline length is also noticed between this plate and the two different sites inside the African Plate. The DGAR-ZAMB station pair shows divergence between the two plates at a rate of 9 mm/yr, while the DGAR-SUTH (southern margin of Africa) pair shows convergence at a rate of ~4 mm/yr. The observed divergence between the Capricorn and Rovuma microplates, can be explained by the presence of Comores hotspot in the Somalian Plate, which is centered between north Madagascar and Rovuma microplate. This feature causes deformation due to magmatic extrusion led internal rifting (or spreading) below the Comores Islands and its surrounding regions. Consequently, a broad deformation zone is being formed east to the Rovuma microplate due to internal rifting of the Somalian Plate that includes the northern part of Madagascar and northernmost part of the Lwandle Plate.

Key word: Capricorn microplate kinematics, Madagascar, Indian Ocean, GPS, intraplate seismicity, Deformation zone

INTRODUCTION

During the process of plate-tectonics, movement of rigid lithosphere over the ductile asthenosphere may undergo convergence, divergence and/or strike-slip motion. The relative motion between the major tectonic plates, associated with the underlying plate tectonic processes, is the mechanism for the generation of different geological features as well as land forms (mountains and basins, ocean ridges and trenches). Thus, it acts as the primary driving force for natural disasters like earthquakes and volcanic activities (Wilson and Burke, 1972; Chapple and Forsyth, 1979; Sinton and Detrich., 1992). Interestingly, several studies have indicated the presence of microplates within the major tectonic plates that act as a separate entity and show different kinematics than the major lithospheric plates over which they are located (Bird and Naar, 1994; Koehn et al., 2008). Therefore, it is necessary to study the nature and amount of relative motion between different lithospheric plates for better understanding of the various active tectonic processes and associated deformation.

The Global Positioning System (GPS) technology is one of the effective methodologies to study the deformation and movement occurring at any point on the surface of the earth by evaluating the kinematics of the lithospheric plates (Dixon et al., 1991; Larson and Agnew, 1991; Bevis et al., 1995; Bouin and Vigny, 2000; Sella et al., 2002; Vigny et al., 2005; DeMets et al., 2010; Akilan et al., 2016). The Indian Ocean being the third largest among the oceans, has several neighborhood continental regions, which are associated with diverse plate tectonic processes that govern the geodynamic events occurring in the eastern hemisphere (Schlich, 1982). This region is characterized by many geotectonic features, for example, prominent ridges and triple junctions where three plate boundaries meet. The Indian and Australian Plates have long been referred to as one Indo-Australian Plate. The trio of Indo-Australia, Antarctica and Somalia Plates, meets at the Rodrigues triple junction in the Indian Ocean (Royer and Gorden, 1997). The plate motions in the Indian Ocean do not define the rigidity of the Indo-Australian Plate, suggesting major deformation zones that divide the plate into different blocks (Minster and Jordan, 1978; Stein and Gorden, 1984; Royer and Change, 1991; Royer and Gorden, 1997; Conder and Forsyth, 2001). The distribution of strong earthquakes and the currently available GPS data indicate the presence of three active plates in the region: Indian, Australian and Capricorn microplate, which are moving relative to each other independently and have large regions of diffused boundaries.

The Capricorn microplate located between the Indian and Australian Plates, was basically proposed by Royer and

Gorden (1997) to explain the observed high intraplate seismicity and also to explain the inconsistency found in the plate kinematic models defined using spreading rates, transform fault azimuths, and earthquake slip vectors (Conder and Forsyth, 2001). Nevertheless, plate geometries and kinematics of the Indian Ocean are not tightly constrained in the context of global tectonics. In the present study, the relative motion of the Capricorn microplate within the Indian Ocean is derived using GPS data to understand the plate tectonic processes and deformation/strain pattern surrounding this region.

GEOLOGIC EVOLUTION OF INDIAN OCEAN

The Indian Ocean was created consequent to Gondwana supercontinent breakup that gave rise to the continental segments like Africa, India, Australia, and Antarctica (Reeves and de Wit, 2000; Conder and Forsyth., 2001; Chatterji et al., 2013). The Indian Ocean presently carries two hotspot tracks, Rajmahal–Kerguelen track in the eastern part of the Indian Plate and the Deccan–Reunion and Marian plume in the western part (Chatterji et al., 2013). These hotspot trails are seen in the form of two linear underwater ridges, the Ninety East Ridge and the Chagos–Laccadive Ridge lying on either sides of the Indian Plate. Apart from these, 90 Ma Marion plume, which led to the breakup of Madagascar from the Indian subcontinent was also located close to the west coast of India (Curray and Munasinghe, 1991; Agrawal et al., 1992). The series of islands and seamounts was formed because of the fast northward movement of India during the Cretaceous-Tertiary period over the Kerguelen and Reunion mantle plumes (Duncan and Pyle, 1988; Chatterji et al., 2013). The Ninety East Ridge resulted from the interaction of the Kerguelen plume within the Indian Plate, while the Chagos–Laccadive Ridge resulted from the interaction of the Reunion plume with the Indian Plate. In addition to the general seismicity seen along the ridge axes, notable seismic events occur at the Chagos Bank that lies in the extensional regime between the Indian and Capricorn microplate and located close to the east of Central Indian Ridge axis (Tinnon and Holt., 1995; Radha Krishna et al., 1998; Henstock and Minshull, 2004; Royer et al., 2015). The seismicity in the Chagos Bank is limited to a region of 100 km in north-south extent, which coincides with a deep trough cutting east-west across the bank (Henstock and Minshull., 2004; Royer et al., 2015 and references therein). The Diego-Garcia Island in the Chagos part of the Chagos–Laccadive Ridge, is located to the south of the Chagos bank and characterized by seismic swarm activity. Diego Garcia Island represents the northern edge of the Capricorn microplate.

Regional tectonics and plate boundary features

The Indian Ocean consists of several seismic and aseismic mid-ocean ridges, transform faults, subduction zones and diffused deformation zones (**Figure 1**). Morphologically, it is dominated by four active mid-ocean ridges that include the north-west oriented Carlsberg Ridge (CR), north-south oriented Central Indian Ridge (CIR), Southwest Indian Ridge (SWIR) and Southeast Indian Ridge (SEIR) (McKenzie and Sclater, 1973; Chatterjee et al., 2013). These ridge structures have very different spreading rates and they converge at the Rodriguez Triple Junction (RTJ) in the mid-ocean region. They also mark the boundaries between three major tectonic plates; the Central Indian Ridge and Carlsberg Ridge form the tectonic division between the Somalia (or Africa) and Indo-Australia Plates, the Southeast Indian Ridge separates the Antarctica and Indian–Australia Plates, and the Southwest Indian Ridge demarcates Somalia/Africa from Antarctica Plate (Chatterjee et al., 2013). In comparison, The SWIR, characterized by its slow spreading rate (< 2 cm/year), joins with the Mid-Atlantic Ridge (MAR) system in the west. The SEIR , which has the fastest spreading rate of 7 cm/year, joins with the East Pacific Rise in the Pacific Ocean (Chatterjee et al., 2013). The CIR to the north of Rodriguez Triple Junction runs to the north with a sequence of spreading centers and fractures zones in an echelon fashion, while it turns towards the northwest direction as CR. The CIR and CR systems form the boundary between the Somalia/Africa and Indo-Australian Plates. The Java-Sumatra trench system in the eastern side and the Makran trench in the northwest side are the other two major tectonic features of the Indian Ocean (Bouysse et al., 2004).

As mentioned earlier, the Indian Ocean lithosphere is shared between different major tectonic plates. The Indian and Australian plates were earlier considered as a single unit. But, the global plate motion data and the intraplate seismicity exhibited by the assumed India-Australia single plate, redefined the plate boundary geometry in the Indian ocean and suggested a wide diffused east-west trending boundary, from the CIR to the Java trench, separating the Indian and Australian plates as the two distinct plates (Weissel et al., 1980; Gorden et al., 1990; Royer and Gorden, 1997; Gorden et al., 1998; Conder and Forsyth, 2001; DeMets et al., 2010). A larger misfit in plate motion models along the SEIR exists, than that along other plate boundaries. Royer and Gordon (1997) supported the presence of an additional diffused plate boundary within the Australian plate, to explain misfit along the SEIR, which was introduced as ‘Capricorn’ microplate between India and Australia.

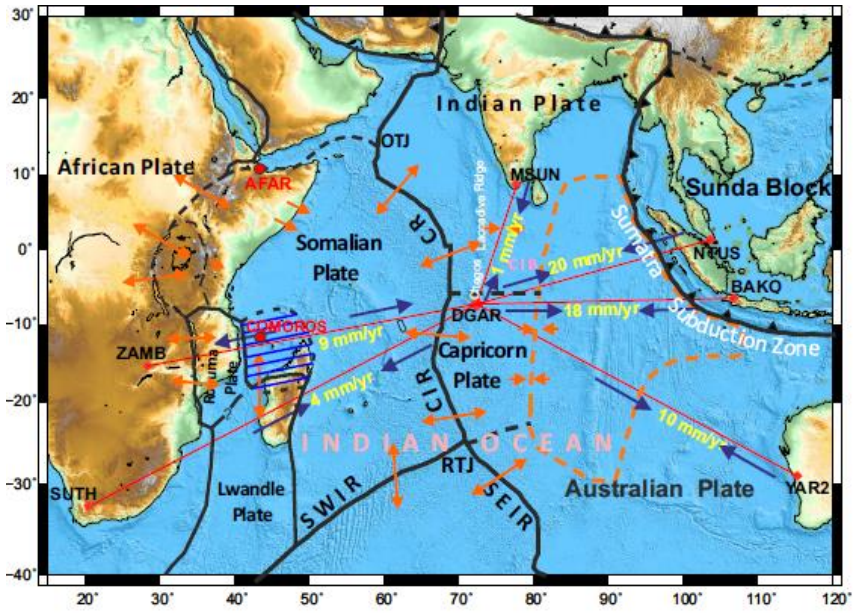

Figure 1. Major tectonic plates and plate boundaries in and around the Indian Plate. Orange broken line marks the diffused plate boundary inferred between the Indian and Australian Plates. Location of the GPS sites (red diamond symbol) and the baseline lengths analyzed, along with their annual rates of change are given. A broad deformation zone that is being formed east of Rovuma in the Somalian Plate, is also shown (Blue lines). SWIR-South West Indian Ridge; SEIR-South East Indian Ridge; CIR-Central Indian ridge; RTJ-Rodrigues Triple Junction; OTJ-Owen Triple Junction.

Thus the original Indo-Australian plate is now considered to be made of three smaller plates: the Indian, Australian, and central `Capricorn' microplate (Figure 1) (Conder and Forsyth, 2001). The boundary between the Capricorn microplate and the Australian Plate extends from the SEIR to the southwest of Java Trench. The primary objective of the present study is to estimate inter-continental scale relative plate motion, which can be inferred by calculating the change in baseline length between the GPS sites in different plates.

GPS DATA ANALYSIS

We analyzed the GPS data from the IGS site located within the Capricorn microplate, namely Diego Garcia (DGAR), and six other sites surrounding the Capricorn plate (Figure 1). All the six sites, namely M. S. University (MSUN), Bakosurtanal (BAKO), Yaragadee (YAR2), Zambia (ZAMB), Suther Land (SUTH), and Singapore (NTUS), are located within the major tectonic plates neighboring the Capricorn microplate. The location details of the GPS sites are given in Table 1. The stations BAKO and NTUS are located in the Sunda Plate, the station YAR2 in the Australian Plate, while the stations ZAMB and SUTH are located in the African Plate. All the above sites fall within the rigid plate.

In the present study, we utilize the GPS data recorded from January 2014 to March 2017. The selection of the data time frame is made in such a way that no large earthquakes occur near Diego Garcia during the period, in order to avoid co-seismic and post-seismic deformations in the crust induced by large earthquakes (Paul et al., 2001; Earnest et al., 2005; Jade et al., 2005; Akilan et al., 2014). This data selection will also avoid any bias in the plate motion evaluation due to earthquake induced deformation effects. For example, the 2004 Sumatra earthquake displaced the Diego Garcia by more than 5 mm (Vigny et al., 2005).

The data processing was carried out using the Bernese 5.0 scientific software (Dach et al., 2007) and baseline lengths between different pairs of station were computed and analyzed using the weekly solutions as widely adopted (Larson and Agnew, 1991). For estimating the change in baseline length between the GPS sites, the rate of change of baseline length per year is derived from the baseline length time series, and strain per year, $\left[\frac{dx}{x}\right]$ (where dx is the change in baseline length/year and the x is the length of the baseline length), is estimated for different arms of baseline lengths formed by the station Diego Garcia. The station DGAR is the fixed station for the entire period of data processing. During the processing, the satellite clock error, receiver clock error, ionosphere error, and the troposphere errors were removed. The precise orbital files were used during the processing. The estimated baseline lengths between different GPS sites, with respect to Diego Garcia, and strain rates are given in Table 2 and Figure 1. As can be seen from Table 2, the R.M.S. error for all the estimations are less than 3 mm.

Table 1. Details of the GPS stations

Station name	Latitude (Deg.)	Longitude (Deg.)	Tectonic plate	Station details
M.S. University (MSUN)	8.76	77.65	Indian plate	NGRI permanent station
Bakosurtanal (BAKO)	-6.49	106.85	Eurasian plate	IGS station
Yarragadee (YAR2)	17.42	78.55	Australian plate	IGS station
Zambia (ZAMB)	-15.43	28.31	African plate	IGS station
Suther Land (SUTH)	-32.38	20.81	African plate	IGS station
Singapore (NTUS)	1.35	103.68	Eurasian plate	IGS station
Diego Garcia (DGAR)	-7.27	72.37	Capricorn plate	IGS station

Table 2. The baseline length between the stations, the corresponding rate per year and the strain rate

Pair of GPS stations	Baseline length between the stations (m)	Rate (mm/yr)	Error (mm)	Strain rate
DGAR-BAKO	3754380.299	-18	2	-4.7944×10^{-9}
DGAR-MSUN	1860354.464	-1	1	-5.37532×10^{-10}
DGAR-NTUS	3557623.589	-20	2	-5.62173×10^{-9}
DGAR-SUTH	5781513.409	-4	3	-6.9186×10^{-10}
DGAR-YAR2	4969198.225	-10	2	-2.0124×10^{-9}
DGAR-ZAMB	4765990.320	9	3	1.88838×10^{-9}

RESULTS

The rate of change in baseline length between two measurement sites (changes in the distance between the pair of stations per year) shows the relative motion between the two sites (Figure 2). While a negative baseline rate indicates convergence between the two studied points used to compute the baseline, a positive value indicates divergence. The accuracy of baseline lengths estimated using GPS is higher below the threshold baseline length of 6000 km (Dach et al., 2007). The baseline lengths estimated between DGAR and the other stations (BAKO, MSUN, NTUS, SUTH, YAR2 and ZAMB) range from 1860354.464 m to 5781513.409 m (Table 2; Figure 1). The changes in baseline length generally suggest the deformation at the plate boundary, but it can also be due to deformation occurring within the plate (intra-plate). The strain rate between the pair of stations, provides an overall indication about the seismicity within the region bounded by the two points on earth. Higher strain rate implies that earthquake occurrence is more likely in the region between the two points, while less strain rate suggests, least seismic activity. The strain rates observed for the different pairs of stations considered in this study vary between -6.9186×10^{-10} and 1.88838×10^{-9} (Table 2). The study provides significant inferences about the observed baseline lengths and strain rates for each station pair and their implications to understand the plate tectonic process operating between the plates in the studied region.

The computed rate of change of baseline length between the DGAR station in the Capricorn microplate and the BAKO station in the Sunda Plate, is -18 mm/yr, which suggests that the two stations are in convergent motion and approaching each other at a rate of 18 mm/yr. Previous study has estimated a NNE resultant velocity of 30.61 mm/yr (north velocity of 30.28 mm/yr and east velcoty of 4.50 mm/yr) for DGAR station with respect to Kerguelen isaland in the Antarctica plate and relative to ITRF 00 (Ravikumar et al., 2008). The major plate boundary existing between the plates, represented by the above two stations, is the wide diffused plate boundary zone that acts as the common divider of the Capricorn-India-Australia-Sunda Plate system (DeMets and Royer, 2003). The east-west orientation of the DGAR-BAKO baseline suggests that the observed deformation can be attributed to the ongoing subduction of the India-Australia-Capricorn microplate system beneath the Sunda block. The deformation caused by the subduction process is producing strain at a yearly rate of -4.7944×10^{-9}, which might be accommodated in the deforming zone and thus could provide necessary conditions for seismogenesis. Similarly, the rate of change of baseline length for the DGAR-NTUS pair, shows a comparable value of -20 mm/year with a corresponding strain rate of -5.62173×10^{-9}. Kreemer et al. (2003) however, estimated higher strain that accumulated in the Sumatra subduction zone resulting in significant seismic hazards in the region. The occurrence of diffuse deformation between DGAR and NTUS, may have contribution from the ongoing subducation occurring along the Sumatra trench, in addition to the diffuse deformation within the Indian Ocean. The present study cannot clearly throw light on to the effect of these two different geological processes on the deformation between DGAR and NTUS.

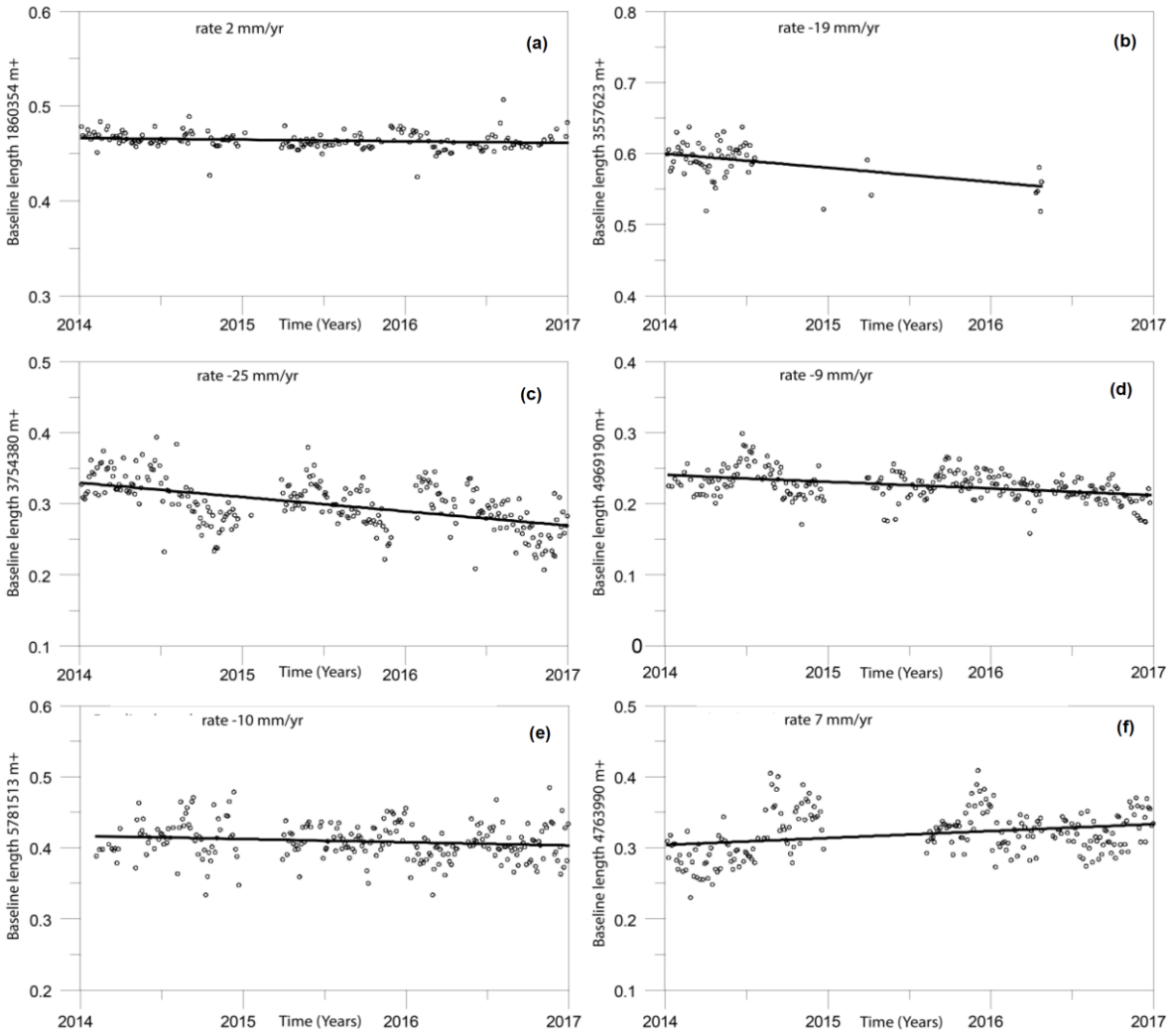

Figure 2. Changes in baseline length between the station pairs, **(a)** DGAR and MSUN, **(b)** DGAR and NTUS, **(c)** DGAR and BAKO, **(d)** DGAR and YAR2, **(e)** DGAR and SUTH and **(f)** DGAR and ZAMB. Their rate of change is shown against each block.

The relative motion between the Capricorn and Indian Plates are inferred from changes in baseline length occurring between the DGAR and MSUN stations, representing the Indian plate. The DGAR-MSUN pair gives a marginal decreasing trend of the baseline length at a rate of 1 mm/yr, which suggests a convergent motion between the Indian plate and Capricorn microplate. The corresponding estimated strain rate is -5.37532 x 10^{-10}. Similarly, the change in baseline length computed for the DGAR-YAR2 pair is -10 mm/yr, which indicates a shortening of baseline length between the Capricorn microplate and the Australia Plate at a rate of 10 mm/yr. The results of this study show a convergence between the Capricorn oceanic lithospheric block and the Australian lithospheric plate, which is in agreement with the findings of Royer and Gordon (1997) that proposed a diffused convergent boundary between the Capricorn microplate and the Australian Plate. Kreemer et al. (2003) have inferred a convergence at the rate of ~11 mm/yr between India and Australia. This study gives the relative motion (convergence) between the Capricorn and Australian Plates at a rate of 10 mm/yr. The estimated strain generated due to this convergence is -2.0124 x 10^{-9}, which could be accommodated along the diffused plate boundary between the Capricorn and Australia Plates.

The kinematics of the Capricorn microplate with respect to the African plate to its west, can be understood from changes in baseline length computed for the DGAR-ZAMB and DGAR-SUTH station pairs (Figure 1). Both the stations ZAMB and SUTH, represent the African Plate. It is found that the baseline change between DGAR and ZAMB occurs at a rate of 9 mm/yr, but that between DGAR and SUTH

(SUTH is in the southern margin of the African plate) is -4 mm/yr. Several tectonic blocks are present between DGAR and ZAMB stations. However, it is not possible to assess the deformation effects at each tectonic segments separately.

DISCUSSION

The plate boundary between the Capricorn microplate and the African plate is defined by the CIR, which is an active spreading ridge in the Indian Ocean (Fisher et al., 1971; Eagles and Hoang, 2014). The dynamics of the plates is well reflected in the rate of change in baseline lengths, as obtained in the present study. Long baselines should be evaluated cautiously as the vertical component of the deformation begins to influence the baseline length between the GPS station pairs having large station spacing. In our study, the stations are not located over geodynamically active zones with significatnt vertical deformation. Hence, the influence of vertical deformation is negligible in the baseleine lengths presented in this study. Divergent kinematics, as seen by the GPS baseline rate estimates, correlates well with the ongoing east-west divergence between the African and Somalian Plates, along the East African rift system (Horner-Johnson et al., 2007). The strain calculated for the DGAR-ZAMB pair baseline is positive, i.e. 1.88838×10^{-9}, suggesting no strain accumulation at the boundary between the African and Indian Plates, which also correlates with the low seismicity along the CIR, as compared to the SWIR and SEIR. On the other hand, the DGAR-SUTH pair shows a convergence motion between the plates at a rate of -4 mm/yr. The above contradicting observation seen between the two baseline arms, i.e., DGAR-ZAMB and DGAR-SUTH, having stations within same plates (i.e., DGAR in Capricorn microplate, and ZAMB and SUTH in African Plate), illustrate a complex plate dynamics in the region. The Lwandle-Somalia Plate boundary is now inferred to be a diffused plate boundary zone that gives rise to the east-west convergence (e.g., Horner-Johnson et al., 2007). Thus, our GPS observation along the DGAR-SUTH arm, clearly identifies the convergent plate kinematics occurring between the African Plate and the southern segment of the Somalia Plate. Therefore, we infer that the convergence along the diffused Lwandle-Somalia Plate boundary, dominates over the divergence along the CIR.

Cause of divergence between DGAR and ZAMB

As mentioned earlier, baseline lengths estimated between DGAR and ZAMB, show a divergence between the two plates. The estimated rate of divergence is 9 mm/yr. Earlier, Royer and Gorden (1997) too indicated that the Indian Plate, west of the Capricon micro-plate is diverging in contrast to the convergence of the Indian Plate with respect to the Australian Plate, located east of the Capricon microplate. It appears that the Somalian plate is undergoing deformation due to internal spreading below the Comores Islands and its surrounding regions due to the presence of Comores hotspot underneath. This hotspot is located at around 12°S and 43°E in the Somalian Plate (Courtillot et al., 2003), which is considered as an active volcanic region and thus undergoing rifting and spreading, as found between DGAR and ZAMB. This spreading is possibly percolating down to south across the northern part of Madagascar, which may well be fragmenting and deforming (Hartnady, 2002; Stamps et al., 2008; Kusky et al., 2010). Northern part of Madagascar and the Comores Island is deforming inconsistently with rigid plate motion (Stamps et al., 2021). Northern Madagascar moves rigidly with the Somalian Plate and southern Madagascar moves with the Lwandle microplate (Saria et al., 2014).

Formation of a new deformation zone

It is well known that a large-scale thermal anomaly exists in the Afar region and most researchers ascribe it to a deep mantle plume (Horner-Johnson et al., 2007). Intriguingly, Comores hotspot is aligned with the Afar hotspot in the Red sea region of Ethiopia. Currently, the Red sea rifting region joins with the rifting associated with the East African rift system, which is one of the world's longest rifts that extends for thousands of kilometer from Ethiopia to Mozambique and passes through the multiple African countries. In a similar manner, the Madagascar, which is an island country in the Indian Ocean, that broke out from the Indian subcontinent at around 88 Ma back due to the outburst of the Marion plume (Agrawal et al., 1992), has again been breaking up, into smaller islands. Quite likely, the East African rift system may, in some way, be associated with the breaking up of northern Madagascar as well. This suggests that a broad deformation zone is being formed to east of Rovuma in the Somalian Plate (Figure 1) due to internal rifting of the Somalian Plate that covers the northern part of Madagascar and the northernmost part of the Lwandle Plate. (Figure 1). Stamps et al. (2021) recently indicated that the Comores Islands region, which is a diffused transitional zone, accommodates extension between the Somalian Plate and the Rovuma microplate.

The main constraint of this work lies in the reliance on a single site data (DGAR), which is situated on an island in the northern region of the proposed Capricorn microplate. Additional GNSS array with dense stations would definitely be needed to provide a better picture of the plate kinematics of the Capricorn microplate and its surrounding regions.

CONCLUSIONS

We studied the relative plate motions between the Capricorn microplate and the surrounding plates, viz., Indian, Australian, Sunda and African Plates, using the changes in baseline length values obtained from the GPS data. The relative motion between India and Diego Garcia is convergent in nature and occurs at a quite low rate of ~1 mm/yr. The rate of change in baseline length between the DGAR station in the Capricorn microplate and the BAKO station in the Sunda Plate, shows significant convergence at a rate of 18 mm/yr. The change in baseline length computed for the DGAR-YAR2 pair, indicates a shortening of baseline length between the Capricorn microplate and the Australia Plate at a rate of 10 mm/yr, which is in agreement with diffused convergent boundary inferred between Capricorn and Australia by Royer and Gordon (1997). Importantly, contrasting baseline change is obtained between DGAR and a station located in the African Plate . The DGAR-ZAMB pair shows divergence between the two plates at a rate of 9 mm/yr, while the DGAR-SUTH (station located in the southern margin of the African Plate) pair, shows a convergence motion between the plates at a rate of 4 mm/yr, which are well correlated with the complex plate kinematics in this region. Our results infer an amalgamation of the Australian continent, Sunda block and Diego Garcia from the plate tectonic kinematics. It appears that a broad deformation zone is being formed to east of the Rovuma Plate in the Somalian Plate due to regional rifting that covers the northern part of Madagascar and the northernmost part of the Lwandle Plate.

Acknowledgements

We thank Dr. Prakash Kumar, Director, CSIR-NGRI for granting permission to publish this work. The GPS data used in this study are obtained from the global data center (http://sopac.ucsd.edu/dataBrowser.shtml). This work has been carried out under the MLP 7018-28(HVS) project of CSIR-NGRI.

Author Credit Statement

A. Akilan: Conceptualised, processed the data and wrote the paper. K. K. Abdul Azeez, Sravan K Kotluri, H.V.S. Satyanarayana, S. Padhy, O.P. Pandey wrote and edited the paper.

Data Availability

All the data (except MSUN) downloaded from global data base and available from the corresponding author on reasonable request.

Compliance with Ethical standards

The authors declare no conflict of interest and adhere to copyright norms

References

Agrawal, P.K., Pandey, O.P. and Negi, J.G., 1992. Madagascar: A continental fragment of the paleo-super Dharwar craton of India. Geology, 20, 543-546.

Akilan, A., Balaji, S. and Srinivas Y., 2014. Are the tectonic blocks around the Wharton basin dispersed during an earthquake? – A GPS Geodesy solution. Indian J. Geo-Marine Sci., 43, 453-462.

Akilan, A., Balaji, S., Padhy, S., Abdul azeez, K.K. and Srinivas, Y., 2016. The Plate kinematics of Burmese micro-plate relative to its surroundings. Arabian J. Geosci., 9, 1-8.

Bevis, M., Taylor, F.W., Schutz, B.E., Recy, J., Isacks, B.L., Helu, S., Singh, R., Kendrick, E., Stowell. J., Taylor, B. and Calmant, S., 1995. Geodetic observations of very rapid convergence and back-arc extension at the Tonga arc. Nature, 374, 249-251.

Bird, R.T. and Naar, D.F., 1994. Intratransform origins of mid-ocean ridge microplates. Geology, 22, 987-990.

Bouin, M.N. and Vigny, C., 2000. New constraints on Antarctic plate and deformation from GPS data, J. Geophys. Res., 105, 28279- 28293.

Bouysse, P., Mendel, V., Menschy, K. and Sgoufin, J., 2004. The map of the Indian Ocean. Physiographic and structural mapping of an ocean, Bilingual French–English. 1–6. CGMW edition, Paris.

Chapple, W.M. and Forsyth, D.W., 1979. Earthquakes and bending of plates at trenches. J. Geophys. Res., 84, 6729-6749.

Chatterjee, S., Goswami, A. and Rcotese, C.R., 2013. The longest voyage: Tectonic, magmatic, and paleoclimatic evolution of the Indian plate during its northward flight from Gondwana to Asia. Gondwana Res., 23, 238-267.

Conder, J.A. and Foryth, D.W., 2001. Seafloor spreading on southeast Indian ridge over the last one million years: a test of the Capricorn plate hypothesis. Earth Planet. Sci. Lett., 188, 91-105.

Courtillot, V., Davaillie, A., Besse, J. et al., 2003. Three distinct type of hot spots in the earth's mantle. Earth Planet. Sci. Lett., 205, 295-208.

Curray, J. R. and Munasinghe, T. 1991. Origin of the Rajmahal Traps and the 857E ridge: preliminary reconstructions of the trace of the crozet hotspot. Geology, 19, 1237–1240

Dach, R., Hugentobler, U., Fridez, P. And Meindl, M., 2007. User manual of the Bernese GPS software version 5.0, Astronomical Institute, University of Bern.

DeMets, C. and Royer, J-Y., 2003. A new high-resolution model for India-Capricorn motion since 20 Ma: Implications for the chronology and magnitude of distributed crustal deformation in the central Indian basin. Curr. Sci., 85, 339-345.

DeMets, C., Gorden, R.G. and Argus, D.F., 2010. Geologically current plate motions. Geophys. J. Int., 181, 1-80.

Dixon, T.H., 1991. An introduction to the global positioning system and some geological applications. Rev. Geophys., 29, 249-276.

Duncan, R.A. and Pyle, D.G., 1988. Rapid eruption of the Deccan flood basalts at the Cretaceous / Tertiary boundary. Nature, 33, 841–843.

Eagles, G. and Hoang H.H., 2014. Cretaceous to present kinematics of the Indian, African and Seychelles plates. Geophys. J. Int., 196, 1-14.

Earnest, A., Rajendran, C.P., Rajendran, K., Anu, R., Arun, G.M. and Mohan, P.M., 2005. Near-field observations on the co-seismic deformation associated with the 26 December 2004 Andaman-Sumatra earthquake. Curr. Sci., 7, 1237-1244.

Fisher, R.L., Sclater, J.G. and Mckenzie, D.P., 1971. Evolution of the central Indian ridge, western Indian Ocean. Geol. Soc. Am. Bull., 82, 553-562.

Gorden, R.G., DeMets, C. and Argus, D.F., 1990. Kinematic constraints on distributed lithospheric deformation in the equatorial Indian Ocean from present motion between the Australian and Indian plates. Tectonics, 9, 409-422.

Gorden, R.G., DeMets, C. and Royer, J-Y., 1998. Evidence for long-term diffuse deformation of the lithosphere of the equatorial Indian Ocean. Nature, 395, 270-273.

Hartnady, C.J.H., 2002. Earthquake hazard in Africa: Perspectives on the Nubia-Somalia boundary. South Ahrican J. Science, 98, 425-428.

Henstock, T.J. and Minshull., 2004. Localized rifting at Chagos Bank in the India-Capricorn plate boundary zone. Geology, 32, 237-240.

Horner-Johnson, B.C., Gorden, R.G. and Argus, D.F., 2007. Plate kinematic evidence for the existence of a distinct plate between the Nubian and Somalian plates along the southwest Indian ridge. J. Geophys. Res., 112, B05418, doi:10.1029/2006JB004519

Jade, S., Ananda, M.B., Dileep Kumar, P. and Banerjee, S., 2005. Co-seismic displacements in Andaman and Nicobar Islands from GPS measurements. Curr. Sci., 88, 1980-1984.

Koehn, D., Aanyu, K., Haines, S. and Sachan, T., 2008. Rift Nucleation, rift propagation and the creation of basement micro-plates within active rifts. Tectonophysics, 458, 105-116.

Kreemer, C., Holt, W.E. and Haines, A.J., 2003. An integrated global model of present-day plate motions and plate boundary deformation. Geophys. J. Int., 154, 8-34.

Kusky, T.M., Raharimahefa, T., Rasoazanam-parany, C. and Toraman, E., 2010. Active tectonics of the Alaotra-Ankay graben system, Madagascar: Possible extenson of Somalian-African diffusive plate boundary?.Gondwana Res.,18, 274-294.

Larson, K.M. and Agnew, D.C., 1991. Application of global positioning system to crustal deformation measurement 1. Precision and Accuracy. J. Geophys. Res., 96, 16547-16565.

Mckenzie, D.P. and Sclater, J.G., 1973. The evolution of Indian Ocean. Scientific Am., 228, 63-72.

Minster, J.B. and Jordan, T.H., 1978. Present-day plate motions. J. Geophys. Res., 83, 5331-5354.

Paul, J., Burgmann, R., Gaur, V.K., Bilham, R., Larson, K.M., Ananda, M.B., Jade, S., Mukal. M., Anupama, T.S., Satyal, G. and Kumar, D., 2001. The motion and active deformation of India. Geophys. Res. Lett., 28, 647-650.

Radha Krishna, M., Verma, R.K. and Arora, S.K., 1998. Near-ridge intraplate earthquakes in the Indian Ocean. Marine Geology, 147, 109-122.

Ravikumar, N., Malaimani, E.C., Akilan, A. and Abilash, K., 2008. 10 years of Continous GPS measurements for geodetic tying of Antarctica and India for geodynamical and strain accumulation studies in the south of Indian Peninsula. J. Indian Geophys. Union, 12, 115-122.

Reeves, C.V. and de Wit, M.J., 2000. Making ends meet in Gondwana. Retracing the transforms of the Indian Ocean and reconnecting continental shear zones. Terra Nova, 12, 272–282.

Royer, J-Y. and Change, T., 1991. Evidence for relative motions between the Indian and Australian plates during the last 20 m.y from plate tectonic reconstruction: Implications for the deformation of the Indo-Australian plate. J. Geophys. Res., 96, 11779-11802.

Royer, J.Y. and Gorden, R.G., 1997. The motion and boundary between the Capricorn and Australian plates. Science, 277, 1268-1274.

Royer, J-Y., Chateau, R., Dziak, R.P. and Bohnenstiehl, D.R., 2015. Seafloor seismicity, Antarctic ice-sounds, cetacean vocalizations and long-term ambient sound in the Indian Ocean basin. Geophys. J. Int., 202, 748-762.

Saria, E., Calais, E., Delvaux, D., Hartnady , C.J.H. and Stamps, D.S., 2014. Present-day kinematics of the East African Rift. J. Geophys. Res., 119, 3584-3600

Schlich, R., 1982. The Indian Ocean: Aseismic Ridges, Spreading Centers, and Oceanic Basins. In: Nairn A.E.M., Stehli F.G. (eds) The Ocean Basins and Margins. Springer, Boston, MA.

Sella, G.F., Dixon T.H and Mao, A., 2002. REVEL: A model for recent plate velocities from space geodesy. J. Geophys. Res., 107, B4. http://doi:10.1029/2000JB000033.

Sinton, J.M. and Detrick, R.S., 1992. Mid-ocean ridge magma chambers. J. Geophys. Res., 97, 197-216.

Stamp, D.S., Calais, E., Ebinger, C.J., Fernandes, R.M., Hartnady, C., Nocquet, J.M. and Saria, E., 2008. A kinematic model for the East African Rift Geophys. Res. Lett., 35, L 05304. https://doi.org/10.1029/2007GL032781

Stamps, D.S., Kreemer,C., Fernandes, R., Rajaonarison, T.A. and Rambolamanana, G., 2021. Redefining east African Rift System kinematics. Geology, 49, 150-155.

Stein, S. and Gorden, R.G., 1984. Statistical tests of additional plate boundaries from plate motion inversions. Earth Planet. Sci. Lett., 69, 401-412.

Tinnon, M.J. and Holt, W.E., 1995. Velocity gradients in the northern Indian Ocean inferred from earthquake moment tensors and relative plate velocities. J. Geophys. Res., 100, 24315-24329.

Vigny, C., Simons, W.J.F., Abu, S., Bamphenyu, R., Satirapod, C., Choosakul, N., Subarya, C., Socquet, A., Omar, K., Abidin, H.Z. and Ambrosius, B.A.C., 2005. Insight into the 2004 Sumatra-Andaman earthquake from GPS measurements in southest Asia. Nature, 436, 201-206.

Weissel, J.K., Anderson, R.N. and Geller, C.A., 1980. Deformation of Indo-Australian plate. Nature, 287, 284-291.

Wilson, J.T.and Burke, K., 1972. Two type of Mountain building. Nature, 239, 448-449.

Received on: 24-10-2024; Revised on: 12-01-2025 ; Accepted on: 16-01-2025

J. Ind. Geophys. Union, 29(1) (2025), 64-67
https://doi.org/10.71122/JIGU.29(1)2025.007

Report on 61st Annual Convention of the Indian Geophysical Union (IGU), held at Banaras Hindu University (BHU), Varanasi (India) during December 3–5, 2024

Abhey Ram Bansal[1*], A.S.S.S.R.S. Prasad [1] and R K Mall[2]
[1]CSIR-National Geophysical Research Institute, Hyderabad-500007 (India)
[2]Institute of Environmental and Sustainable Department, Banaras Hindu University, Varanasi-221005 (India)
*Corresponding author: hsecigu@gmail.com

The Indian Geophysical Union (IGU) successfully organized its 61st Annual Convention in collaboration with the Institute of Environment and Sustainable Development and the Department of Geophysics, Banaras Hindu University (BHU), Varanasi. The convention took place from December 3–5, 2024, under the special theme "*Advances in Earth System Sciences with Special Reference to Weather and Climate"* focussing on topics like Solid Earth, Marine Geosciences, and Atmospheric, Planetary and Space Sciences. The three-day event was inaugurated on December 3, 2024, in the Mahamana Auditorium by Dr V.K. Saraswat, a Member of NITI Aayog, who served as the Chief Guest (Figure 1).

During the inaugural ceremony, IGU President Dr M. Ravichandran addressed the gathering (Figure 2) and honoured the IGU awardees for 2024 (Figures 3-4), as well as researchers and postgraduate students. The program received extensive media coverage. During the ceremony Chief guest has released the abstract volume (Figure 5).

The convention featured an impressive line-up of keynote addresses, award lectures, and invited talks, delivered by eminent scientists, including Prof. Harsh K. Gupta, Prof. V. K. Gaur, Dr. Prakash Chauhan, Dr. Ajay Mangalik, Dr. Kalachand Sain and Prof. N. V. Chalapathi Rao. Dr. Ranjit Rath, CMD of Oil India, inaugurated the scientific instrument exhibition stalls (Figure 6).

The IGU Awards have been given to the following eminent scientists, senior scientists, young scientists, young women researchers and postgraduate students.

Dr. K.S. Krishna
IGU-Hari Narain Lifetime Achievement Award

Dr. Prakash Chauhan
IGU-Prof. K.R. Ramanathan Memorial Lecture Award

Dr. Ajay P. Singh
IGU-Anni Talwani Memorial Prize

Dr. Bhaskar Kundu
IGU-Krishnan Medal

Dr. Som Dutt
IGU-J.G. Negi Young Researchers Award

Dr. Ashutosh Pandey
IGU-J.G. Negi Young Researchers Award

Tabish Khan, S.P. Anand and S.K. Begum received the IGU-Prof. D. Lal Best Paper Award for their paper entitled "Comparison of satellite derived gravity models with ground data: A case study from the Deccan Volcanic Province (India)" published in J. Indian Geophys. Union, 27(6) (2023), 409-425.

Following **Young Women Researchers** received "**IGU-Anni Talwani Memorial Grant.**

1. Ms. Machitti Pavani, CSIR-National Geophysical Research Institute, Hyderabad, India
2. Ms. Venkata Durga, N., CSIR-National Geophysical Research Institute, Hyderabad, India
3. Ms. Annie Jose, MS University, Tirunelveli, Tamil Nadu, India
4. Ms. Kurakula Kalyani, Wadia Institute of Himalayan Geology, Dehradun, Uttarakhand, India

Figure 1: Inauguration by Chief Guest Dr V.K. Saraswat.

Figure 2: Presidential Address by Dr. M. Ravichandran.

Figure 3: IGU - Dr. Hari Narain Life Time achievement Award Presented to Dr. K. S. Krishna.

Figure 4: IGU - Prof. K R Ramanathan Memorial Lecture Award Presented to Dr. Prakash Chauhuan.

Figure 5: Release of the abstract volume.

Figure 6: Inauguration of Exhibition stalls by Dr. Ranjit Rath.

Similarly, IGU-Prof. Jagdeo Singh and Dr. S. Balakrishna Memorial Grant for Student Toppers – 2024, was awarded to:

1. Jhadhav Tanishka (Osmania University, Hyderabad)
2. Pullaguri Shereesha (Osmania University, Hyderabad)
3. Morusupalli Dedeepya (Andhra University, Visakhapatnam)
4. Valle Ramya Sri (Andhra University, Visakhapatnam)
5. Dokkari Sravani (Andhra University, Visakhapatnam)
6. Mogalapu Amulya (Andhra University, Visakhapatnam)
7. V. Madhu Babu (Adikavi Nannaya University, Rajamahendravaram)
8. K. Jashnavi Sai Harini (Adikavi Nannaya University, Rajamahendravaram)
9. P. Boopathy Raja (MS University, Tirunelveli)
10. Sasipraba, S. (MS University, Tirunelveli)
11. Amol Kamble (SRTM University, Nanded)
12. Prajakta Panchal (SRTM University, Nanded)
13. Tignangshu Das (IIT-ISM, Dhanbad)
14. Yashovardhan Gupta (IIT-ISM, Dhanbad)
15. Jainendra Tripathy (IIT-ISM, Dhanbad)
16. Raj Sahu (IIT-ISM, Dhanbad)
17. Devananda Pradeep (CUSAT, Kochi)
18. Nidhin, P. (CUSAT, Kochi)
19. Bisal Shaw (BHU, Varanasi)
20. Aman Kukreti (BHU, Varanasi)
21. Hemant Yadav (Kurukshetra University, Kurukshetra)
22. Neeraj (Kurukshetra University, Kurukshetra)
23. Sneh Yadav (Kurukshetra University, Kurukshetra)
24. Utkarsh Prajapati (IIT Roorkee, Roorkee)
25. Mridul Sharma (IIT Roorkee, Roorkee)
26. Bharat Sharma (IIT Kanpur, Kanpur)
27. Ayushi Nautiyal (IIT Kanpur, Kanpur)

The conference attracted more than 400 delegates (Figure 7). In addition to the delivered prestigious lectures, over 300 research paper were also presented at different technical sessions. The event provided an excellent platform for meaningful interactions between senior scientists, young researchers, and students, fostering collaboration and knowledge exchange (Figures 8-10). During the concluding session, awards were presented by the Chief Guest, Prof. Raghuvanshi, to recognize the achievements of researchers and scholars (Figures 11-12). The IGU Best Presentation

Awards were given under the Young Researcher Program, and the IGU-ONGC Best Poster Presentation Awards were presented in the Researcher and PG Student categories.

IGU-ONGC Best Oral Presenter Award for Young Researcher Program

Ms. Sushrita Dutta (IIT Bombay, Mumbai) – First Prize

Mr. Yezarla Mahesh (CSIR-NGRI, Hyderabad) – Second Prize

Mr. Sareer Ahmad Mir (University of Kashmir, Srinagar) – Second Prize

IGU-ONGC Best Poster Presenter Award

Researcher Category

Ms. Priya Maurya (WIHG, Dehradun) – First Prize

Mr. Manan Singh (Indian Institute of Geomagnetism, Navi Mumbai) –Second Prize

Student Category

Ms. Saranya R. Pramod (CSIR-NGRI, Hyderabad) – First Prize

Ms. Chabungbam Yaiyaisana (Kurukshetra University, Kurukshetra) – Second Prize

Figure 7: Delegates at 61st IGU Annual Convention.

Figure 8: Interaction at poster sessions.

Figure 9: Interaction at poster sessions.

Figure10: Interaction at poster sessions.

Figure 11: Presentation of award to Young Researcher.

Figure 12: Presentation of awards to Young Researcher.

IGU expressed heartfelt gratitude to the Local Organizing Committee (LOC), led by Prof. S. K. Jain, Vice-Chancellor of BHU and Chairman of the LOC, along with Co-Chair persons Prof. A. S. Raghubanshi (Director, IESD) and Prof. G. P. Singh (Head, Department of Geophysics). Special acknowledgement was also extended to Prof. Sanjay Kumar (Rector), Prof. R. K. Mall (IESD and Convener, LOC), and other LOC members for their dedication to ensuring seamless technical sessions and robust delegate participation.

The IGU Executive Committee also acknowledged the support of key individuals, including:

Patron:	Prof. Shailesh Nayak
President:	Dr. M. Ravichandran
Past Presidents:	Prof. Harsh K. Gupta and Prof. V. P. Dimri
Vice Presidents:	Dr. Prakash Kumar, Dr. A. P. Dimri, Dr. Sushma Rawat, and Dr. T. Srinivas Kumar
Chief Editor, JIGU:	Dr. O. P. Pandey

A special vote of thanks was extended to the technical session chairpersons for conducting the sessions as scheduled and to all Fellows and Members of IGU for their unwavering support. IGU expressed its deep appreciation to the following organizations for their financial support, which was critical to the convention's success:

- Ministry of Earth Sciences (MoES), New Delhi
- Oil India Limited (OIL), Delhi
- Oil and Natural Gas Corporation (ONGC), New Delhi
- National Centre for Polar and Ocean Research (NCPOR), Goa
- CSIR-National Geophysical Research Institute (CSIR-NGRI), Hyderabad
- National Institute of Ocean Technology (NIOT), Chennai
- National Centre for Earth Science Studies (NCESS), Thiruvananthapuram
- Indian National Centre for Ocean Information Services (INCOIS), Hyderabad
- National Remote Sensing Centre (NRSC), Hyderabad
- CSIR-North East Institute of Science and Technology (NEIST), Jorhat
- CSIR-National Institute of Oceanography (NIO), Goa
- Banaras Hindu University, Varanasi

IGU also thanked CSIR-NGRI, NRSC, AIMIL Ltd., HGS (India) Limited, Complete Instrumentation Solutions Pvt. Ltd., Pan India Consultants Pvt. Ltd., and Shijay Projects India Pvt. Ltd. for setting up stalls to showcase cutting-edge products and services related to geoscientific data acquisition, processing, modelling, and interpretation. A special mention was made of Mr. Rafique Mohammad Attar, Treasurer of IGU, for his tireless efforts in coordinating the various aspects of the convention. IGU convention concluded on 5th December, 2024 (Figure 13)

Figure 13: Delegates at Concluding session.

Received: 26-1-2025, Revised: 5-2-2025, Accepted: 6-2-2025

GUIDE FOR AUTHORS

The Journal of Indian Geophysical Union (JIGU), a SCI Journal published bimonthly by the Indian Geophysical Union (JIGU), is an inter disciplinary journal from India that publishes high-quality research in earth sciences with special emphasis on the topics pertaining to the Indian subcontinent and the surrounding Indian Ocean region. The journal covers several scientific disciplines related to the Earth sciences such as solid Earth Geophysics, geology and geochemistry, apart from marine, atmosphere space and planetary sciences. J-IGU welcomes contributions under the following categories :

*Research articles, short notes and students section reporting new findings, results, etc.

*Review articles providing comprehensive overview of a significant research field.

In addition, JIGU also welcomes short communications, after communications and report on scientific activity, book reviews, news and views, etc.

The manuscript should be submitted electronically as a single word format (.doc file) including the main text, figures, tables, and any other supplementary information along with the signed "Declaration Letter". The manuscript should be submitted by email (jigul1963@ gmail.com) to the Chief Editor.

After acceptance of the manuscript the corresponding author would be required to submit all source files (text and Tables in word format) and figure in high resolution standard (*.jpg, *.tiff, *.bmp) format. These files may be submitted to JIGU as a single *.zip file along with the "Copyright Transfer Statement".

IMPORTANT INFORMATION

Ethics in publishing; J-IGU is committed to ensuring ethics in publication and takes a serious view of plagiarism including self-plagiarism in manuscripts submitted to the journal, Authors are advised to ensure ethical values by submitting only their original work and due acknowledgement to the work of others used in the manuscript. Authors must also refrain from submitting the same manuscript to more than one journal concurrently, or publish the same piece of research work in more than one journal, which is unethical and unacceptable. Editor of JIGU is committed to make every reasonable effort to investigate any allegations of plagiarism brought to his attention, as well as instances that come up during the peer review process and has full authority to retract any plagiarized publication from the journal and take appropriate action against such authors if it is proven that such a misconduct was intentional.

Similarly, Editor and Reviewers are also expected to follow ethical norms of publishing by ensuring that they don't use any unpublished information, communicated to them for editorial or review purpose, in their own research without the explicit written consent of the author. They are also expected to keep manuscript' data/ observations/ any other information related to the peer review confidential to protect the interest of the authors. Reviewers should refrain from reviewing the manuscripts in which they have conflicts of interest resulting from competitive, collaborative, or other relationships or connections with any of the authors, companies, or institutions connected to the manuscript.

Conflict of interest

All authors are requested to disclose any actual or potential conflict of interest including any financial, personal or other relationships with other people or organizations within three years of beginning the submitted nor that could inappropriately influence, or be perceived to influence, their work.

Submission declaration

Submission of a manuscript implies that the work has not been published previously and it is not under consideration for publication elsewhere, and that if accepted it will not be published elsewhere in the same or any other form, in English or in any other language, without the written consent of the publishers. It also implies that the authors have taken necessary approval from the competent authority of the institute/organization where the work was carried out.

Copyright

After acceptance of the manuscript the corresponding author would be required to sign and submit the "Copyright Transfer Statement".

MANUSCRIPT PREPARATION

The corresponding author should be identified (include E-mail address, Phone/Mobile number). Full affiliation and postal address must be given for all co-authors.

Abstract:

An abstract of not more than 300 words must be included.

Text:

The manuscript should be structured to include a front page containing the title, Author(s) name, affiliation and address of the institute, where the work was carried out, and 5-to-6 Key words. Author(s) present address, if different from the above mentioned address, may be given in the footnote. The corresponding author should be identified with an asterisk and his/her email ID should be provided. This page should be followed by the main text consisting of Abstract, Introduction, Methods/ Techniques/ Area description, Results, Discussion, Conclusions, Acknowledgements, and References. Tables and Figures with captions should be inserted at the end of main text. It should not be inserted in the body of the text.

Figures/ Illustrations:

figures should be provided in camera-ready form, suitable for reproduction (which may include reduction) without retouching. Figures in high-resolution (at least 300 dpi) standard formats (*.jpg, * tiff, *.bmp) are acceptable. Figures should be numbered according to their sequence in the text. References should be made in the text to each figure. Each figure should have a suitable caption.

Tables:

Authors should take note of the limitations set by the size and layout of the journal. Table should not exceed the printed area of the page. They should be typed on separate sheets and details about the tables should be given in the text. Heading should be brief. Large tables should be avoided and may be provided as supplementary information, if required.

Equations:

Equations should be numbered sequentially with Arabic numerals and cited in the text. Subscripts and Superscripts should be set off clearly.

Equation writing software that presents each equation as an object in MS Word will be accepted. Style and convention adopted for the equations should be uniform throughout the paper.

References:

All references to publications cited in the main text should be presented as a list of references in order following the text and all references in the list must be cited in the text. References should be arranged chronologically, in the text. The list of references should be arranged alphabetically at the end of the paper.

References should be given in the following form:

Kaila, K.L., Reddy PR., Mall D.M., Venkateswarlu, N., Krishna V.G. and Prasad, A.S.S.S.R.S., 1992, Crustal structure of the west Bengal el eon deep seismic sounding investigations. Geophys. J. Int., 1,45-66.

REVIEW PROCESS:

All manuscripts submitted to the journal are peer-reviewed. It is advisable to send the contact details of 4 potential reviewers along with the manuscript to expedite the review process. Editor has the option to select reviewers from the list or choose different reviewers. The review process usually takes about 3 months. All enquiries regarding the manuscript may be addressed to the Chief Editor.

GALLEY PROOF:

Technical editing of manuscripts is performed by the editorial board. The author is asked to check the galley proof for typographical errors and to answer queries from the editor. Authors are requested to return the corrected proof within two days of its receipt to ensure uninterrupted proceedings The editor will not accept new material in proof unless permission from the editorial board has been obtained for the addition of a "note added in proof". Authors are liable to be charged for excessive alterations to galley proof.

PUBLICATION CHARGES:

There are no page charges for publication. The corresponding author will receive a soft copy (pdf format) of his/her published article. Should the author desire to purchase reprints of his/her publication, he/she must send the duly signed Reprint Order Form (accompanies the galley proof and contains price details) along with the corrected galley proof to the Editor. The reprint charges must be paid within one month of sending the Reprint Order Form.

Any payment related to printing or purchase of reprints should be made in the form of a Demand Draft in the name of Treasurer, Indian Geophysical Union, payable at Hyderabad.

You may download the pdf file from:
http://iguonline.in/journal/instructions.php